Resolution Improvement in Optical Microscopy by Use of Multi-Beam Interferometric Illumination

by

Jekwan Ryu

Submitted to the Harvard–Massachusetts Institute of Technology
Division of Health Sciences and Technology
in partial fulfillment of the requirements for the degree of

Doctor of Philosophy

at the

MASSACHUSETTS INSTITUTE OF TECHNOLOGY

September 2003

Author .....
Harvard–Massachusetts Institute of Technology Division of Health Sciences and Technology
July 5, 2003

Certified by .....
Dennis M. Freeman
Associate Professor of Electrical Engineering
Thesis Supervisor

Accepted by .....
Martha Gray
Chair, Departmental Committee on Graduate Students

MIT Libraries
Document Services

Room 14-0551
77 Massachusetts Avenue
Cambridge, MA 02139
Ph: 617.253.5668 Fax: 617.253.1690
Email: docs@mit.edu
http://libraries.mit.edu/docs

DISCLAIMER OF QUALITY

Due to the condition of the original material, there are unavoidable flaws in this reproduction. We have made every effort possible to provide you with the best copy available. If you are dissatisfied with this product and find it unusable, please contact Document Services as soon as possible.

Thank you.

pgs. 113 - 114 are missing from the original thesis

Resolution Improvement in Optical Microscopy by Use of Multi-Beam Interferometric Illumination

by

Jekwan Ryu

Submitted to the Harvard–Massachusetts Institute of Technology Division of Health Sciences and Technology
on July 5, 2003, in partial fulfillment of the requirements for the degree of Doctor of Philosophy

Abstract

In conventional optical microscopy, the numerical aperture (NA) of the objective lens intrinsically links the resolution, depth of field (DOF), working distance (WD) and field of view (FOV). In a diffraction-limited system, changing the NA to improve resolution is not possible without degrading the other optical performances. This linkage, which represents an important limitation in conventional microscopy, has now been broken.

In the new method, a target is illuminated by a sequence of finely textured light patterns generated by interference of multiple coherent beams that converge in a cone. The corresponding sequence of brightness values, measured by a single photodetector (e.g., a *single pixel* of a CCD), encodes the target's sub-pixel contrast pattern. Fourier domain components at spatial frequencies contained in the probing illumination patterns can be recovered from the pixel brightness sequence by solving a set of over-determined linear equations. For a given wavelength, the resolution of the reconstructed image is primarily determined by the NA of the cone of beams, rather than the NA of the microscope objective. A low NA objective, with large DOF, long WD, and large FOV, can be used without compromising resolution.

A cone of 31 coherent beams with NA of 0.98 is produced from a single source beam ($\lambda =$ 488 nm) using an acousto-optic deflector (AOD) and an all-reflective beam delivery system. The target is placed where the beams overlap. Fluoresced light from the target is collected with a 0.2 NA objective for 930 different interference patterns. Brightness sequences are decoded to reconstruct an image with resolution comparable to what would be obtained using a conventional system with a 0.98 NA objective. Further, changing the NA of the actual objective from 0.2 to 0.1 causes negligible change in resolution, demonstrating that resolution is primarily determined by the illumination produced by the cone of beams.

Another restriction of conventional systems is removed by the use of reflective elements. The illumination system, which determines resolution, can be constructed using only reflective elements. Ultraviolet or x-ray illumination can be used with fluorescing targets to obtain resolution beyond what is possible using visible light. The well-known problems of refractive optics at short wavelengths can be avoided.

Thesis Supervisor: Dennis M. Freeman
Title: Associate Professor of Electrical Engineering

Acknowledgments

It is my pleasure to acknowledge gratefully some of the people who helped me throughout this thesis work.

I cannot thank Professor Denny Freeman enough, who supervised this thesis. I thank him for his support throughout the project and for providing me such a tremendous learning experience during this period. His passion and integrity really affected me and made me think seriously about what it means to become a scientist, and to become a creative and critical thinker. I was extremely fortunate to meet him at this stage of my life and career.

I also had the good fortune of working closely with my other teachers on this project: Professors Berthold Horn, George Barbastathis, and Jennifer Melcher. Their enthusiastic participation and guidance really contributed to many different aspects of the project. Especially, I thank Professor Horn for his numerous contributions on theoretical and computational aspects of the project.

I am indebted to people from the MIT Micromechanics group for providing a stimulating and fun environment where I was able to learn and grow. I am grateful to A. J. Aranyosi, Janice Balzer, Andy Copeland, Salil Desai, Amy Englehart, Roozbeh Ghaffari, Stanley Hong, Werner Hemmert, Kinuko Masaki, Michael Mermelstein. Michael Mermelstein, who originally invented the concept of Synthetic Aperture Optics that appears in this thesis, guided me through my early involvement in the project. I also would like to thank Stanley Hong for numerous stimulating discussions, some of which made me think about the same problem in an entirely different way, and for being always available for help with optics setup. I also thank A. J. Aranyosi for sharing with me his critical thinking and experiences on various scientific and practical problems encountered.

I am grateful to several people from MIT for their contributions: John Fini from the Optics and Quantum Electronics group for his help in mathematical formulation of the beam calibration problem, Daniel Feldkhun from the Lincoln laboratory for his work on the acousto-optic interference pattern projector, Joe Deck at Lightwave

Instruments for proof-reading this thesis and providing many helpful suggestions on writing. I also thank Professors Gilbert Strang and Peter So for their interest in the project and for generously offering their time to discuss the project with me, including mathematical and theoretical aspects and possible future applications.

I would also like to thank my family, especially my parents, for their support and love during my entire life. In particular, I thank Seungmin, my wife and my best friend, without whose love, encouragement, and support, I could not have finished this thesis.

Contents

Chapter 1

Introduction

Since the invention of the compound microscope at the beginning of the seventeenth century (Hooke, 1961), optical microscopy has been an important tool in many fields of science and engineering, especially in biomedical sciences. It is a powerful tool in biology and medicine since it can be used to investigate the structure and function of a biological system while it is alive. This capability is not available in other microscopic imaging tools such as electron microscopy (EM) or scanning probe microscopy (SPM).

However, the physics of the lens, which is the key element of microscopy imaging, imposes several important limitations. This thesis describes and demonstrates an optical microscopy technique based on principles of image formation that are different from conventional optical microscopy in order to overcome some of these limitations.

1.1 Limitations of conventional optical microscopy

1.1.1 Resolution limited by the wavelength of light

Resolution in optical microscopy is fundamentally limited by the wavelength of light (Abbe, 1873). The size of the smallest feature that can be resolved by optical microscopy (as defined by the Rayleigh criterion (Born and Wolf, 1999)) is $0.61\lambda/\mathrm{NA}$ where λ is the wavelength of light, and NA is the numerical aperture of the objective lens.

The limiting resolution predicted by this formula improves when the wavelength

is reduced. However, scaling an optical microscopy to wavelengths shorter than those of visible light is a challenging problem. Few materials are suitable for refractive elements at very short wavelengths. Commonly used refractive materials become opaque at short wavelengths, while others exhibit birefringence (Wang et al., 2002; Wang, 2003).*

One alternative is to use reflective elements instead of refractive elements for image formation, since some common materials reflect light of even relatively short wavelength satisfactorily. However, few examples of quality imaging systems consisting entirely of reflective elements exist. This may be in part because fewer degrees of freedom are available in designs using reflective elements (one radius of curvature per element) when compared with refractive elements (two radii of curvature plus choice of refractive index per element). For the above reasons, scaling optical microscopy to short wavelengths of light to improve resolution is, while highly desirable, a scientifically challenging problem.

1.1.2 Intrinsic coupling between optical performances

At a fixed wavelength of light, resolution can only be increased by increasing NA. However, increasing NA decreases depth of field (DOF $= 2\lambda/\mathrm{NA}^2$), the axial portion of the specimen which is in focus.

Decreasing DOF is undesirable when the surface of an opaque target, such as transistors on a silicon wafer or DNA molecules on a glass substrate, is visualized. Small DOF means only a small portion of the target near the plane of focus would be imaged. In many applications, it is desirable to obtain a sharply focused image of the target regardless of its distance from the objective.

*The next step in optical projection lithography is to use a 157 nm laser, with the goal of using this wavelength to write structures as small as 60 or even 50 nm. One of the most difficult problems is to manufacture the refractive material for the lenses. Calcium fluoride, the material of choice, must be grown as a single crystal, which takes a very long time. The quality requirements are also very high, resulting in unsatisfactory yields associated with crystal growth. On top of that, calcium fluoride shows intrinsic birefringence, meaning that the index of refraction depends on the plane of the beam's polarization. Consequently, only polarized light will result in sharply focused images in a single plane, making it even more difficult to fashion a lens for this wavelength.

Furthermore, if the physical size of the lens is also fixed, increasing NA also decreases working distance (WD; space between the front element of the objective and the top of the specimen) and field of view (FOV). Decreasing WD eliminates certain possibilities of simultaneously manipulating or probing the sample non-optically, for example, electrophysiological recording or mechanical intervention. Decreasing FOV is undesirable when, for example, interaction between cells or structures that are remote from each other needs to be studied.

Given the wavelength of light and the size of the lens, the resolution, DOF, WD, and FOV are intrinsically linked. One cannot be changed to improve optical performance without changing the others in ways that may degrade performance.

This trade-off between resolution and other optical performances is illustrated in Figure 1-1, where the four optical performances of twenty different microscope objectives from a leading manufacturer are shown (Mermelstein, 2000c). The chart shows that as the NA of the objective increases from 0.075 to 1.4, improving the resolution, the remaining parameters (the DOF, WD, and FOV) decrease by more than two orders of magnitude.

1.2 Previous work

Previously, the resolution limit of a high NA objective was decreased by a factor of two using a structured illumination technique (Bailey et al., 1993; Neil et al., 1997; Heintzmann and Cremer, 1998; Gustafsson et al., 1999; Gustafsson, 2000; Frohn et al., 2000). Such structured, or textured, illumination patterns are generated by the interference of two or four coherent beams with equal wavelengths. By illuminating the target with a high spatial resolution light pattern, high spatial frequency components of the target, which would not normally pass through the objective, can be encoded into low spatial frequencies that *will* pass through the objective. After electronic post-processing of the data, a high resolution image of the target can be obtained. Theoretical aspects of this concept have been extensively studied previously (Krishnamurthi et al., 1996; Cragg and So, 2000; Frohn et al., 2001; So et al., 2001).

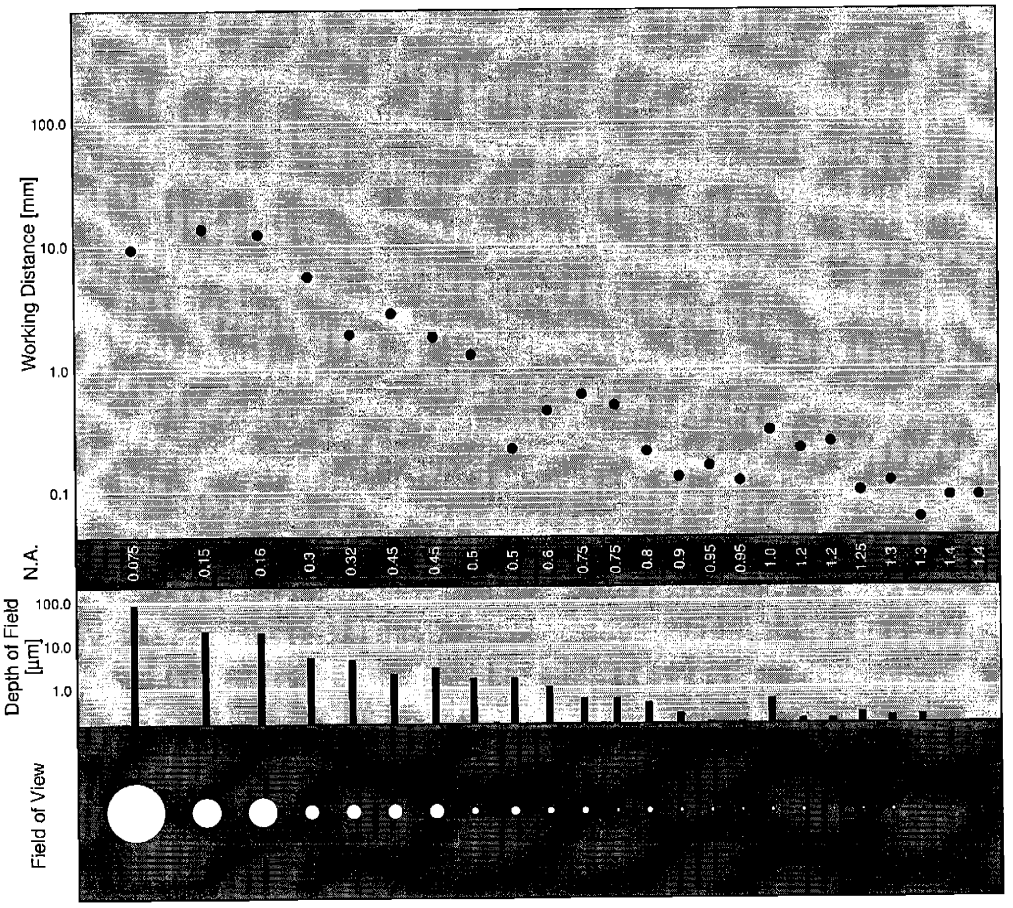

Figure 1-1: Four key performance parameters of optical microscopy imaging: resolution, working distance, depth of field, and field of view, for 20 different microscope objectives from a leading manufacturer, chart courtesy of M. S. Mermelstein. At a given wavelength of light, the resolution improves as the NA increases. The chart shows that as the NA increases by an order of magnitude (from 0.075 to 1.4), there are more than two orders of magnitude reduction in the working distance, depth of field, and field of view.

When the structured illumination is produced by sufficiently many beams, it can not only improve resolution, but can also become a primary mechanism of image formation. In fact, when a sequence of structured illuminations are used, a high resolution image of the target can be reconstructed from a sequence of target brightness measurements only, requiring no resolving power on the detection side. This concept, called synthetic aperture optics, was originally formulated by Mermelstein (Mermelstein, 2000a; Mermelstein, 2000b; Mermelstein, 2000c).

In synthetic aperture optics, resolution is limited by the resolution of the struc-

tured illumination pattern, and therefore is still limited by the wavelength of light. However, it is not limited by the resolution of optical elements on the sensor side (such as the NA of the objective, and the sensor pixel size). Therefore, a low NA objective can be used on the detection side of the system, allowing us to take advantage of its increased working distance, wider field of view, and larger depth of field. When high resolution structured illumination is combined with a low NA objective, the system can achieve high resolution without compromising the WD, DOF, and FOV.

Additionally, the physical apparatus that delivers the structured illumination can be entirely made of reflective optical elements (e.g., mirrors). Reflective elements, unlike the refractive element such as the lens, can handle short wavelengths of light such as ultraviolet (UV) or X-ray. Therefore, synthetic aperture optics is a promising way to improve the resolution of optical imaging beyond what is possible with visible light by scaling to UV or even X-ray.

1.3 The scope of this thesis

This thesis presents the first experimental demonstration of the synthetic aperture optics concept. Specifically, it is shown that a sequence of brightnesses of a target, measured using a single photodetector (e.g., a single pixel of a CCD) when the target is illuminated by a sequence of structured light patterns, can be processed to reconstruct an image of the target that reveals sub-pixel details of target's contrast pattern. Furthermore, experimental evidences are presented that prove the fact that the structured illumination, rather than the microscope objective as in the conventional system, is the primary source of resolution. This fact leads to breaking of the intrinsic link between resolution and other optical performances.

Realization of the synthetic aperture optics concept is based on solution to several previously unresolved problems. First, it is necessary to illuminate the target with a *known* sequence of interference patterns formed by sufficiently many laser beams. Previously, an interference pattern projector with 15 beams, generated and controlled using the acousto-optic effect, was described (Mermelstein, 2000c). Utilizing the

same principle of acousto-optics, this thesis describes the physical apparatus of a 31 beam interference pattern projector. A major contribution of this thesis is a newly developed dynamic beam calibration method, which is required to make use of the interference pattern projector. The developed beam calibration technique removes the requirement for building a physically perfect system and enables dynamic assessment of imperfections in the physical system.

Another problem is encountered when post-processing the data to reconstruct an image of the target. In synthetic aperture optics, target information is sampled in the Fourier domain at spatial frequencies contained in the probing illumination patterns and the image of the target is reconstructed using a procedure similar to an inverse Fourier transform. However, the distribution of the sampled spatial frequencies in the Fourier domain is highly non-uniform. This is because of the constraints imposed by the geometric arrangement of the beams. Similar problems have been encountered in the fields of radio-astronomy (Keto, 1997; Brow, 1975) and magnetic resonance medical imaging (Herman, 1979; Mueller et al., 1979; King and Moran, 1984). This thesis describes an image reconstruction algorithm that applies when the transform domain is not sampled uniformly. Furthermore, it is shown that uniform angular spacing of the beams generating the illumination patterns leads to less than ideal sampling of the transform space, and alternative geometric arrangements are proposed.

In the following chapters, the term *structured illumination* is used to refer to an optical microscopy method based on the concept of synthetic aperture optics, while *uniform illumination* refers to the conventional optical microscopy.

Chapter 2

Theoretical Overview

This chapter describes how structured illumination patterns can be used to increase the resolution of an imaging system for optical microscopy. A target is illuminated by a sequence of finely textured light patterns formed by the interference of multiple coherent beams. The sequence of brightness values reported from a *single* pixel of a charge coupled device (CCD) imager encodes the target contrast pattern with sub-pixel resolution. Previously, it was shown that Fourier domain components at spatial frequencies contained in the probing illumination patterns can be recovered from the pixel brightness sequence by solving a set of over-determined linear equations (Mermelstein, 2000c).

In this chapter, several newly developed theories and post-processing algorithms are described together with previously developed theories. It is shown that uniform angular spacing of the beams generating the illumination patterns leads to less than ideal sampling of the transform space, and alternative geometric arrangements are proposed. An image reconstruction algorithm based on the Voronoi diagram, that applies when the transform domain is not sampled uniformly, is described. Finally, it is shown that the contrast patterns within individual pixels can be spliced together to form an image encompassing multiple pixels.

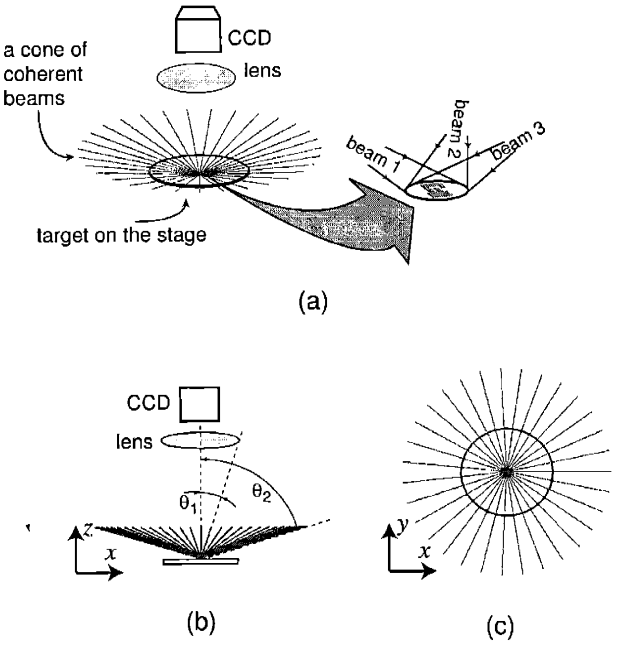

Figure 2-1: Generation of structured illumination using the interference of multiple coherent beams. (a) Schematic of the imaging setup showing a lens, a CCD, and a cone of 31 coherent beams illuminating the target. The target is placed where the beams overlap, as illustrated in the right side. For clarity, only three beams are shown. (b) Side view of the setup. The cone half angle of the beams (θ_2) and the cone half angle of the lens (θ_1) are indicated. (c) A view of the cone of beams looking from the top.

2.1 Physical elements

2.1.1 High resolution structured illumination

High spatial resolution structured illumination patterns are formed by the interference of multiple coherent beams. Figure 2-1 (a) illustrates an optical imaging setup using a lens and a CCD in which illumination is provided by a number of coherent beams that overlap in an area where a target is placed. In the region of overlap, a light pattern is formed as the result of interference between the beams. It is this pattern that illuminates the target. The right side of Figure 2-1 (a) shows a magnified view of the target region where beams overlap. Only three beams are shown for clarity. The overlapping beams form a cone in three-dimensional space. Figure 2-1 (b) is a side view of the cone of beams, while Figure 2-1 (c) shows a view from the top, i.e. from the direction of the lens and the CCD imager.

Suppose there are N coherent beams overlapping in the target region. The electric field, $\mathbf{E}$, of the n-th beam, as a function of position $\mathbf{r}$ and time t, can be written as

$$\mathbf{E}_n(\mathbf{r},t) = a_n \cos(\mathbf{k}_n \cdot \mathbf{r} - \omega_n t + \phi_n)\hat{\mathbf{p}}_n \tag{2.1}$$

where a_n is the amplitude, $\mathbf{k}_n$ the wavenumber*, ω_n the optical frequency, ϕ_n the optical phase, and $\hat{\mathbf{p}}_n$ the polarization vector. The intensity pattern formed by the interference of N beams then is

$$I(\mathbf{r},t) = \left|\sum_{n=1}^{N} \mathbf{E}_n(\mathbf{r},t)\right|^2 . \tag{2.2}$$

In the method presented here, the beams all originate from the same source and so λ_n and ω_n are the same for all beams. In addition, the polarization vectors $\hat{\mathbf{p}}_n$ of the beams are assumed to be equal†. Then the average of $I(\mathbf{r},t)$ over one cycle can be written as

$$I(\mathbf{r}) = \frac{1}{2}\sum_{l=1}^{N}\sum_{m=1}^{N} a_l a_m \cos(\mathbf{k}_{lm} \cdot \mathbf{r} + \phi_{lm}) \tag{2.3}$$

where $\mathbf{k}_{lm} = \mathbf{k}_l - \mathbf{k}_m$ and $\phi_{lm} = \phi_l - \phi_m$. Eq. (2.3) shows that the intensity pattern is a function of position $\mathbf{r}$ and is completely characterized by the amplitudes (a_n), the optical phases (ϕ_n), and the wavenumbers $(\mathbf{k}_n)$ of the beams. When the directions of propagation of the beams are fixed in space by the physical arrangement of the apparatus, then the intensity pattern $I(\mathbf{r})$ becomes a function of just the amplitudes and optical phases of the beams. Consequently, the intensity pattern can be changed by modulating these beam parameters. Figure 2-2 (a) shows a computer simulated intensity pattern in the target plane formed by the interference of 31 beams as illustrated in Figure 2-1. The cone half angle of the beams (θ_2) was chosen to be 78° in this illustration. In this particular example, the amplitudes of all beams were

*The wavenumber $\mathbf{k}_n$ is $(2\pi/\lambda_n)\hat{\mathbf{l}}_n$, where λ_n is the wavelength and $\hat{\mathbf{l}}_n$ is a unit vector defining the direction of propagation of the n-th beam. The vectors $\mathbf{k}_n$ and $\hat{\mathbf{p}}_n$ are perpendicular to one another.

†In fact, the polarization vectors of the beams cannot be made exactly equal, but this is a good approximation if the beams are TM (Transverse Magnetic) polarized and the cone half angle of the beams (θ_2) is close to 90°.

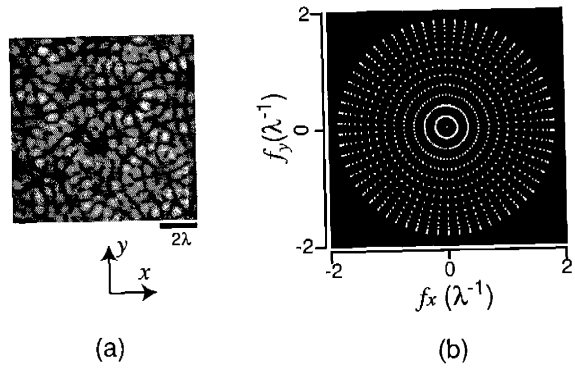

Figure 2-2: (a) Computed structured illumination pattern in the target plane formed by the cone of 31 beams shown in Figure 2-1 ($\theta_2 = 78^\circ$). (b) Fourier transform magnitude of the pattern in (a) showing a total of 931 bright spots corresponding to a set of spatial frequency components contained in the intensity pattern in (a).

set equal and the optical phases of the beams were chosen randomly with uniform distribution between 0 and 2π.

Eq. (2.3) shows that in the Fourier domain, the intensity pattern $I(\mathbf{r})$ is composed of a set of distinct spatial frequency components $\mathbf{k}_{lm}$, for $l = 1, 2, \cdots, N$ and $m = 1, 2, \cdots, N$. The total number of distinct frequency components (p) is determined by the number of beams (N), and is $p = N^2 - N + 1$.[‡] The values of the spatial frequencies themselves are determined by the differences between the wavenumbers of all possible pairs of beams. The highest spatial frequency is $2\sin(\theta_2)/\lambda$. Figure 2-2 (b) shows the Fourier transform magnitude of the intensity pattern in Figure 2-2 (a). It shows a total of 931 (i.e. $31^2 - 31 + 1$) bright spots corresponding to the spatial frequency components of the pattern in Figure 2-2 (a).

As will be shown in the following section, the resolution of the proposed system is determined by the spatial frequency components contained in the structured illumination. Since the highest spatial frequency component (and hence the smallest feature size) of the illumination pattern is controlled by the cone half angle of the beams (θ_2) at a given wavelength of light, the angle θ_2 controls the resolution of the system. For a traditional imaging system in Figure 2-1 with uniform illumination, the

[‡]When $l = m$ in Eq. (2.3), the corresponding spatial frequency $\mathbf{k}_{lm}$ becomes zero (DC), so N of the N^2 combinations contribute to a single frequency component.

resolution is instead controlled by the cone half angle of the objective lens (the angle θ_1 in Figure 2-2, NA $= \sin(\theta_1)$). The ratio $\eta = \sin(\theta_2)/\sin(\theta_1)$ represents the increase in maximum spatial frequency content present as the result of the use of structured illumination.

In the computer simulations that follow, the NA of the lens in Figure 2-1 was chosen to be 0.13 (therefore, $\theta_1 = 7.5°$), representing the lowest NA from a leading manufacturer of microscope objectives. This lens selection aims at the advantages in field of view, working distance, and depth of field that a low NA lens offers. The cone half angle of the beams (θ_2) was selected to be 78°, its value in the multiple beam interference pattern projector that will be described in the following chapter. Notice that the value η — representing the increase in maximum spatial frequency content present due to structured illumination — corresponds here to $\sin(78°)/\sin(7.5°) = 7.5$.

Note that the three-dimensional brightness pattern $I(\mathbf{r})$ is constant in the z-direction if all the wavenumbers $\mathbf{k}_n$ have the same z-component. This happens when the beams all come in at the same angle ($\pi/2 - \theta_2$ in Figure 2-1) with respect to the target plane $z = 0$. The result is very large depth of field, limited only by the low NA of the objective lens. As a result we treat the target contrast as an essentially two-dimensional pattern in the following, i.e., a function of $\mathbf{r}$ in the target plane $z = 0$.

2.1.2 Low resolution imager

Suppose that there are N beams, and M distinct structured illumination patterns are projected in sequence by controlling the amplitudes (a_n) and the optical phases (ϕ_n) of the beams. Let $I_j(\mathbf{r})$ represent the intensity of the j-th illumination pattern as a function of position $\mathbf{r}$. The planar target is represented by a contrast value as a function of position, $C(\mathbf{r})$.[§] In a simulation we use the image shown in Figure 2-3 (a) as the target contrast pattern. The light pattern that falls on the CCD imager,

[§]Here, the position vector $\mathbf{r}$ is in target coordinates. For convenience, the magnification of the imager can be treated as if it were unity, in which case the position vector in the target coordinates also designates the position in the image coordinates.

$g_j(\mathbf{r})$, is given by

$$g_j(\mathbf{r}) = [C(\mathbf{r})I_j(\mathbf{r})] * h(\mathbf{r}) \quad j = 1, 2, \cdots, M \tag{2.4}$$

where $h(\mathbf{r})$ represents the point spread function (PSF) of the lens (Born and Wolf, 1999) and $*$ designates the convolution operation.

The array of the pixels of the CCD can be viewed as an array of light sensors where each pixel corresponds to a single light sensor. The brightness b_j reported from a single pixel of the CCD imager positioned at the origin ($\mathbf{r} = 0$) of the coordinate system becomes

$$b_j = \int g_j(\mathbf{r})p(\mathbf{r})\, d\mathbf{r} \quad j = 1, 2, \cdots, M \tag{2.5}$$

where $p(\mathbf{r})$ represents the response of the pixel, modelled as a two dimensional boxcar function, which is one inside the boundary of the pixel, and zero elsewhere. Substituting Eq. (2.4) into Eq. (2.5) and performing some algebraic manipulations leads to

$$b_j = \int [w(\mathbf{r})C(\mathbf{r})]I_j(\mathbf{r})\, d\mathbf{r} \tag{2.6}$$

$$= \int C^w(\mathbf{r})I_j(\mathbf{r})\, d\mathbf{r} \quad j = 1, 2, \cdots, M \tag{2.7}$$

where $w(\mathbf{r}) = h(\mathbf{r}) * p(\mathbf{r})$ is the two-dimensional convolution of $h(\mathbf{r})$ and $p(\mathbf{r})$, i.e., the combined PSF of the lens and the CCD sensor element. In the following, $w(\mathbf{r})$ will be called the "window" function — it gives the response of a picture cell to incident light as a function of position relative to the center of that picture cell. A simulated windowing function $w(\mathbf{r})$ is shown in Figure 2-3 (b). In Eq. 2.7, $C^w(\mathbf{r}) = w(\mathbf{r})C(\mathbf{r})$ is the "windowed" target contrast function. A sample $C^w(\mathbf{r})$ shown in Figure 2-3 (c) corresponds to $C(\mathbf{r})$ and $w(\mathbf{r})$ shown in parts (a) and (b).

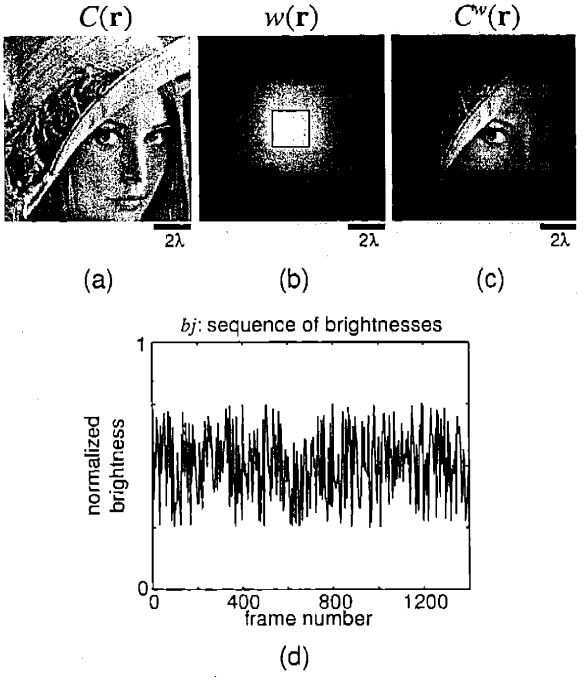

Figure 2-3: Encoding sub-pixel target contrast information in a sequence of brightness values from a single pixel. (a) $C(\mathbf{r})$; a target contrast function. (b) $w(\mathbf{r})$; a window function for a pixel positioned at the origin (the center of the image). NA = 0.13, pixel size = 2λ. The rectangle at the center shows the actual size of the pixel relative to the window function. (c) $C^w(\mathbf{r}) = C(\mathbf{r})w(\mathbf{r})$; a windowed target, (d) Simulated sequence of brightness values reported from a single pixel while the target was illuminated by a sequence of $M = 1400$ different structured illumination patterns.

2.2 Computational elements

2.2.1 Decoding target information

Eq. (2.7) shows that, for a given sequence of textured illumination patterns, the recorded sequence of brightness values is a function of $C^w(\mathbf{r})$. For a computer-simulated sequence of 1400 illumination patterns[¶], and the target shown in Figure 2-3 (a), the resulting brightness sequence is shown in Figure 2-3 (d). The sequence of illumination patterns was generated by changing the optical phases of the beams.[‖]

The sequence of brightness values b_j, $j = 1, 2, \cdots, M$, in Eq. (2.7) encodes infor-

[¶]We picked $M = 1400$ patterns so as to yield an overdetermined system of linear equations in the unknown components at 931 frequencies.

[‖]For each illumination pattern, 31 optical phases were chosen randomly between 0 and 2π with uniform distribution. In this simulation the amplitudes of the 31 beams were kept equal.

mation on the windowed target contrast $C^w(\mathbf{r})$ at spatial frequencies present in the sequence of illumination patterns $I_j(\mathbf{r})$, $j = 1, 2, \cdots, M$. This can be more clearly seen after replacing $I_j(\mathbf{r})$ in Eq. (2.7) by the expression in Eq. (2.3) and performing several steps of algebraic manipulations to rewrite Eq. (2.7) as the following matrix equation (Mermelstein, 2000c):

$$\mathbf{b} = A\mathbf{x} \tag{2.8}$$

where the $M \times 1$ column vector $\mathbf{b} = [b_1, b_2, \cdots, b_M]^T$ is the measured brightness sequence, while the $p \times 1$ column vector $\mathbf{x}$ equals

$$[x_{DC}, x^c_{12}, x^s_{12}, x^c_{13}, x^s_{13}, \cdots, x^c_{(N-1)N}, x^s_{(N-1)N}]^T$$

and represents a total of $p = (N^2 - N + 1)$ Fourier transform coefficients of the windowed target contrast $C^w(\mathbf{r})$ at spatial frequencies present in the illumination pattern. Specifically,

$$x_{DC} = (N/2) \int C^w(\mathbf{r})\, d\mathbf{r} \tag{2.9}$$

$$x^c_{lm} = \int C^w(\mathbf{r}) \cos(\mathbf{k}_{lm} \cdot \mathbf{r})\, d\mathbf{r} \tag{2.10}$$

$$x^s_{lm} = \int C^w(\mathbf{r}) \sin(\mathbf{k}_{lm} \cdot \mathbf{r})\, d\mathbf{r} \tag{2.11}$$

The j-th row, A_j, of the $M \times p$ matrix A, is determined by the amplitudes (a_n) and the optical phases (ϕ_n) of the beams for the j-th illumination. Specifically, A_j equals

$$[1, \alpha_{12}, -\beta_{12}, \alpha_{13}, -\beta_{13}, \cdots, \alpha_{(N-1)N}, -\beta_{(N-1)N}]$$

with $\alpha_{lm} = a_l a_m \cos(\phi_{lm})$ and $\beta_{lm} = a_l a_m \sin(\phi_{lm})$.

For $M > p$, Eq. (2.8) is an overdetermined linear system. Using knowledge of the illumination, i.e., the matrix A and the measured brightness sequence, the vector $\mathbf{b}$, we can find $\bar{\mathbf{x}}$, the best approximation to the solution $\mathbf{x}$ of Eq. (2.8) in the least squares sense, using

$$\bar{\mathbf{x}} = (A^T A)^{-1} A^T \mathbf{b} \tag{2.12}$$

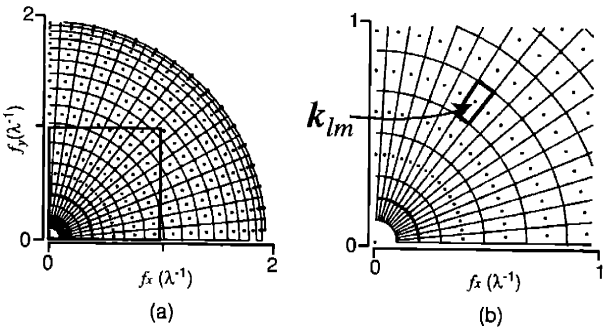

Figure 2-4: Calculating the weights to be given to samples in Fourier space using the areas of the Voronoi polygons. (a) The Voronoi diagram for the distribution of the Fourier sample points in Figure 2-2 (b). Only the first quadrant of the Fourier space is shown for clarity (The point at the lower left corner corresponds to DC). (b) Magnified view of a rectangular sub-region in (a) indicating an example Fourier sample point ($\mathbf{k}_{lm}$) and its corresponding Voronoi polygon.

where $(A^TA)^{-1}A^T$ is the pseudoinverse of A.

Notice that the number of estimated Fourier transform coefficients (p) increases quadratically with the number of beams (N). This means that with a relatively modest number of beams (e.g., 31), a large enough number of Fourier transform coefficients (e.g., 931) of the target's contrast pattern can be estimated to reconstruct an image of the target from the data**.

Notice also that the resolution (or equivalently the spatial frequency content) of the reconstructed image is determined by the illumination and is not directly limited by the factors limiting resolution in a traditional imaging system, such as the NA of the lens, and the CCD's pixel size. Instead of determining the resolution, the NA of the lens controls the size of the window function $w(\mathbf{r})$ and therefore defines the area of the target that is represented by the vector $\mathbf{x}$ in Eq. (2.8).

2.2.2 Image reconstruction

If sufficiently many Fourier transform coefficients are obtained using the method described in the previous section, then an image of the windowed target can be reconstructed. As is well known, an arbitrary function can be reconstructed exactly from

**As a rough rule of thumb, N beams provide about enough information to reconstruct the N^2 brightness values in an $N \times N$ array of sub-pixel cells.

its Fourier transform. The Fourier transform is a continuous function of frequency. In contrast, here only a finite number of samples of the Fourier transform of $C^w(\mathbf{r})$ are obtained by solving Eq. (2.8). Furthermore, as is illustrated in Figure 2-2 (b), the distribution of these Fourier sample points is highly non-uniform. First of all, the sampling density varies with frequency, being low at mid-frequencies and high at both low and high frequencies. Secondly, in the low spatial frequency region, while the sample points are densely populated along the angular direction, they are sparsely populated along the radial direction. The reverse is true at high frequencies.

To compensate for sampling density non-uniformity in Fourier space, the coefficient of each sample point in Fourier space is weighted according to the inverse of the density of sample points in the vicinity. This notion was implemented by allocating non-overlapping space-filling elemental areas to the sample-points. The density at a sample point is inversely proportional to the corresponding elemental area. These areas are defined by calculating the Voronoi polygon for each sample point. The Voronoi polygon is defined by drawing a boundary enclosing all points lying closer to the sample point in question than to any other sample point (Aurenhammer, 1991). Figure 2-4 (a) shows the Voronoi diagram, which is the set of all Voronoi polygons, for the sample points in Figure 2-2 (b). For clarity, only the first quadrant of Fourier space is shown. Figure 2-4 (b) is an enlarged view of the sub-region of (a) indicated by a rectangle. Sample points are shown as dots, and borderlines between adjacent Voronoi polygons are marked as lines. Notice that the polygons are more elongated in the regions of low and at high frequencies.

The area of each Voronoi polygon was calculated and used as a weighting factor for the corresponding sample point. An image of the estimated windowed target $\widehat{C}^w(\mathbf{r})$ was then reconstructed by summing all weighted frequency components as in Eq. (2.13):

$$\widehat{C}^w(\mathbf{r}) = s_{DC}x_0 + 2\sum_{l=1}^{N-1}\sum_{m=l+1}^{N} s(\mathbf{k}_{lm})\chi_{lm} \tag{2.13}$$

where s_{DC} and $s(\mathbf{k}_{lm})$ are the areas of the Voronoi polygon corresponding to DC and

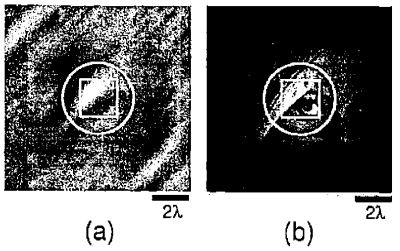

Figure 2-5: (a) An image of the windowed target $C^w(\mathbf{r})$ reconstructed by processing the brightness sequence in Figure 2-3 (d) by the method described in this paper. (b) The original windowed target shown as a reference.

the spatial frequency $\mathbf{k}_{lm}$, respectively and

$$\chi_{lm} = x^c_{lm} \cos(\mathbf{k}_{lm} \cdot \mathbf{r}) + x^s_{lm} \sin(\mathbf{k}_{lm} \cdot \mathbf{r}). \tag{2.14}$$

The above reconstruction formula treats the measured energy contributions as being localized at a single frequency but considers them as representative of the energy over the corresponding Voronoi polygon.††

Figure 2-5 (a) shows an image reconstructed by processing the pixel brightness sequence in Figure 2-3 (d) as described above. The circled area in the image itself defines a region where the window function in Figure 2-3 (b) is more than 50% of its maximum value. The rectangular region inside the circle is the area occupied by the pixel whose brightness measurements were used in reconstructing this image. Part (b) is the original windowed target shown as a reference. Notice that the reconstructed image within the circle in part (a) is similar to the corresponding region in part (b), with some loss of sharpness. Figure 2-5 clearly demonstrates that, using a sequence of brightness measurements from a single pixel, an image can be reconstructed with sub-pixel detail within that pixel. In fact, as shown, an area somewhat larger than the pixel can be reconstructed.

Two factors control the quality of the reconstructed image. First, the wavelength of light, λ, and the half angle of the cone of beams, θ_2, determines the maximum

††We have measurements only at discrete unequally spaced frequencies in the transform domain. We could assume as an approximation that the transform was constant in each Voronoi polygon. Instead we consider all the energy for that polygon to be concentrated at a point.

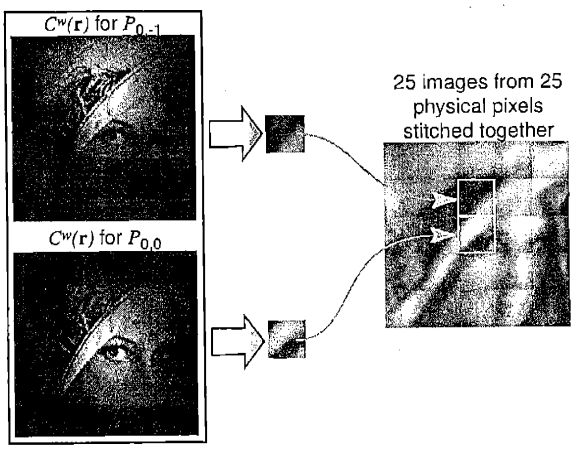

Figure 2-6: Combining images from multiple pixels (The drop-off in brightness at the edges of the tiles is due to drop-off in the windowing function — which has not been compensated for).

spatial frequency $2\pi \sin(\theta_2)/\lambda$ present in the illumination and therefore control the sharpness of the reconstructed image. Second, the total number of beams (N) determines the number of Fourier sample points and therefore controls the density of sampling in the Fourier domain. This in turn determines how many independent sub-pixel samples can be expected to be recovered.

2.2.3 Combining multiple pixels

In the previous section, it was shown that a (small) image can be generated using data from a *single* pixel of a CCD. The array of pixels of a CCD amounts to multiple imagers working in parallel, each looking at a slightly different area. Images generated from multiple pixels can be combined to form a larger image.

Eq. (2.7) describes the brightness of a pixel positioned at the origin of the coordinate system in terms of the window function, $w(\mathbf{r})$, the target contrast, $C(\mathbf{r})$, and the illumination, $I_j(\mathbf{r})$. For a pixel whose center is positioned at $\mathbf{r} = \mathbf{r}_c$, the brightness of the pixel is described by

$$b_j = \int [w(\mathbf{r} - \mathbf{r}_c)C(\mathbf{r})]I_j(\mathbf{r})\, d\mathbf{r} \tag{2.15}$$

where $w(\mathbf{r} - \mathbf{r}_c)$ is $w(\mathbf{r})$ shifted in space by $\mathbf{r}_c$. The windowing function shifted

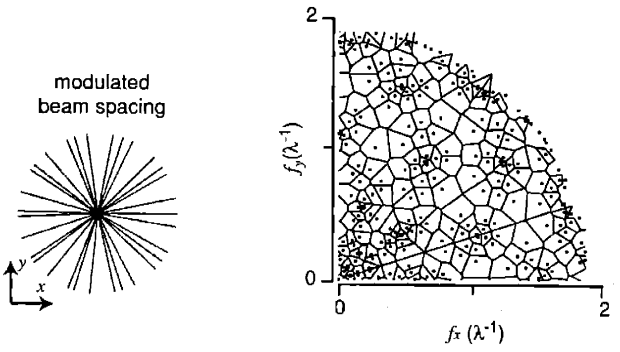

Figure 2-7: Left: beam placement with sinusoidally modulated spacings between adjacent beams. Right: the resulting distribution of sample points in Fourier space, and the corresponding Voronoi diagram.

by the vector $\mathbf{r}_c$ defines a sub-region in the target space to which the output of a particular pixel is responsive, and therefore a region in which a contrast function can be reconstructed from the coded information obtained from the pixel.

In this paper, a simple method for combining images from multiple pixels is presented. Figure 2-6 illustrates this procedure using two adjacent pixels, $P_{0,-1}$ and $P_{0,0}$. The two images inside the left box of Figure 2-6 represent the target contrast pattern multiplied by two different window functions corresponding to the two chosen pixels.The figure illustrates how the position of each window corresponds to the positions of the corresponding pixel.

Processing the data from each pixel is equivalent to performing Fourier analysis of the corresponding windowed target. When processed, the data from each pixel generates an image of a windowed portion of the target contrast. From each such "sub- image," a region corresponding to the area of the pixel is cropped, for example, the rectangular area defined in Figure 2-5 (a). The two small images in the center of Figure 2-6 are sample cropped images. The result of stitching together all the small images for a 5×5 array of pixels is shown on the right.

2.2.4 Optimizing beam placement

The distribution of Fourier sample points is determined by the angular arrangement of the beams. The distribution in Figure 2-2 (b) results from the beam placement shown

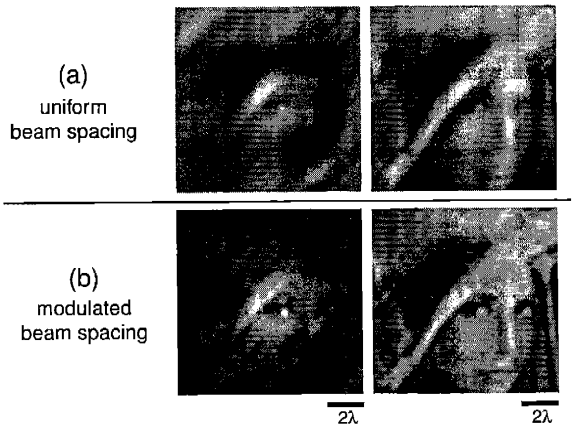

Figure 2-8: Images of the target reconstructed from data obtained (a) using uniform beam spacing, and (b) using modulated beam spacing.

in Figure 2-1 (c), where the beams have uniform angular spacing. In this case, the sample points in Fourier space lie on the intersections of a group of concentric circles and a group of radial lines. The corresponding Voronoi diagram (Figure 2-4) shows that the Voronoi polygons in the low and high frequency regions have high aspect ratio, which is an indication of non-uniform sampling in those regions. The reason this is undesirable is that for fixed cell area, an elongated cell combines frequency components that are further apart than does a cell of a more compact shape.

One could try to find a set of beam angles that provides a more uniform distribution of sample points in Fourier space. One could, for example, minimize some measure of the elongation of the Voronoi polygons using numerical optimization. Figure 2-7 illustrates a particular example of non-uniform beam spacing. The left part of Figure 2-7 shows beam placement, still using 31 beams, in which the angles between adjacent beams vary sinusoidally from beam to beam, rather than all being the same. The right part shows the resulting distribution of sample points in Fourier space and the corresponding Voronoi diagram in the first quadrant. Compared to the uniform beam spacing case illustrated in Figure 2-4 (a), the resulting Voronoi polygons, although still showing considerable variation in area, exhibit significantly reduced aspect ratios, especially in the low and high spatial frequency regions, indicating better sampling.

Figure 2-8 compares images reconstructed using the two different beam placements considered here. Part (a) repeats images shown previously for uniform beam spacing. The left side is reconstructed using a single pixel located at the center, while the right side is tiled from 25 pixels. Part (b) shows corresponding images for the modulated beam spacing case. The effect of improving the distribution of sample points in Fourier space is clear from the reconstructed images. Modulated beam spacing produces images with lower energy background artifacts.

Finally, images of the same target acquired with different conditions are compared in Figure 2-9. The image in part (a) simulates an image acquired with a 0.13 NA lens, using uniform illumination. Here, the pixel size of the CCD imager was assumed to be infinitesimally small. Therefore, part (a) simulates the theoretical resolution limit of a 0.13 NA lens. The image in part (b) simulates the same condition as in part (a), but with finite pixel size of 2λ. The two images in part (c) and part (d) are the same as part (a) and part (b), but with a 0.98 NA lens that has the same cone half angle as the cone half angle of the beams. The image in part (e) was generated with a 0.13 NA lens and a 2λ pixel size, but using a structured illumination sequence.

Several observations can be made here. First, the results in Figure 2-9 clearly illustrate that the structured illumination technique overcomes the practical resolution limit set by the finite pixel size of a CCD imager, generating an image of the target with sub-pixel details. Second, the resolution of the technique is comparable to the theoretical resolution limit of a 0.98 NA lens — i.e. a lens with the same cone half angle as the cone half angle of the coherent beams — and it is still limited by the wavelength of the illuminating light. An important factor, however, is that, unlike a 0.98 NA objective lens, the illumination part of the new system can be made entirely of reflective optical elements, which makes scaling to short wavelengths of light more practical. Finally, the method has advantages in terms of the field of view, working distance, and depth of field compared with a 0.98 NA lens, since these parameters are instead determined by the 0.13 NA lens on the sensor side.

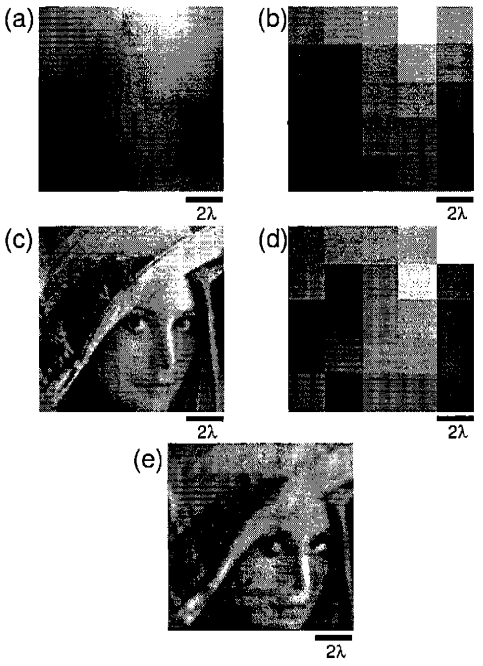

Figure 2-9: Images of the same target acquired with different conditions.

2.3 Summary and conclusion

An optical microscopy method combining high resolution illumination, in the form of a sequence of finely textured light patterns, with low resolution sensing, was described in this chapter. It was shown that the sequence of brightness values reported from a single pixel encodes the target contrast pattern within and near that pixel. A computational scheme to process non-uniformly spaced samples in Fourier space to produce a reconstructed image of the target contrast within and near the pixel was presented. The resolution of such a system is primarily limited by the illumination system, not by the NA of the objective or the size of the pixels, as in traditional microscopic imaging methods. Since the physical apparatus to generate the illumination can be made entirely of reflective optical elements, the method holds potential for scaling optical microscopy to very short wavelengths of light.

In future work, it is desirable to find "optimal" arrangements of beam angles using numerical optimization technique. To do this, it will be necessary to develop suitable optimization criteria. Work on antenna placement in radio astronomy may be

relevant in this connection (Keto, 1997). Another future direction is to investigate improved methods for combining images from multiple pixels, especially noting that the windows for adjacent pixels overlap one another significantly. The method described here is similar in concept to the short-time Fourier transform (STFT) analysis and synthesis technique, which uses overlapping windows that are shifted versions of one another. Formulating the method as a variation of STFT may provide new insights.

Chapter 3

Multiple-Beam Interference Pattern Projector: Hardware

In this chapter, a physical apparatus that produces a cone of multiple intersecting coherent beams is described. The resulting interference pattern projector will serve as an illuminator for the structured illumination microscopy setup described in this thesis.

3.1 Generation and control of multiple beams using acousto-optics

The multiple-beam interference pattern projector described in this chapter relies on the phenomenon of acousto-optic diffraction in generating and controlling many laser beams from a single source beam. An acousto-optic effect is produced by generating an ultrasonic wave in an optically transparent crystalline solid. As the acoustic wave travels through the medium, it causes periodic variations in the index of refraction, causing the material to behave like a diffraction grating (Adler, 1967; Korpel, 1981; Korpel, 1997). That is, a diffracted beam is produced at an angle determined by the frequency of the ultrasonic wave. When the ultrasonic wave has multiple frequency components, multiple diffracted beams are produced, each at an angle determined by

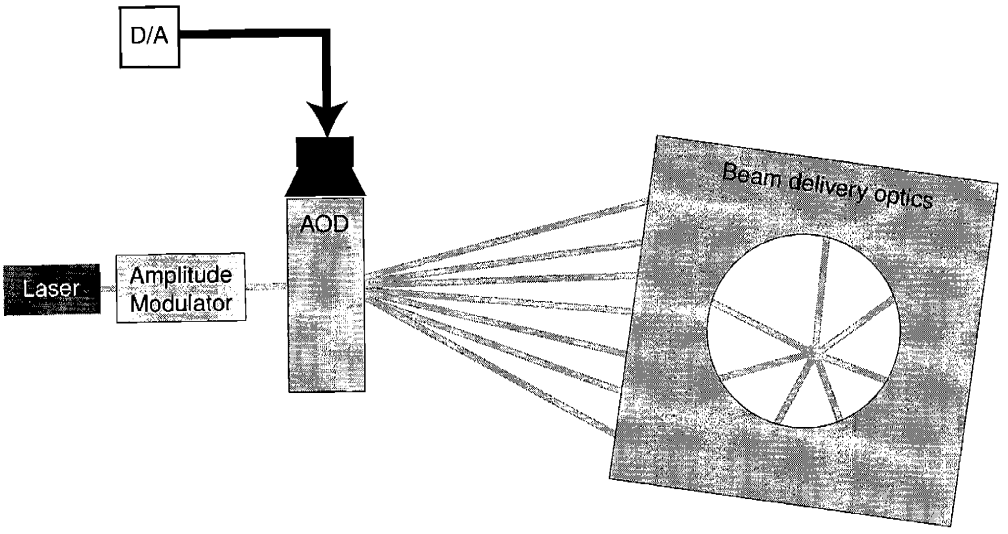

Figure 3-1: Optical layout of the multiple beam interference pattern projector. The figure illustrates generation of multiple laser beams from a single source beam using the AOD. AOD is driven by a radio frequency electrical signal which is the output from a digital to analog converter (D/A). Only seven diffracted beams are shown for clarity and the undiffracted main beam is not shown. Beam delivery optics convert the array of diffracted beams into a converging cone of beams.

each frequency component (Hecht, 1977).

A commercially available acousto-optic device, the acousto-optic deflector (AOD, model LS55-V, Isomet Corporation, Springfield, Virginia) was used in the interference pattern projector described here. The AOD consists of a piece of crystalline material with a piezo-electric transducer on one end and a soft absorber on the other end to prevent reflections. The transducer is driven by a radio frequency (RF) voltage signal.

An optical layout of the projector that used the AOD is illustrated in Figure 3-1. A single line (λ = 488 nm) argon ion laser (model I304C, Coherent, Inc., Santa Clara, California) is used as the source beam and is gated by an amplitude modulator (whose function will be explained in a later section). The figure illustrates generation of multiple diffracted beams using the AOD driven by a RF signal. The beam delivery system comprises mirrors that convert the array of diffracted beams from the AOD into a converging cone of beams, which overlap and form interference patterns in the target region.

The electrical drive signal for the AOD is synthesized digitally. Figure 3-2 shows

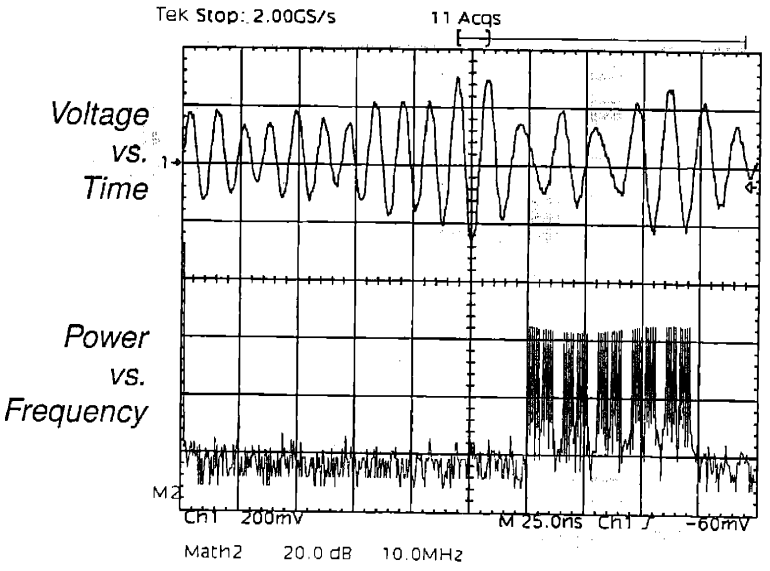

Figure 3-2: Oscilloscope trace of the output voltage signal from the D/A, courtesy of M. S. Mermelstein. The top trace is a portion of the waveform in the time domain and the bottom trace is the power spectrum of the waveform. The power spectrum shows fifty frequency components of the waveform ranging from 60 to 88 MHz.

an example waveform from a digital to analog converter (D/A, model AWG 1200, Chase Scientific Company, Aptos, California). The system was programmed with a waveform composed of fifty discrete sines, each at a distinct frequency. The figure shows a portion of the waveform in the top trace and its power spectrum in the bottom trace. The voltage range from the D/A output is 200 mV per vertical division, shown on a time base of 25 ns per horizontal division. The spectrum is plotted with DC on the far left, 10 MHz per horizontal division, and 20 dB per vertical division.

The spectrum shows the signal's fifty frequency components from 60 to 88 MHz in five pairs of groups of five. A high-bandwidth radio-frequency amplifier (model ZHL-5W, Mini-Circuits, Brooklyn, New York) boosts the signal by 40 dB before delivering it to the AOD. A laser entering the AOD is diffracted as a result. There is a one-to-one correspondence between the frequency components of the AOD drive and the resulting diffracted output beams, shown in the photograph in Figure 3-3.

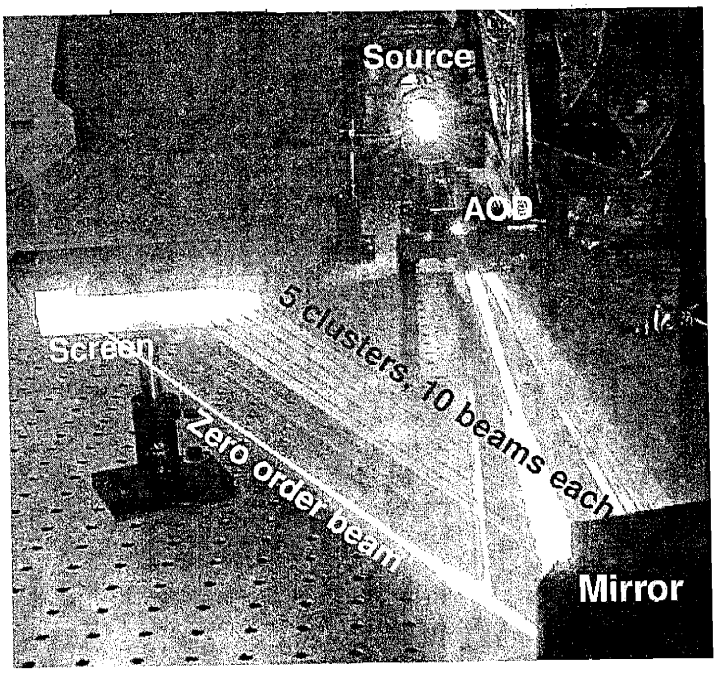

Figure 3-3: Generation of multiple diffracted beams using the AOD. The photograph shows generation of an array of fifty diffracted beams from a single source beam using the AOD, when it is driven by the RF signal shown in Figure 3-2. The mirror on the bottom right corner reflects the diffracted beams onto the screen. The undiffracted, zero order beam is shown also. Notice the correspondence between the structure in the array of diffracted beams and the structure of the power spectrum in Figure 3-2. Photo courtesy of M. S. Mermelstein.

3.1.1 Amplitude control

The structured illumination approach described in this thesis is based on controlling the amplitudes and phases of a set of laser beams to form a controlled interference pattern illuminating the target. The amplitudes of the diffracted beams from the AOD can be independently controlled by controlling the amplitudes of the frequency components of the drive signal. This is demonstrated in Figure 3-4. The top panel shows the power spectrum of a drive signal with 15 distinct frequency components. The resulting 15 output diffracted beams from the AOD are then projected onto a CCD, and the middle panel shows the image of the array of diffracted beams. The bottom panel shows an intensity scan across the center of the image, quantifying the optical powers of the beams. There is a good correspondence between the electrical power of each frequency component in the drive signal (top plot), and the optical

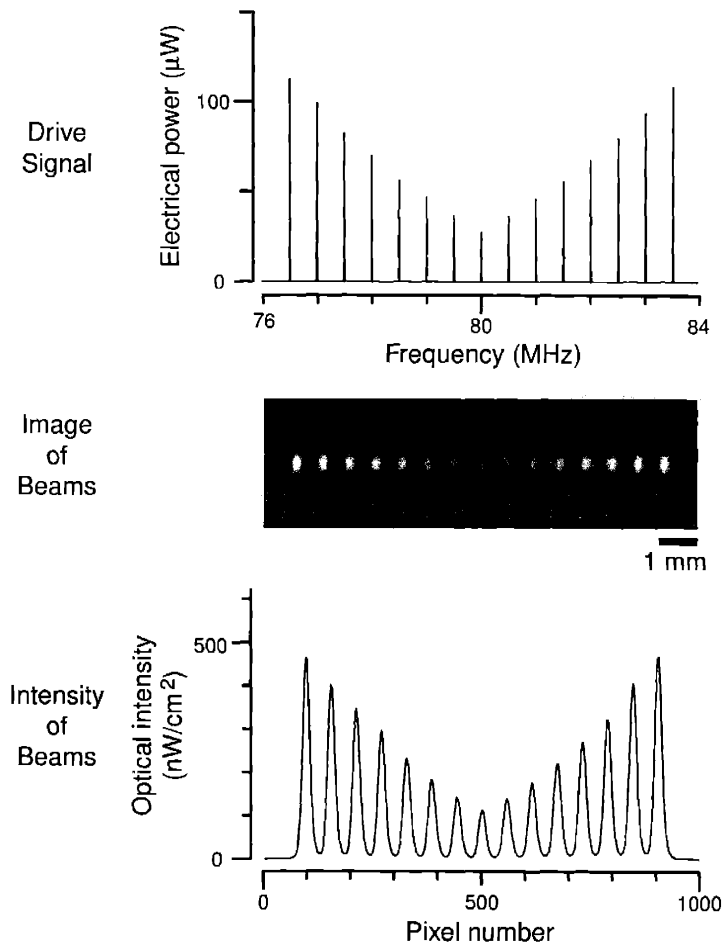

Figure 3-4: Controlling the amplitudes of the beams using an AOD. The top panel shows the power spectrum of the electrical signal driving the AOD, showing fifteen frequency components. The middle panel shows a CCD image of the output diffracted beams. The bottom plot shows an intensity scan horizontally through the center of the CCD image. The optical intensity values were calibrated using data provided by the CCD manufacturer. Data courtesy of S. S. Hong.

power of the corresponding output diffracted beam (bottom plot).

3.1.2 Phase control

The AOD can also be used to control the optical phase of each diffracted beam, by controlling the electrical phase of the corresponding frequency component of the drive signal.

Doppler Shift Compensation using Amplitude Modulator

However, the optical phase relationship of the diffracted beams set by the electrical drive is not maintained over time due to the Doppler shift effect. As beams are diffracted from the AOD crystal, they are frequency shifted by the drive frequency. In Figure 3-5, three drive frequencies and three resulting beams are shown*, each diffracted at an angle proportional to its drive frequency. The Doppler shift imparted to each beam causes its phase to drift relative to the input beam. If these beams were combined, they would form an interference pattern that would change in response to the changing relationships of the beam phases.

Careful choice of drive frequencies, however, can guarantee that a given relationship will repeat periodically. The laser power can then be gated to produce output beams only when the desired relationship repeats. Therefore, by combining the AOD for phase and amplitude control and the amplitude modulator for on/off switching, the desired phase relationship between the beams can be created, albeit in brief pulses rather than continuously.

The short laser strobes necessary to implement the above phase-control strategy were achieved with a KD*P crystal, prepared and packaged (ConOptics, Danbury, CT) with a high-quality polarizer. Such a crystal rotates polarization in proportion to an applied electric field, and in conjunction with a polarizer, acts as an amplitude modulator. The crystal assembly was mounted at the output of the argon laser. A custom high-speed (1.2 Gbps) digital channel, fully synchronized with the AOD drive electronics, was programmed to generate pulses of approximately 7 ns duration. A single sweep of this pulse is shown on the top trace of Figure 3-6.

These pulses were delivered by a coaxial cable to a high-voltage level shifter (ConOptics model 25D) which drove the KD*P crystal with the several hundred volt swing needed for best pulse extinction. A fiber optic delivered the modulated beam to a nanosecond-resolution photo-diode (Motorola MRD500) at the input of a digital oscilloscope (Tektronix TDS724D). The photoelectron current delivered into

*Assume the electrical amplitudes and phases of the three frequency components are the same.

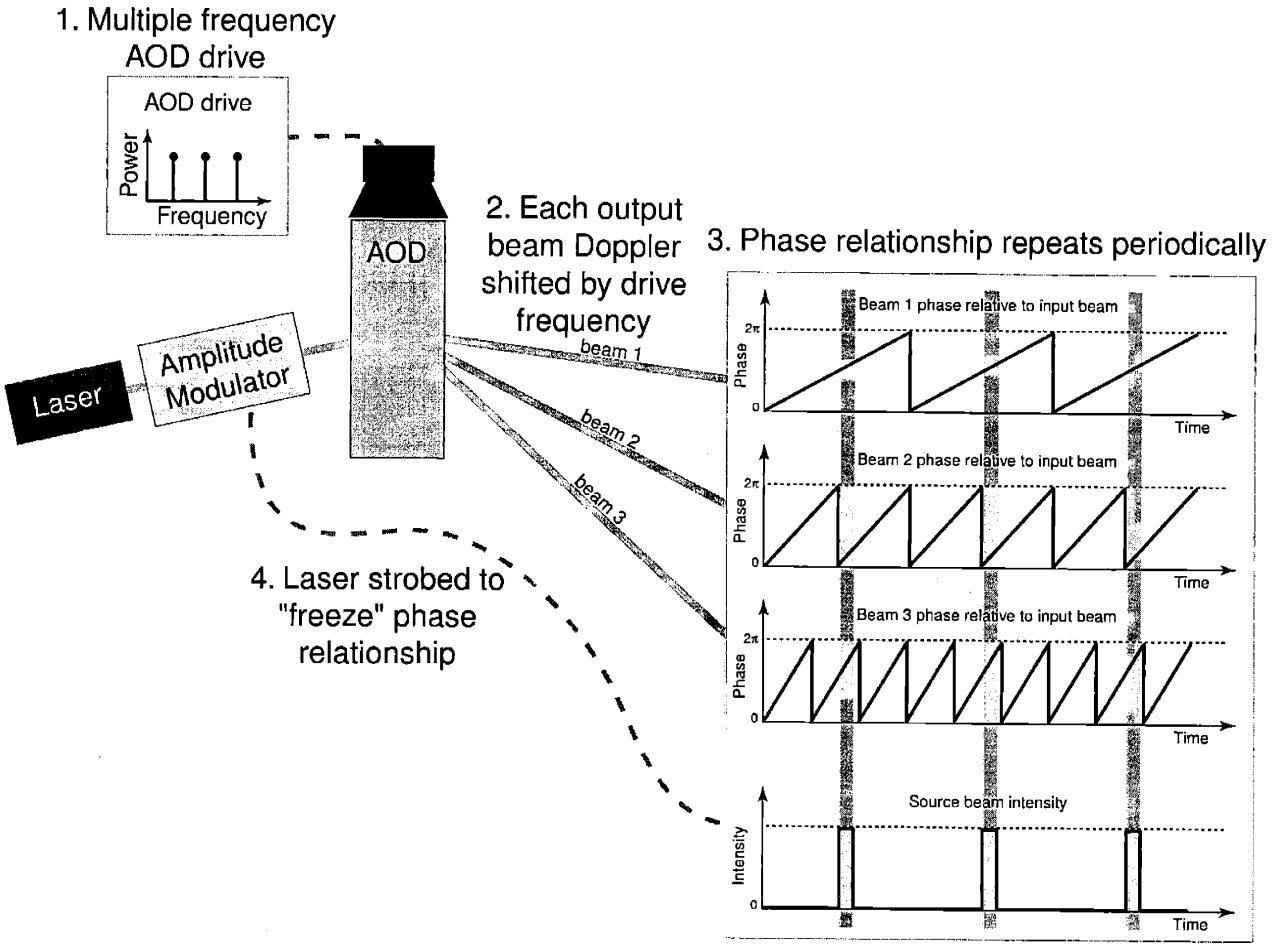

Figure 3-5: Frequency shift of the diffracted beams due to Doppler effect of the AOD. The figure illustrates production of three diffracted beams by the AOD when it is driven by an electrical drive with three frequency components. Due to the Doppler effect, each diffracted beam is frequency shifted by the corresponding frequency in the electrical drive. As a consequence, the phase relationship between the diffracted beams changes over time, as illustrated on the right. Proper choice of a set of drive frequencies, however, ensures that the same relationship repeats over time. The bottom plot on the right shows a pulse train driving the amplitude modulator, gating the source beam such that the output diffracted beams are produced only when the desired phase relationship holds.

the 50 ohm oscilloscope input registers the light strobe as a downward voltage pulse shown in Figure 3-6 as a single sweep (middle trace) and as an average of 33 sweeps (bottom trace).

Finally, Figure 3-7 shows an experimental demonstration of beam phase control. The AOD drive signal has two frequency components as shown on the left. The electrical phase of the first component was changed while the phase of the second

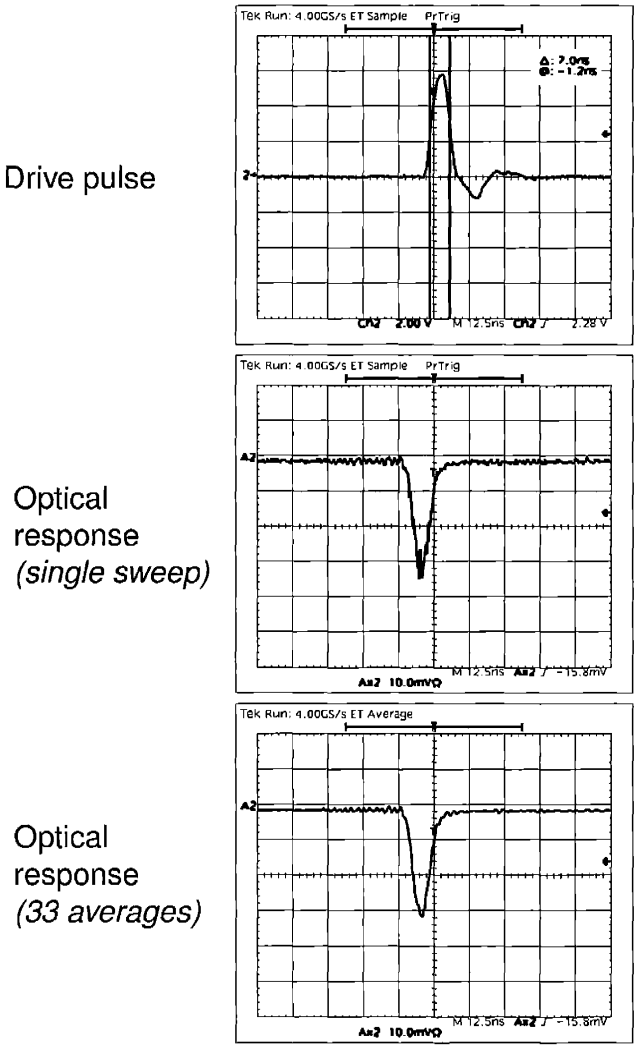

Figure 3-6: Strobing performance of the amplitude modulator. The top trace is a single sweep of pulses of approximately 7 ns duration. After passing through a high-voltage level shifter, the pulses drove the KD*P crystal in the amplitude modulator that gates the source beam according to the driving pulses. The middle traces show recordings from a photodiode coupled to the source beam. The bottom traces are an average of 33 sweeps. Data courtesy of M. S. Mermelstein.

component was fixed, resulting in the relative phase changing from $\pi/2$ to $-\pi$. This changing phase relationship was visualized by imaging the fringes formed by the interference of the two beams. The change in the relative phase of the two beams shows up as a change in the spatial phase of the resulting fringe pattern. The right side of Figure 3-7 shows systematic change in the spatial phase of the fringe due to beam modulation.

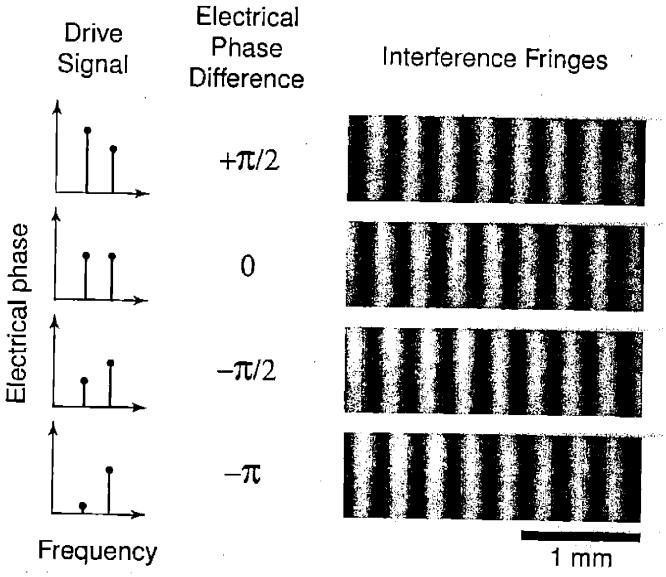

Figure 3-7: Controlling the phases of the beams using the AOD and the amplitude modulator. The plots on the left side show the change in the relative phases of the two frequency components of the electrical drive. While the electrical phase of the second component was fixed, the electrical phase of the first component was changed through four equally spaced points from zero to 2π. The images on the right side correspond to fringes formed by the interference of the two output diffracted beams for each case. Data courtesy of S. S. Hong

3.2 All-Reflective Beam Delivery

The output from the AOD is an array of diverging beams. For these beams to interfere, it is necessary to guide them into a converging cone of beams. This was done by building a beam delivery system made of a set of mirrors. Figure 3-8 (a) shows how this is done. The AOD is driven by an electrical signal with 31 frequency components. The diverging fan of beams produced from the AOD is guided into a converging cone by an assembly of small mirrors mounted beneath a half inch thick aluminum plate, Figure 3-8 (b). The upper right of Figure 3-8 (a) shows a schematic side view of the setup, illustrating the cone of beams.

Figure 3-8 (b) is a photograph of the mirror assembly seen from the bottom side of the aluminum plate. The mirrors outside the ring of mirrors in the photograph deliver the five clusters of output beams from the AOD through the gaps in the ring to the rows of pick-off mirrors. These mirrors select individual beams in a cluster and send them back towards the ring mirrors. These ring mirrors are the final optical

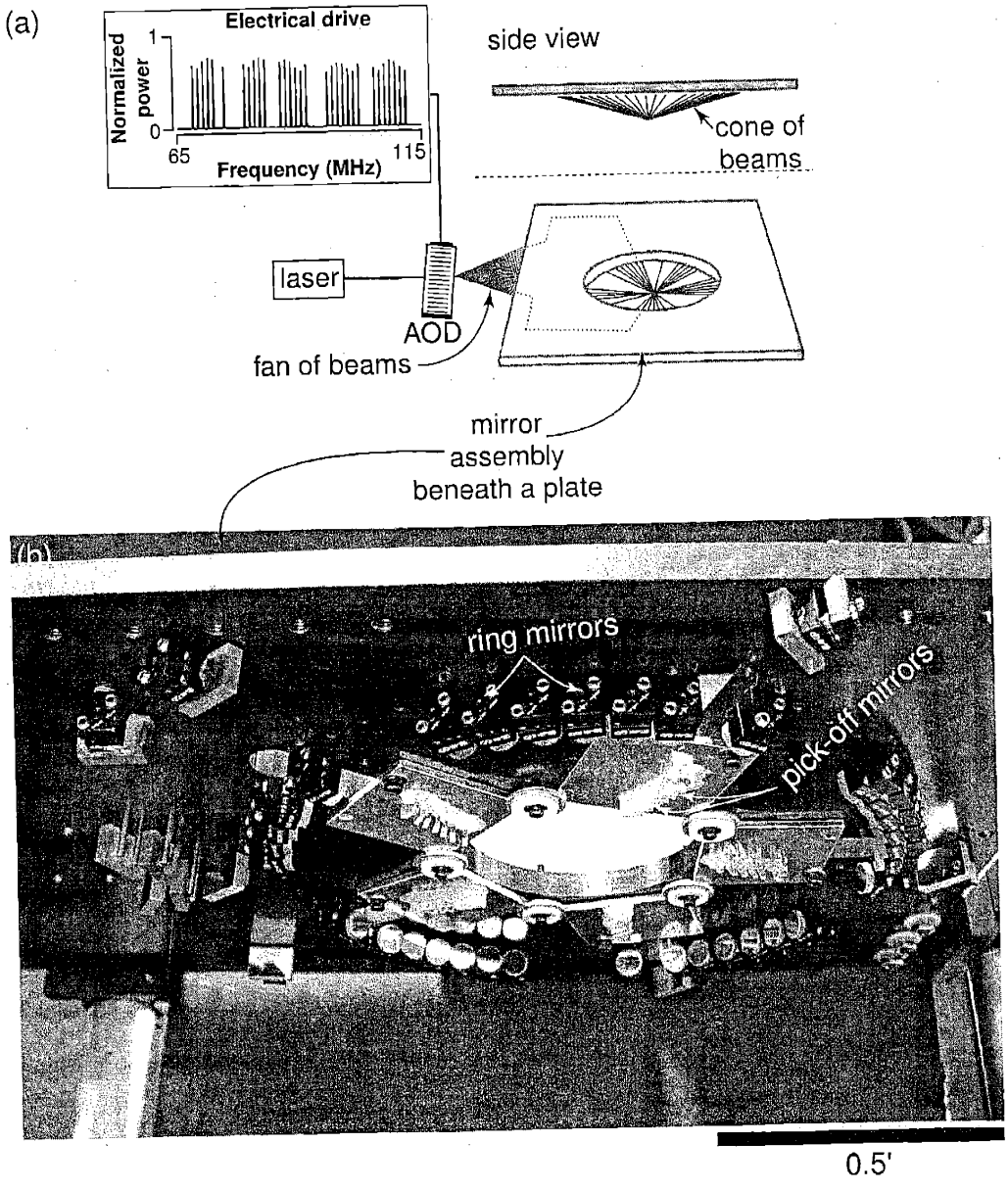

Figure 3-8: The beam delivery system. (a) A schematic illustration showing the conversion of an array of diffracted beams from the AOD into a converging cone of beams by an assembly of small mirrors (not shown) beneath a half inch thick aluminum plate. The plate was mounted 14 inches high from the optical table using four posts (not shown). The top left shows the power spectrum of the electrical drive of the AOD, with 31 distinct frequency components. The top right is a side view of the setup showing the cone of beams. (b) A photograph of the mirror assembly taken from the bottom side of the aluminum plate at an angle. The vertical orientation of the ring mirrors are slightly downwards, producing a cone of beams with a half cone angle of 78°.

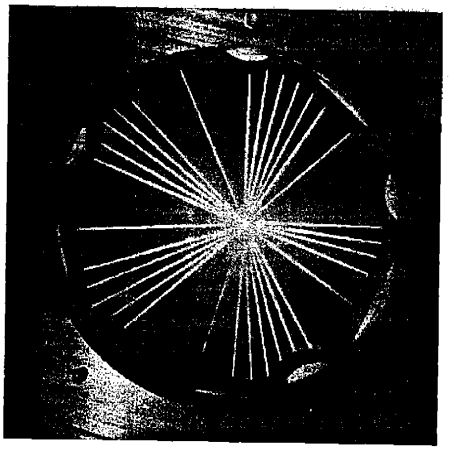

Figure 3-9: A cone of beams visualized through the opening of the aluminum plate.

elements hit by the beams before they converge and overlap at the target. The ring mirrors reflect the beams downward from the plane of the plate toward the center of the ring where all beams intersect and produce an interference pattern. The target is placed at the region where the beams intersect.

The design of the mirror assembly shown in Figure 3-8 is based on a computer optimization aimed at maximizing the number of beams that can be handled per mirror. The system design also minimizes the differences in the optical path lengths of the beams and matches the polarizations (Transverse Magnetic (TM)) of the beams. The cone angle of the cone of beams is determined by the vertical orientation of the ring mirrors, which can be manually controlled. In the imaging experiments described in the following chapters, the half cone angle was set to be 78°, resulting in a *synthesized* aperture of 0.98 for the projector. With this cone angle, the polarization vectors of the beams are approximately equal.

The photograph in Figure 3-9 shows a cone of 31 laser beams in the projector visualized through the opening in the plate from the top. The bright spot at the center is where the beams overlap and the target will be placed.

In chapter 6, it will be demonstrated that the converging cone of beams delivered by the apparatus shown in Figure 3-8 is the primary source of resolution in the structured illumination approach. Notice that the beam delivery apparatus in Figure 3-8 is made of reflective optical elements only, which can handle short wavelengths of

light such as UV and X-ray. Although a blue laser (488 nm wavelength) was used in this thesis for proof-of-concept demonstration purposes, we have an opportunity to improve the resolution of the system beyond what is possible with the visible wavelengths by scaling to UV and X-ray. Such scaling is not possible with the conventional lens system.

Chapter 4

Multiple-Beam Interference Pattern Projector: Calibration Algorithms

4.1 Introduction

In the previous chapter, a physical setup that projects interference patterns formed by a converging cone of 31 laser beams was described. To make use of the interference pattern, precise knowledge of it is required. According to Eq. (2.3), the interference pattern is determined by the amplitudes, phases, and directions of the beams that produce it. An important problem here is that these beam parameters are not known in the region of interference.

This problem is illustrated in Figure 4-1. As described in the previous chapter, the amplitude and phase of each of the diffracted beams can be controlled using the electrical signal that drives the AOD. However, the control location, which is the point where the diffracted beams are produced, is separated from the target location, the region where the beams overlap and produce the interference pattern. What lies between these two points is the system of mirrors.

In an ideal situation, the system of mirrors needs to be built so that it provides

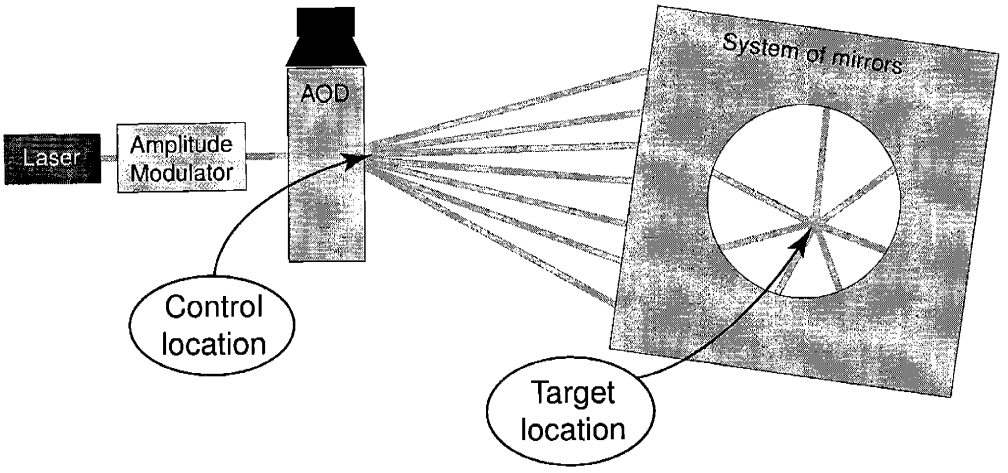

Figure 4-1: Separation between the control location and the target location. The amplitudes and the phases of the diffracted beams from the AOD are electronically controlled where the beams are produced (*control location*). However, these values become unknown at the *target location* because the beams are attenuated differently and their optical path lengths are not exactly identical as they are delivered by the system of mirrors.

control over the beams with precision similar to a lens. That is, the positions of the individual mirrors need to be determined so that optical path lengths of all beams are the same, and all the beams undergo the same attenuation in amplitude as they pass through the system of mirrors. Building such a system is almost impossible in a practical sense, especially when the wavelength of the source beam is reduced and the corresponding precision requirement increases. Even if this can be done, small environmental perturbations (e.g., change in temperature, humidity, etc.) will change the system over time.

Instead of building a physically perfect system, a beam calibration method was newly developed to determine the amplitudes, phases, and directions of the beams in the region of interference. The developed calibration method can be done in a dynamic fashion, which makes it possible to account for the change in the system due to environmental perturbations. The difference between the beam parameters *commanded* using the AOD and the parameters *calibrated* in the region of interference will represent imperfections in the physical system at the time of calibration. Therefore, the developed calibration technique provides a way to dynamically access imperfections in the physical system and compensate for them.

Previously, an image-based method was developed to calibrate the beam parameters in the region of interference (Mermelstein, 2000c). In this method, the beam parameters are determined by analyzing an image of the interference pattern acquired using a lens and a CCD. However, several limitations exist in the image-based method. First, the beams travel at an angle relative to the optical axis of the imaging lens and therefore will be bent upon passing through the lens, which can affect the polarizations of the beams. As a result, optical pattern projected onto the CCD will be different from the original interference pattern. Secondly, a high resolution imaging setup is required for calibration, in addition to a low resolution setup for acquiring imaging data. As a result, calibration data and imaging data are acquired, each using different sensors and at separate times. In this case, the positional alignment between the two setups and any change in the system over time become important issues. Finally, the image-based method will eventually fail to work as the wavelength of light is reduced beyond that of visible light.

The beam calibration method presented in this chapter overcomes the above limitations of the previous method. The new method uses a sparse array of fluorescent microspheres as a calibration target, and is based on measuring the total number of photons emitted from each microsphere, when it is illuminated by an interference pattern. The method does not rely on imaging the interference pattern using a lens and a camera. Therefore, the calibration data is acquired simultaneously with the imaging data using the same low resolution sensors on the imaging side.

4.2 Data acquisition

4.2.1 Calibration target

The calibration target is made of a sparse, random monolayer of fluorescent microspheres. The original solution of fluorescent polystyrene microspheres (model T-8880, Molecular Probes, Inc., Eugene, Oregon, 1.0μm diameter, 30 nm standard deviation) is diluted by mixing it with ethanol (1:200 dilution) and then sonicated for 3 minutes

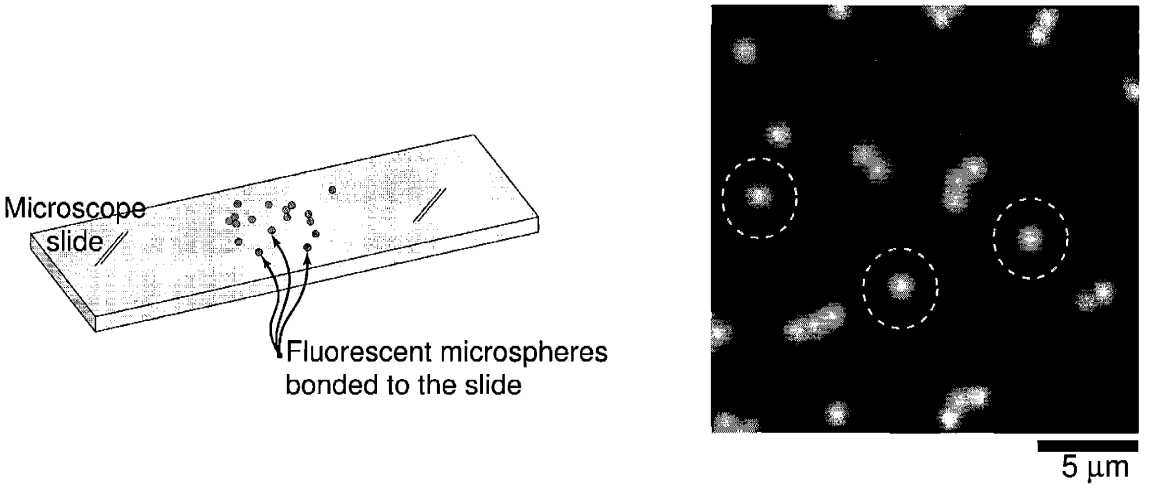

Figure 4-2: Left: an illustration of a sparse and random monolayer of fluorescent microspheres on a glass substrate used as a calibration target. The microspheres are bonded to the glass substrate due to electrostatic attraction between their surface and the substrate. Right: a high resolution optical microscopy (NA = 0.6) image of a sub-region of the calibration target showing several isolated microspheres, (marked by the dotted circles) together with several clusters of microspheres. The diameter of the microspheres is 1.0 μm with a standard deviation of 30 nm. The size of the microsphere was selected to be comparable to the wavelength of light (488 nm) so that the microspheres can spatially sample the interference pattern.

to separate individual microspheres. A 1 μl drop of the solution is then drop-coated to the surface of a microscope slide. The solution spreads out evenly along the surface of the microscope slide. After the ethanol evaporates, the microspheres are bonded to the glass substrate because of negatively charged carboxyl groups on their surfaces. This procedure creates a random monolayer of microspheres (Figure 4-2). The sparseness of the microspheres can be controlled by varying the concentration of the microspheres in the solution. The peaks of the excitation and the emission spectra of the fluorescent dye that coats the microsphere are 488 and 560 nm, respectively.

4.2.2 A series of high resolution illuminations

Similar to the imaging data acquisition procedure outlined in Chapter 2, calibration data consists of a series of low resolution images of the calibration target when it is illuminated by a sequence of light patterns. In fact, the same sequence of patterns is used in both calibration and imaging. Each illumination pattern is a fringe, a two

dimensional sinusoidal brightness grating, made by a pair of interfering beams.

Fringes, produced by a pair of beams, were chosen for each illumination pattern primarily because the AOD exhibits intermodulation when excited with multiple frequencies (Elston, 1985). Creation of nonlinear distortion products results in cross talk between independent channels. This effect becomes more significant as the number of channels grows. Producing only two beams at a time using the AOD minimizes the effect of intermodulation. A sequence of structured illumination using pairs of beams corresponds to a special case of the more general situation described in Chapter 2. In fact, post-processing the raw data for this case becomes relatively more straightforward compared with illumination using more than two beams at a time, as will be described in the following sections.

Several terms for the parameters of a fringe to be calibrated are defined here. The spatial variation of light intensity of a fringe formed by the interference of a pair of beams (i and j) with equal wavelengths is described by the following expression,

$$f_{ij}(\mathbf{r}) = \frac{1}{2}(a_i^2 + a_j^2) + a_i a_j \cos((\mathbf{k}_i - \mathbf{k}_j) \cdot \mathbf{r} + (\phi_i - \phi_j))\hat{\mathbf{p}}_i \cdot \hat{\mathbf{p}}_j \qquad (4.1)$$

where a_i, ϕ_i, $\mathbf{k}_i$, and $\hat{\mathbf{p}}_i$ are the amplitude, phase, wavenumber, and polarization vector of the beam i. Eq. (4.1) can be simplified to

$$f_{ij}(\mathbf{r}) = c_{ij}^0 + c_{ij}^1 \cos(\mathbf{k}_{ij} \cdot \mathbf{r} + \phi_{ij}) \qquad (4.2)$$

where $c_{ij}^0 = \frac{1}{2}(a_i^2 + a_j^2)$ and $c_{ij}^1 = a_i a_j \hat{\mathbf{p}}_i \cdot \hat{\mathbf{p}}_j$ are defined as the DC and AC amplitudes of the fringe and $\mathbf{k}_{ij} = \mathbf{k}_i - \mathbf{k}_j$ and $\phi_{ij} = \phi_i - \phi_j$ the spatial frequency of the fringe and the spatial phase of the fringe. This function describes a raised cosine function with spatial average intensity c_{ij}^0 and minimum and maximum values $c_{ij}^0 \pm c_{ij}^1$. Note that the minimum value $c_{ij}^0 - c_{ij}^1$ can not be smaller than zero.

4.2.3 A series of low resolution images

For each illumination pattern, an image of the calibration target was acquired using the same microscope objective and CCD used for acquiring imaging data. Figure 4-3 (a) illustrates a schematic of the setup. The figure shows a pair of diffracted beams (i and j) emerging from the AOD when it is driven by an electrical signal with two frequency components. A fringe formed by the interference of the two beams illuminates the calibration target. A microscope objective with 0.2 NA (Epiplan-10x, Carl Zeiss, Oberkochem, Germany) and an 8-bit CCD camera (CA-DA-1024A, Dalsa, Colorado Springs, Colorado) with pixel size of 10μm were used to acquire an image of the calibration target illuminated by the fringe. The λ filter (CG-OG-512-2×2-3, CVI Laser Corp., Albuquerque, NM) blocks any illumination light scattered or reflected from the stage but passes the light fluoresced from the target excited by the illumination.

In the plot at the top left corner of Figure 4-3 (a), η_i and η_j, the electrical phases of the two frequency components of the AOD drive are illustrated. While fixing η_i at 0, the value of η_j was changed from 0 to 2π, at 16 equally spaced phases. This results in a sequential shift of the phase of the beam j relative to that of beam i. Each time η_j was changed, an image of the calibration target was acquired with a CCD exposure time of 40 msec, resulting in a total of 16 images for every beam pair.

The above procedure was repeated for the 82 different pairs of beams that are available from the 31 beam projector shown in Figure 3-9. This resulted in a total of $16 \times 82 = 1312$ images acquired. At 40 msec exposure time, acquisition time of the entire data set was roughly 1 minute. In the analysis that follows, we assume that system perturbations during this time period are negligible, which will be verified through the analysis results.

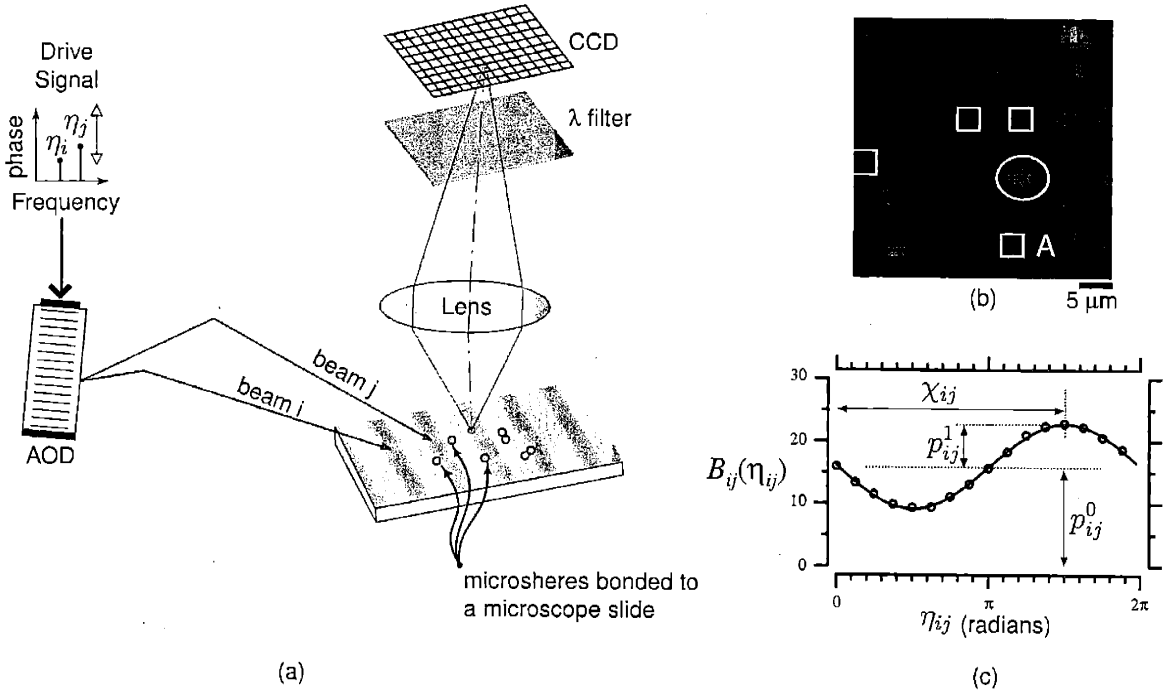

Figure 4-3: (a) Schematic of the calibration setup. A pair of beams (i and j) from the AOD interfere at the calibration target region to form a fringe that illuminates the target. The beam delivery optics between the AOD and the target are not shown. The top left plot shows the electrical phases (η_i and η_j) of the two frequency components of the AOD drive signal. The electrical phase of the second component (η_j) was modulated at 16 equally spaced phases from 0 to 2π while the electrical phase of the first component (η_i) remains the same. The electrical amplitudes of the two components were set to be equal. Each time the phase was changed, an image of the calibration target was acquired using a microscope objective with 0.20 NA and a CCD. A long-pass filter (λ filter) was used to selectively collect only the light fluoresced from the target. (b) An image of the target illuminated by a fringe made by a particular pair of beams. Isolated microspheres are marked by surrounding rectangles. The region marked by an oval circle contains a cluster of more than one microsphere. (c) The measured brightness of the microsphere A in part (b) plotted against $\eta_{ij} = \eta_i - \eta_j$. Circles are measured brightness and the curve is the least-square fit of the data points to a raised cosine function. The three parameters of the best-fit sinusoidal function are also indicated in the plot.

4.3 Analysis and results: Fringe amplitudes and phases

An image of the calibration target illuminated by a particular fringe is shown in Figure 4-3 (b). Notice that the shapes of the microspheres are not resolved due to the low imaging resolution. However, their brightnesses can be determined from the image.

In Chapter 2, it was shown that a sequence of brightnesses values contains target information when the sequence of illuminations is known. Conversely, a sequence of brightnesses contains information about the illuminations if the target it known. The microspheres with highly regular diameters and fluorescent responses are a known target.

Suppose we know that each of the rectangular regions in Figure 4-3 (b) contains a single microsphere. This can be verified by imaging the calibration target using high resolution microscopy, or more efficiently, can be verified from the calibration data itself, as will be described in the following section. The brightness of a microsphere (for example, the one in region A in the image) can be quantified by summing the pixel values that make up the image of the microsphere.

Figure 4-3 (c) shows a plot of 16 measured brightnesses of a single microsphere vs. the electrical phase difference between the two frequency components of the AOD drive ($\eta_{ij} = \eta_i - \eta_j$). The circles are the data points and the curve is the least-squares fit of the data to a raised cosine function. The three parameters of the best-fit sinusoidal function, p_{ij}^0, p_{ij}^1, and χ_{ij}, are defined in the plot.

4.3.1 Mathematical models

The brightness data in Figure 4-3 (c) can be interpreted as samples of the convolution of the microsphere and the fringe. Suppose $s(\mathbf{r})$ represents the microsphere and $f_{ij}(\mathbf{r})$ represents a fringe formed by beam i and j when $\eta_i = \eta_j$ in Figure 4-3, that is, when the phases of the two beams are set to be the same by AOD. The brightness B_{ij} of the microsphere illuminated by the fringe $f_{ij}(\mathbf{r})$ becomes

$$B_{ij} = \int s(\mathbf{r}) \cdot f_{ij}(\mathbf{r}) d\mathbf{r}. \tag{4.3}$$

Now, if a phase delay is introduced to one beam while keeping the phase of the other beam fixed, making $\eta_{ij} = \eta_i - \eta_j$ taking a non-zero value, the resulting displacement of the fringe is $\mathbf{r}_{\eta_{ij}}$, defined by

$$\mathbf{k}_{ij} \cdot \mathbf{r}_{\eta_{ij}} = \eta_{ij} \tag{4.4}$$

where $\mathbf{k}_{ij}$ is the fringe frequency. Now the expression for the shifted fringe is described by $f_{ij}(\mathbf{r}_\theta - \mathbf{r})$, and Eq. (4.3) becomes:

$$B_{ij}(\eta_{ij}) = \int s(\mathbf{r}) \cdot f_{ij}(\mathbf{r}_{\eta_{ij}} - \mathbf{r}) d\mathbf{r} \tag{4.5}$$

$$= [s(\mathbf{r}) * f_{ij}(\mathbf{r})]_{\mathbf{r}=\mathbf{r}_{\eta_{ij}}}. \tag{4.6}$$

The right side of Eq. (4.5) is the convolution of $s(\mathbf{r})$ and $f_{ij}(\mathbf{r})$ evaluated at $\mathbf{r} = \mathbf{r}_{\eta_{ij}}$. The left side of the same equation is determined from the brightness data such as shown in Figure 4-3 (c):

$$B_{ij}(\eta_{ij}) = p_{ij}^0 + p_{ij}^1 \cos(\eta_{ij} + \chi_{ij}) \tag{4.7}$$

$$= p_{ij}^0 + p_{ij}^1 \cos(\mathbf{k}_{ij} \cdot \mathbf{r}_{\eta_{ij}} + \chi_{ij}) \tag{4.8}$$

where p_{ij}^0, p_{ij}^1, and χ_{ij} are the parameters of the best-fit sinusoidal function of the brightness data defined in Figure 4-3 (c) and Eq. (4.4) was used in Eq. (4.8).

From Eq. (4.6) and Eq. (4.8), the following expression can be obtained:

$$s(\mathbf{r}) * f_{ij}(\mathbf{r}) = p_{ij}^0 + p_{ij}^1 \cos(\mathbf{k}_{ij} \cdot \mathbf{r} + \chi_{ij}). \tag{4.9}$$

The top part of Figure 4-4 shows a schematic illustration of $\mathbf{S}(\mathbf{k})$, the Fourier transform of $s(\mathbf{r})$. Values of the transform at DC ($\mathbf{k} = 0$) and at $\mathbf{k} = \pm\mathbf{k}_{ij}$ are shown in the plot. The middle part corresponds to $\mathbf{F}_{ij}(\mathbf{k})$, the Fourier transform of $f_{ij}(\mathbf{r})$ in Eq. (4.2). Values of the Fourier transform $\mathbf{F}_{ij}(\mathbf{k})$ at DC and at $\mathbf{k} = \pm\mathbf{k}_{ij}$ determined from Eq. (4.2) are shown in the plot. The bottom part corresponds to $\mathbf{S}(\mathbf{k})\mathbf{F}_{ij}(\mathbf{k})$, the Fourier transform of $s(\mathbf{r}) * f_{ij}(\mathbf{r})$ in Eq. (4.9). The values of the transform at DC and at $\pm\mathbf{k}_{ij}$ are the products of corresponding values of $\mathbf{S}(\mathbf{k})$ and $\mathbf{F}_{ij}(\mathbf{k})$ and are shown in the plot. In the same plot, these transform values are equated to the corresponding values from Eq. (4.9).

From the equations in the bottom part of Figure 4-4, the following expressions to determine the DC and AC amplitudes, c_{ij}^0 and c_{ij}^1, and phase, ϕ_{ij}, of a fringe can be

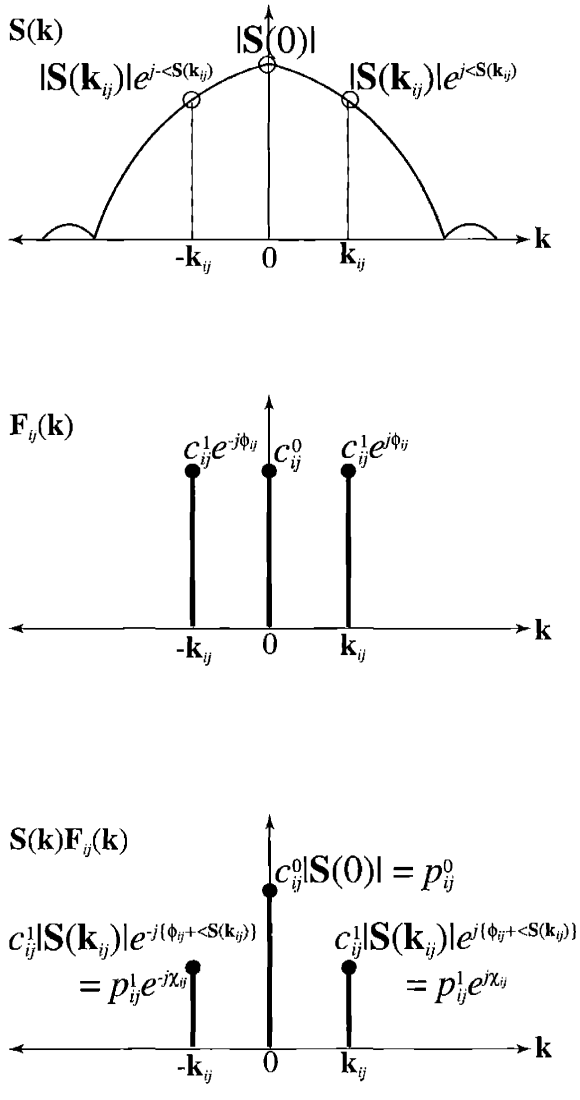

Figure 4-4: Top: A schematic drawing of the Fourier transform $\mathbf{S}(\mathbf{k})$ of the miscrosphere intensity function $s(\mathbf{r})$. The values of the transform at DC ($\mathbf{k} = 0$) and at $\mathbf{k} = \pm\mathbf{k}_{ij}$ are shown in the plot. Middle: Fourier transform $\mathbf{F}_{ij}(\mathbf{k})$ of the fringe function $f_{ij}(\mathbf{r})$ in Eq. (4.2). Its three frequency components and their transform values are shown. Bottom: Fourier transform of the convolution of $s(\mathbf{r})$ and $f_{ij}(\mathbf{r})$ in Eq. (4.9).

derived:

$$c_{ij}^0 = \frac{p_{ij}^0}{|\mathbf{S}(0)|} \tag{4.10}$$

$$c_{ij}^1 = \frac{p_{ij}^1}{|\mathbf{S}(\mathbf{k}_{ij})|} \tag{4.11}$$

$$\phi_{ij} = \chi_{ij} - \angle\mathbf{S}(\mathbf{k}_{ij}). \tag{4.12}$$

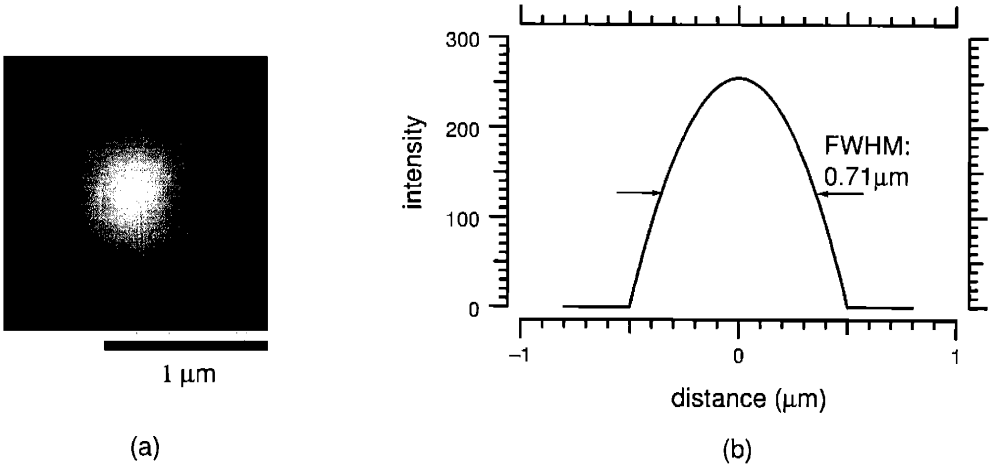

Figure 4-5: (a) A simulated 1 μm diameter microsphere calculated using the model of Eq. (4.13). (b) Intensity scan through the center. The full width half maximum (FWHM) of the intensity scan is 0.71 μm.

Notice that data from a single microsphere is sufficient in estimating the fringe amplitudes and phases.

To determine the fringe parameters using Eq. (4.10, 4.11, 4.12), it is necessary to know the Fourier transform of the microsphere $\mathbf{S}(\mathbf{k})$, which is calculated using a model of the intensity function $s(\mathbf{r})$ of a microsphere. The following model assumes that the amount of dye fluorescence at a point on the surface of a microsphere is proportional to the square of the height of that point from the substrate:

$$s(\mathbf{r}) = \begin{cases} \alpha[(\frac{d}{2})^2 - |\mathbf{r} - \mathbf{r}_c|^2], & |\mathbf{r} - \mathbf{r}_c| \leq \frac{d}{2} \\ 0, & \text{elsewhere} \end{cases} \tag{4.13}$$

where d and $\mathbf{r}_c$ are the diameter and the center position of the microsphere and α is a proportionality constant.

Figure 4-5 (a) shows a simulated 1 μm diameter microsphere based on the above model and Figure 4-5 (b) shows an intensity scan through the center of the microsphere in (a).

4.3.2 Fringe amplitudes

The DC and the AC amplitudes of the fringe, c_{ij}^0 and c_{ij}^1, can be determined using Eq. (4.10) and Eq. (4.11). Calculation of $|\mathbf{S}(\mathbf{k}_{ij})|$ using the model in Eq. (4.13) requires that $\mathbf{k}_{ij}$ itself be known. Therefore, determination of the fringe amplitudes is done after the fringe frequencies are determined.

Figure 4-6 shows the estimated c_{ij}^0's and c_{ij}^1's at a set of $\mathbf{k}_{ij}$'s. The $\mathbf{k}_{ij}$'s were estimated using the method described in the following section. Each microsphere produces estimates of fringe amplitudes at the location of the microsphere. The results shown correspond to averaged values for 12 different microspheres. The amplitudes are reported in dB.

The plots at the bottom of Figure 4-6 display the same data at the top, plotted against the radial frequencies ($k_r = \sqrt{k_x^2 + k_y^2}$)*. From the radial frequency plots, fringes can be grouped into four sub-groups, depending on their radial frequencies. The radial frequency of a fringe is determined by the angular separation between the two beams producing the fringe. Notice that the AC amplitudes of the fringes decrease significantly with increase in radial frequencies. The calibration results also show that, for fringes within the same sub-group that have similar radial frequencies, there exist about 5 dB variations in their DC and AC amplitudes.

Main factor contributing these variations is the non-uniformity in the amplitudes of the beams. Due to the frequency response of the AOD, the amplitudes of an array of diffracted beams produced from the AOD gradually decrease, going from lower frequency beams (beams that are produced using lower frequency electrical signals) to higher frequency beams (beams produced using higher frequency signals). This tapering of the amplitudes of the beams becomes significant when the frequency of the electrical signal becomes higher than about 85 MHz†.

However, an important point here is that the non-uniformity in the amplitudes of the beams can be effectively compensated using the calibration results shown in

*Estimated spatial frequencies of fringes in two-dimensional Fourier domain are shown in Figure 4-14

†The frequencies of the electrical signal fall within a range from 65 MHz to 115 MHz, as shown in the top left plot in Figure 3-8(a)

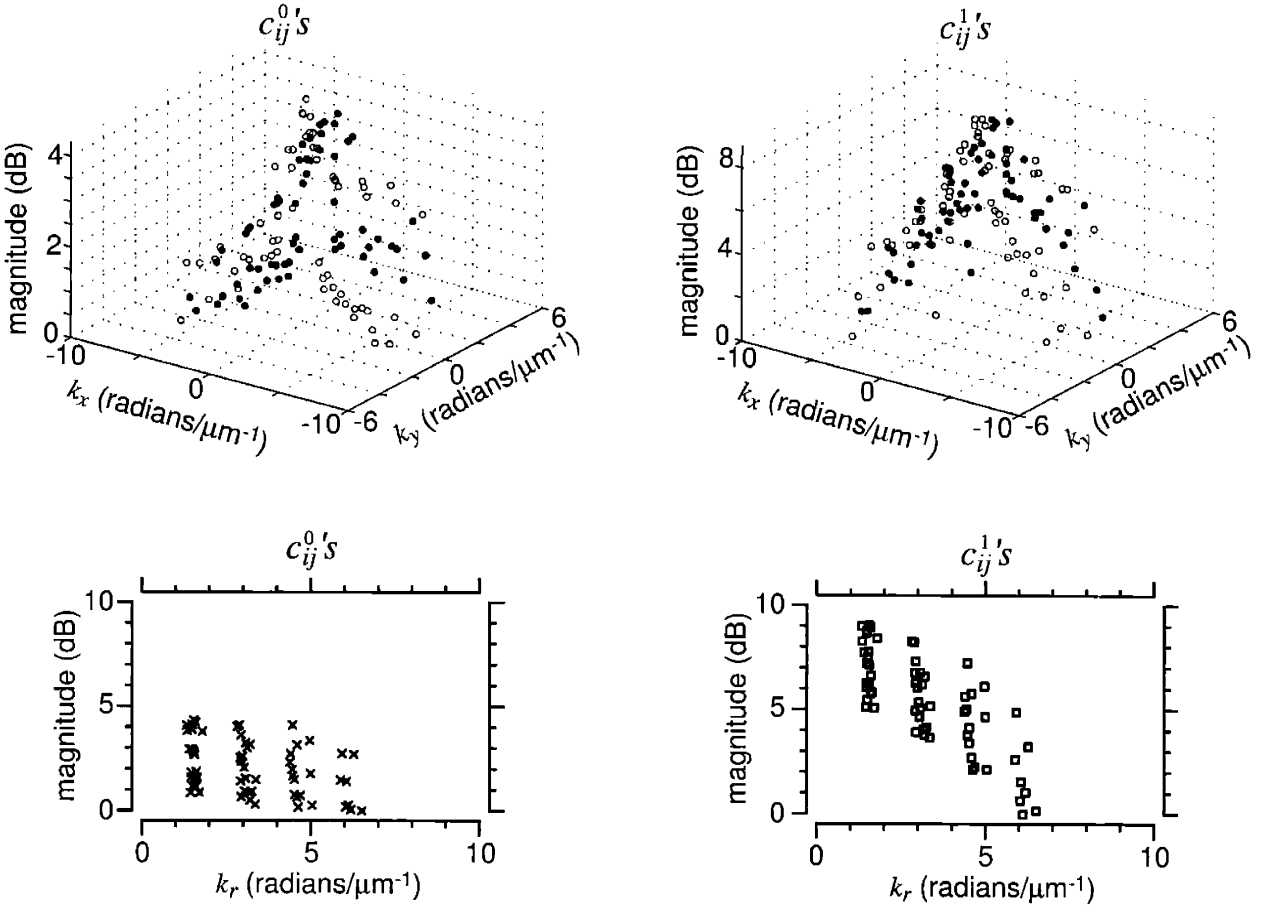

Figure 4-6: The estimated DC amplitudes (c_{ij}^0's, left) and AC amplitudes (c_{ij}^1's, right) for 62 fringes. The set of fringes is represented in Fourier domain by a total of 125 frequencies. The top plots show the DC (left) and AC (right) amplitudes at these frequencies (points in the k_x-k_y plane) in dB. The filled data points and the unfilled ones are for conjugate frequencies of each other. The plots at the bottom show the same data at the top plotted against the radial frequencies ($k_r = \sqrt{k_x^2 + k_y^2}$)

Figure 4-6.

4.3.3 Fringe phases

The definition of phase always requires a reference position, which may be chosen arbitrarily. Here, the phase reference point for every fringe is set to be the center of a microsphere. Under this condition, the phases of all frequency components of $\mathbf{S}(\mathbf{k})$ are assumed to be zero, that is, $\angle\mathbf{S}(\mathbf{k}_{ij}) = 0$ for any $\mathbf{k}_{ij}$ in Eq. (4.12). Therefore,

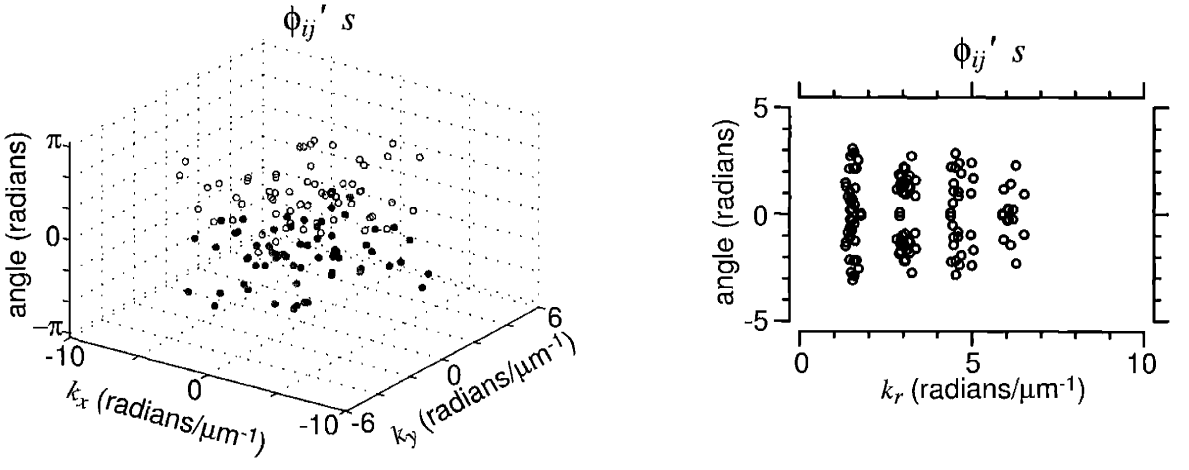

Figure 4-7: The estimated phases (ϕ_{ij}'s) for 62 fringes. The plot on the left shows the phases at 125 frequencies (points in the k_x-k_y plane) in radians. The filled data points and the unfilled ones are for conjugate frequencies of each other. The plot on the right shows the same data plotted against the radial frequencies.

Eq. (4.12) becomes:

$$\phi_{ij} = \chi_{ij} \tag{4.14}$$

and the fringe phase can be determined directly from the brightness data shown in Figure 4-3 (c). Figure 4-7 shows estimated fringe phases (ϕ_{ij}'s) for the same set of fringes in Figure 4-6 measured from a particular microsphere.

Accuracy of phase estimates

The estimated fringe phase ϕ_{ij} is the difference between the phases of the two beams, $\phi_i - \phi_j$. If the fringe phases for many beam pairs are measured, the estimates of the phases of the individual beams are over-determined. The validity of the over-determined data set can be assessed by checking its internal consistency.

For a beam triplet, beam i, j, and k, the following relationship between their phases should hold:

$$\phi_{ij} + \phi_{jk} = \phi_{ik}. \tag{4.15}$$

According to Eq. (4.14), χ_{ij} is an estimate of ϕ_{ij}. Therefore, if the phase estimates

are internally consistent, Eq. (4.15) becomes:

$$\chi_{ij} + \chi_{jk} = \chi_{ik}. \tag{4.16}$$

The top panel of Figure 4-8 (b) shows a plot of $\chi_{ij} + \chi_{jk}$ vs. χ_{ik} for a total of 95 beam triplets. The plot was generated using data from a single microsphere in the region A in Figure 4-8 (a). Each data point in the plot comes from a particular beam triplet. If the relationship in Eq. (4.16) is satisfied, all data points in the plot should fall on a straight line through the origin with a slope of one.

For a particular beam triplet, i, j, and k, a metric representing the deviation from the above rule of Eq. (4.16) can be defined:

$$E_{ijk} = \chi_{ij} + \chi_{jk} - \chi_{ik}. \tag{4.17}$$

For the data shown in the top panel of Figure 4-8 (b), the mean and the standard deviation of E_{ijk} are -0.11 radians (1.75 % of 2π) and 0.20 radians (3.18 % of 2π), respectively.

In an ideal condition, E_{ijk} is zero for all beam triplets. Ensemble statistics of the metric E_{ijk} can be regarded as quantitative measures of the self-consistency of the phase measurements. The phase inconsistency observed in the data results from factors such as 1) noise in the measurement system and 2) any change in the system during data acquisition (e.g., stage drift).

Beam triplet analysis in this way shows that the phase estimation error grows as the angular separation between a pair of beams increases. In Figure 4-9, beam triplets are grouped into four groups depending on the angular separation between the two outer beams in the triplet (the angle α). For each triplet sub-group, a histogram of E_{ijk}, and its standard deviation are shown. The standard deviation increases as the angle α increases.

As the angular separation between a pair of beams increases, the spatial frequency of their interference fringe increases. If we define the pitch of the fringe (L) as the

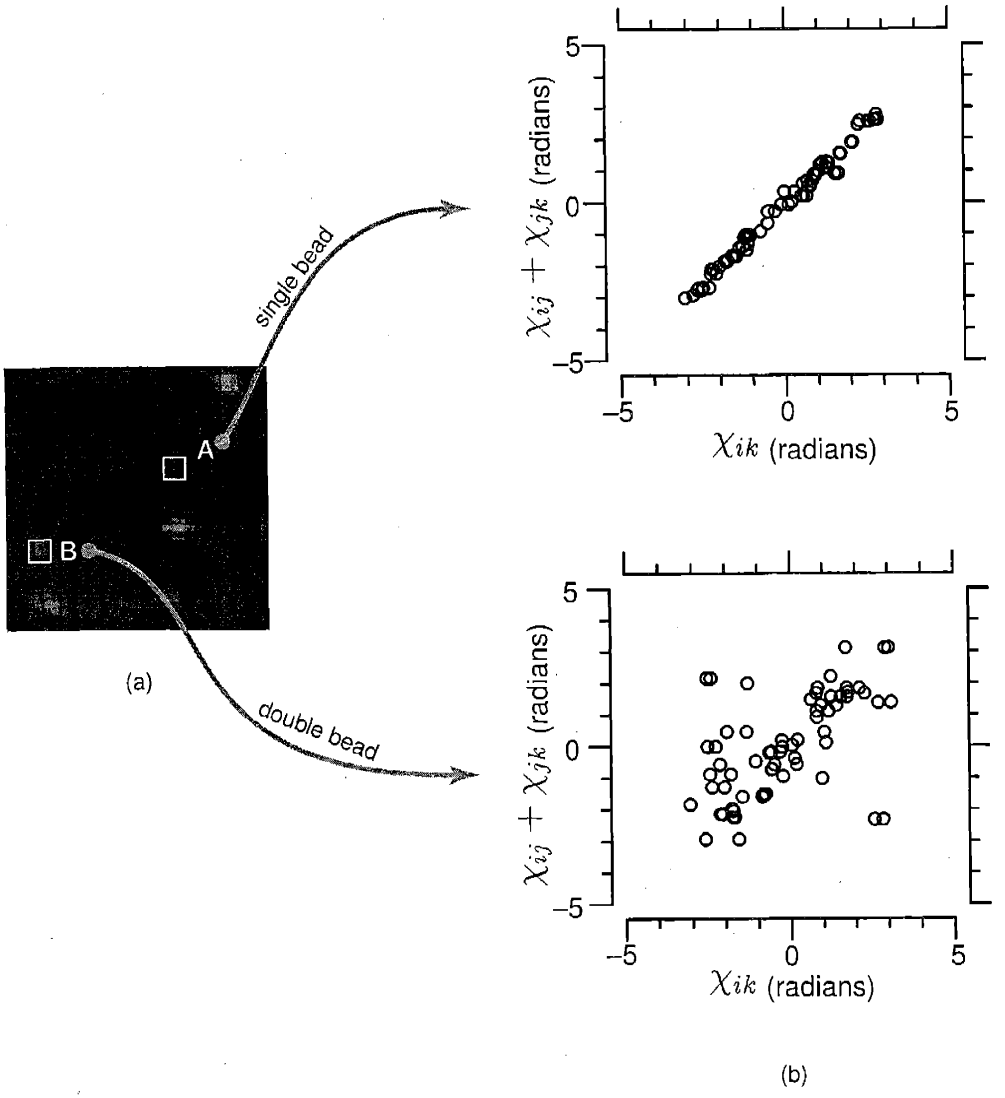

Figure 4-8: (a) An image of the sample illuminated by a fringe pattern. Two regions are marked by rectangles. The region A contains a single, isolated bead and the region B contains two beads that are adjacent to each other. This was verified by imaging the sample using a higher NA (0.60) lens in a Zeiss Axioplan microscope. Notice that it is not straightforward to determine whether each region contains a single bead or not just from the low-resolution image shown. (b) The result of the beam triplet phase consistency check described in the text for the two regions. The mean and the standard deviation of $E_{i,j,k}$ for all beam triplets were -0.11 radians and 0.20 radians for the data from region A (top panel), and 0.06 radians and 1.01 radians for region B (bottom panel), respectively.

distance between the adjacent bright peaks in the fringe, it is determined by:

$$L = \frac{\lambda \sin(\theta)}{2 \sin(\alpha/2)} \tag{4.18}$$

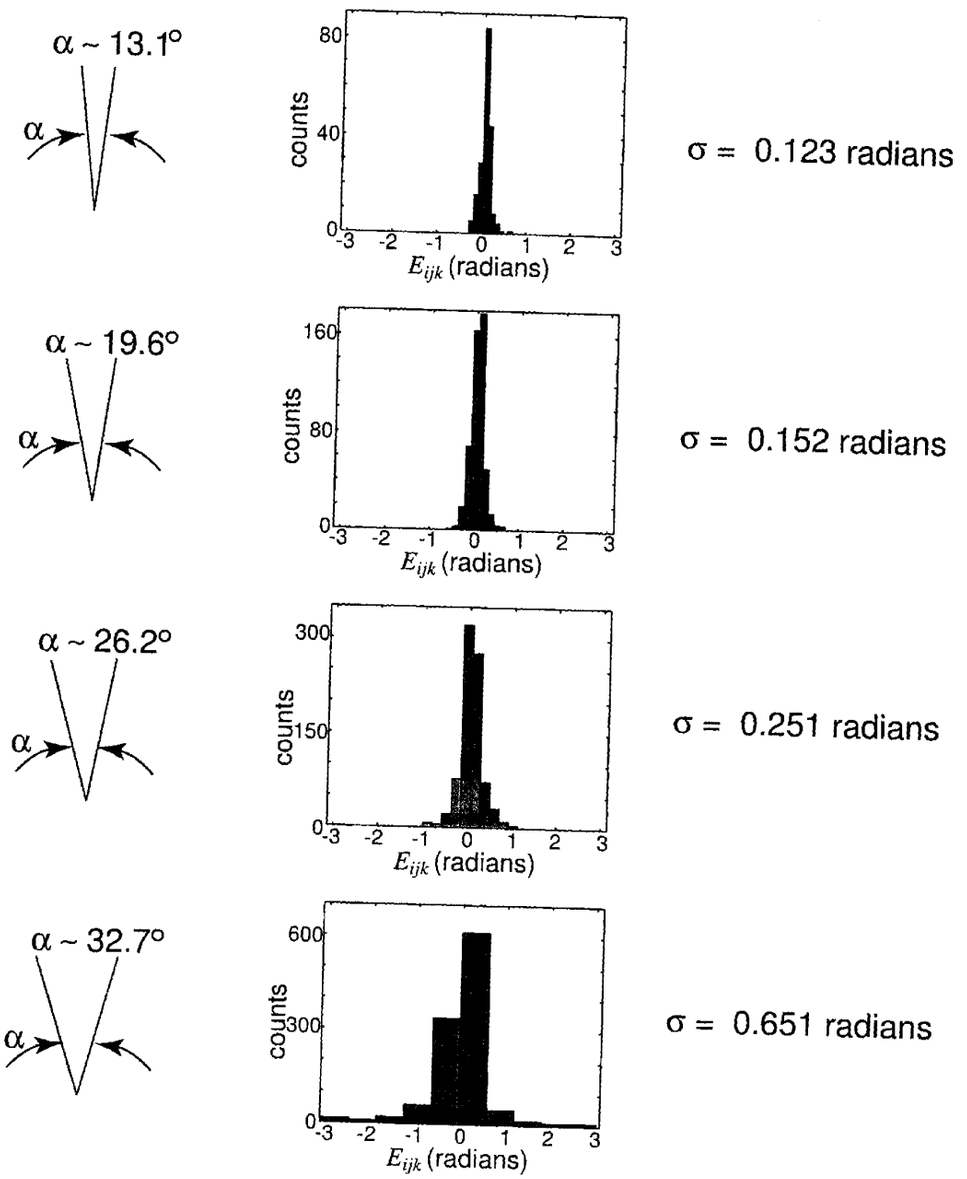

Figure 4-9: Phase estimation accuracy decreases as the angular separation between the two beams (α) increases. The left part shows the angular separations between the two outer beams for four groups of beam triplets. The right part shows the histogram of E_{ijk} and its standard deviation for each beam triplet group.

where λ is the wavelength of light, θ is the half cone angle of the beams, and α is the angular separation between the two beams. As the feature size (L) becomes smaller, the measurement noise such as table vibration becomes comparable to it, which is a likely reason for the increase in standard deviation with increasing angle α in Figure 4-9.

Verification of a single microsphere

The beam triplet phase consistency check can also be used to check for the presence of a single microsphere within a region of interest. Verifying it based on the image of the calibration target is not always straightforward because of the low resolution of the imager and the nonuniform illumination intensity across the field of view. Suppose a region contains a cluster of several microspheres (for example, two microspheres that are adjacent to each other), rather than a single, isolated microsphere. In this case, the spatial frequencies making up the cluster are no longer in phase as in the case of a single microsphere. As a result, the term $\angle\mathcal{S}(\mathbf{k}_{ij})$ in Eq. (4.12) takes a non-zero value that is dependent on $\mathbf{k}_{ij}$, and χ_{ij} no longer becomes an estimate of ϕ_{ij}.

The bottom panel in Figure 4-8 (b) shows the same plot of $\chi_{ij} + \chi_{jk}$ vs. χ_{ik} constructed using data from a target in sub-region B in (a). Deciding whether or not the region B contains a single microsphere just from visual inspection of the image is ambiguous. On the other hand, the triplet phase consistency check result in part (b) clearly shows deviation from what is expected for a single microsphere. Therefore, the beam triplet phase consistency check described here can be a convenient way to verify the presence of a single microsphere within a region of interest.

It should be emphasized that the data from a single microsphere are sufficient to estimate the amplitudes and the phases of fringes. As will be shown in the following section, data from multiple microspheres are necessary to estimate the fringe frequencies.

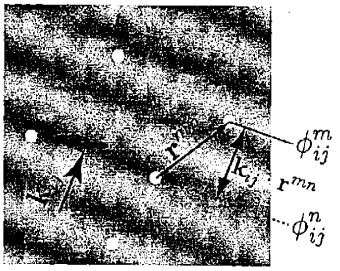

Figure 4-10: Relationship between the spatial frequency of the fringe ($\mathbf{k}_{ij}$), phases estimated from two microspheres (ϕ_{ij}^m and ϕ_{ij}^n), and the locations of the beads ($\mathbf{r}^m$ and $\mathbf{r}^n$). $\mathbf{r}^{mn} = \mathbf{r}^m - \mathbf{r}^n$.

4.4 Analysis and results: Fringe frequencies

This section describes algorithms to estimate the fringe frequencies using data from multiple microspheres. A basic idea here is that the phase estimates at multiple locations of a fringe pattern contain information about its frequency. Each microsphere produces an estimate of a fringe phase referenced to the center position of the microsphere.

Here, we use the relationship between the fringe phases estimated from a selected set of microspheres, the locations of the microspheres, and the fringe frequencies. Figure 4-10 illustrates this relationship with five microspheres illuminated by a fringe pattern with frequency $\mathbf{k}_{ij}$. For a pair of microspheres s^m and s^n, their locations are given by vectors $\mathbf{r}^m$ and $\mathbf{r}^n$. The vector $\mathbf{r}^{mn}$ corresponds to the difference between the two location vectors ($\mathbf{r}^m - \mathbf{r}^n$). The fringe phases estimated using data from each of the two microspheres are ϕ_{ij}^m and ϕ_{ij}^n, respectively. The following equality should hold:

$$M(\mathbf{k}_{ij} \cdot \mathbf{r}^{mn}) = \phi_{ij}^{mn} \tag{4.19}$$

where $M(x)$ is the remainder of x after division by 2π, and $\phi_{ij}^{mn} = \phi_{ij}^m - \phi_{ij}^n$. $\mathbf{k}_{ij} \cdot \mathbf{r}^{mn}$, in units of radians, is also indicated in the figure.

Suppose the two vectors $\mathbf{k}_{ij}$ and $\mathbf{r}^{mn}$ are known only to a crude approximation while the fringe phase ϕ_{ij}^{mn} is assumed to be precisely known. In such a case, one can

define the following error representing the inaccuracy in $\mathbf{k}_{ij}$ and $\mathbf{r}^{mn}$:

$$E_{ij}^{mn} = M(\mathbf{k}_{ij} \cdot \mathbf{r}^{mn}) - \phi_{ij}^{mn}. \tag{4.20}$$

One can then search for values of $\mathbf{k}_{ij}$ and $\mathbf{r}^{mn}$ that minimize the above error. Obviously the problem cannot have a unique solution because there is only a single equation for two unknowns. However, when sufficiently many fringes and microspheres are considered simultaneously, the problem of finding a set of $\mathbf{k}_{ij}$'s and a set of $\mathbf{r}^{m}$'s that best-fit the phase estimates can be over-determined.

The search procedure is divided into the following steps:

- step 1: Determine initial guesses for $\mathbf{k}_{ij}$'s and $\mathbf{r}^{m}$'s.
- step 2: Refine each $\mathbf{k}_{ij}$ while fixing the $\mathbf{r}^{m}$'s and ϕ_{ij}'s so that the root-mean-square (RMS) value of E_{ij}^{mn} defined above for *all possible pairs of microspheres* can be minimized. Repeat this for every $\mathbf{k}_{ij}$.
- step 3: Refine each $\mathbf{r}^{m}$ while fixing $\mathbf{k}_{ij}$'s and ϕ_{ij}'s so that the RMS error for *all possible pairs of beams and the remaining microspheres* can be minimized. Repeat this for every $\mathbf{r}^{m}$.
- step 4: Repeat the previous two steps until the error converges to a minimum.

The initial values of the $\mathbf{r}^{m}$'s for the above iterative procedure were obtained from a composite image of the calibration target. When many low resolution images of the calibration target illuminated by a series of fringes are averaged, the composite image is what we would expect if the target were illuminated uniformly. Figure 4-11 shows a sub-region of the averaged image, containing a single microsphere. The center position of the microsphere can be estimated by calculating the centroid value of participating pixels as defined by:

$$x_C = \frac{\sum_i p_i x_i}{\sum_i p_i} \tag{4.21}$$

$$y_C = \frac{\sum_i p_i y_i}{\sum_i p_i} \tag{4.22}$$

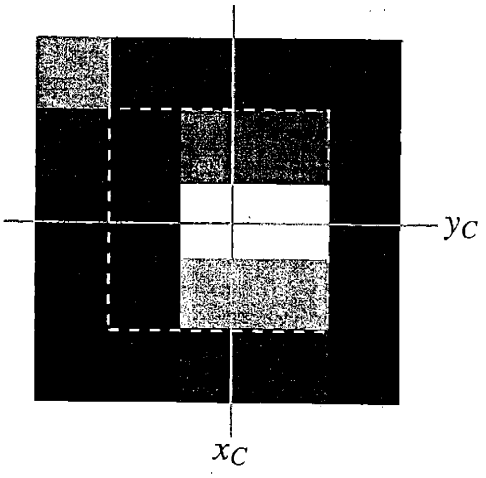

Figure 4-11: An averaged image of a single microsphere. Nine pixels bounded by the dotted box were used in calculating the centroid position (x_C, y_C) of the microsphere.

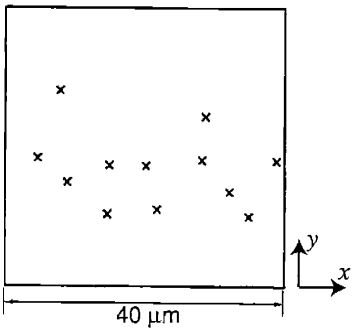

Figure 4-12: Locations of 12 microspheres used in calibration, estimated by the centroid method. These were used as the initial estimates of the $\mathbf{r}^m$'s.

where x_C and y_C are the x and y component of the centroid point and p_i, x_i, and y_i are the pixel value, x position, and y position of the i-th pixel. Figure 4-12 shows estimated centroid locations of 12 microspheres whose data were used in calibration.

Initial estimates of the $\mathbf{k}_{ij}$'s can be calculated using the wavelength of light, polarization of the source beam, half cone angle of the cone of beams, and positions of the ring mirrors (Figure 3-8) producing it, without any separate measurement step.

An iterative procedure that performs the optimizations for step 2 and 3 was implemented based on the Nelder-Mead simplex algorithm (Nelder and Mead, 1965; Press et al., 1988), a well-known direct search method[‡] for multi-dimensional unconstrained

[‡]meaning that it attempts to minimize a scalar-valued nonlinear function of n real variables using only function values, without any derivative information

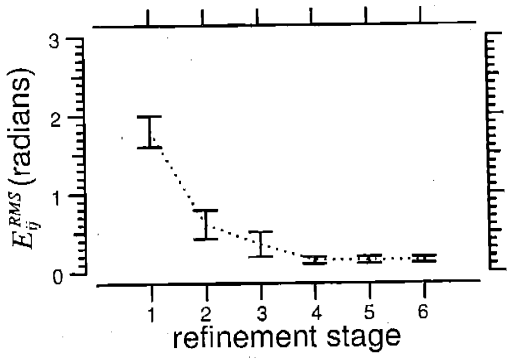

Figure 4-13: The reduction of error by the optimization procedure described in the text. For each stage of optimization, ± 1 standard deviation range of the RMS error, E_{ij}^{RMS}, for all $\mathbf{k}_{ij}$'s is illustrated. The dotted line connects the mean values.

minimization.

Convergence of the optimization procedure is shown in Figure 4-13. For each $\mathbf{k}_{ij}$, the RMS value of E_{ij}^{mn} over all possible pairs of microspheres was calculated, at each stage of optimization. The plot shows ± 1 standard deviation range of the RMS error, E_{ij}^{RMS}, for 62 $\mathbf{k}_{ij}$'s. Stage 1 corresponds to the initial values of the refinement variables, $\mathbf{k}_{ij}$'s and $\mathbf{r}^m$'s. Stage 2 and 3 correspond to results after the optimization step 2 and 3. Stage 4 and 5 correspond to results after the answers from the stage 3 were used as inputs for the second iteration of optimization step 2 and 3, etc. The plot shows an order of magnitude decrease and convergence of the error after six stages of the optimization, demonstrating its performance. The locations of 125 frequencies in Fourier space estimated for 62 beam pairs are shown in Figure 4-14.[§]

[§]Notice that the current 31 beam projector can project 465 distinct fringe patterns, represented by 931 distinct frequencies in Fourier domain. The frequencies shown in Figure 4-14 correspond to a low frequency subset of the entire set of frequencies. Calibration of fringes with higher frequencies was limited by the inaccuracy in phase estimates illustrated in Figure 4-9.

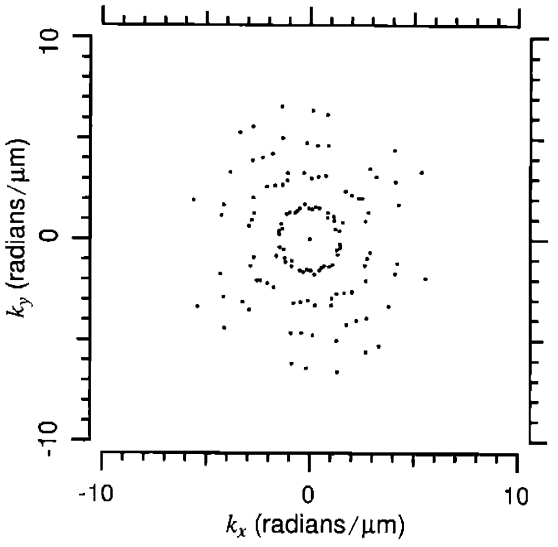

Figure 4-14: Estimated locations of 125 frequencies of 62 fringes in Fourier space.

Chapter 5

Imaging Using a Single Light Sensor

5.1 Introduction

In conventional optical microscopy using a CCD, target information is spatially sampled by the pixels of the CCD, producing an array of gray values that make up an image of the target. An output recording from a single light sensor is a single gray value, which does not constitute an image. Imaging using a single light sensor becomes possible if either the target or the light sensor is translated, producing a gray value at each translated location. Laser scanning confocal microscopy (J. B. Pawley, 1995) is a representative example of such a scanning system. Typically, a single photon counter such as a photomultiplier tube (PMT) or an avalanche photodiode (APD) is used on the detection side for maximum light sensitivity.

The advantages of PMTs or APDs over CCDs are speed (over 100 MHz bandwidth) and sensitivity (capable of detecting a single photon). However the speed cannot be fully exploited in conventional scanning systems due to the mechanical limits of scanning. Typically, the scanning actuator is a piezoelectric transducer (PZT). The smallest interval between two successive actuations using a PZT is typically more than two orders of magnitudes longer than the interval between two successive photon counting events using a PMT or an APD, and this becomes the limiting factor in

data acquisition speed. The nonlinearity of PZT response is an additional limitation. It would be desirable to replace the mechanical scanning operation by an alternative mechanism with speed comparable to that of a PMT or APD.

Here, a proof-of-concept demonstration of an imaging system using a single light sensor without any intentional mechanical motion of its parts is described. A sequence of brightnesses of a cluster of several microspheres, which can be measured using a single light sensor, was recorded when the target was illuminated by a sequence of structured light patterns. All components of the system: the apparatus delivering the sequence of illuminations, the target and the stage, and the detectors, were fixed in space with no need for mechanical actuation. Computer-processing the brightness sequence, using knowledge of the illumination sequence, permitted reconstruction of an image of the target that revealed individual microspheres in the constellation.

5.2 Experiment

5.2.1 Imaging setup

For the imaging experiment, the multiple-beam interference pattern projector described in Chapter 3 (Figure 3-8 and Figure 3-9) was combined with a conventional optical microscope (Figure 5-1). The projector, for which the aluminum plate and the mirror assembly beneath it are shown in Figure 5-1 (a), produces a cone of 31 laser beams which overlap and produce an interference pattern illuminating a target on the stage. The half cone angle of the cone of beams (the angle θ_1 in Figure 5-1) is 78°, resulting in a numerical aperture (NA) of 0.98. Fluoresced light from the target passes through a microscope objective and a λ filter and hits the CCD. The NA of the microscope objective is 0.2, corresponding to a half cone angle (the angle θ_2) of 11.5°. The same objective, λ filter, and CCD as described in Chapter 4 for calibration data acquisition were used in the imaging setup shown in the figure.

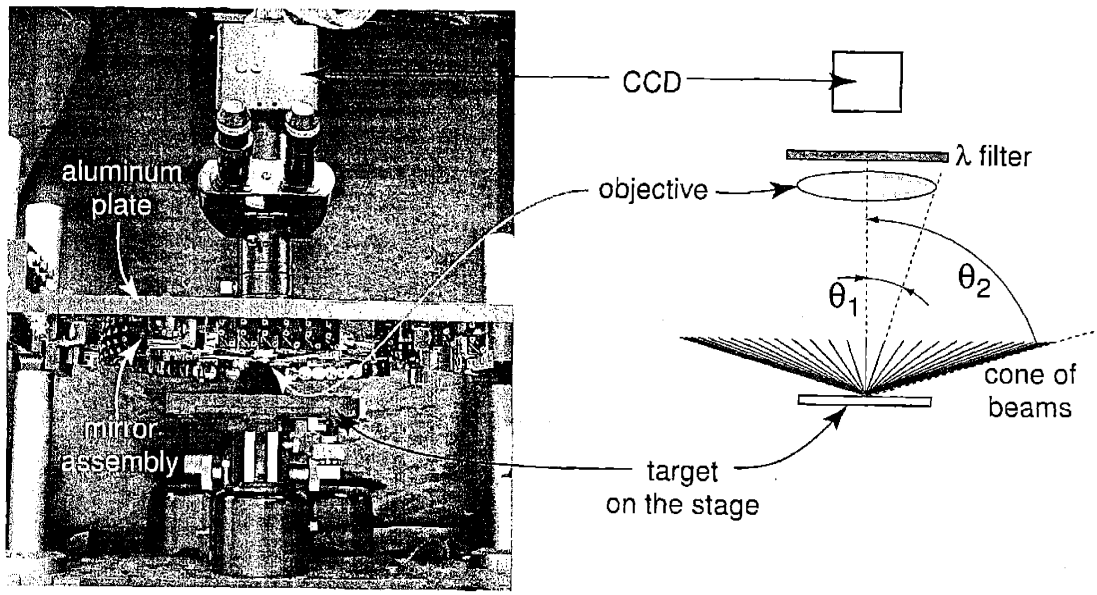

(a)

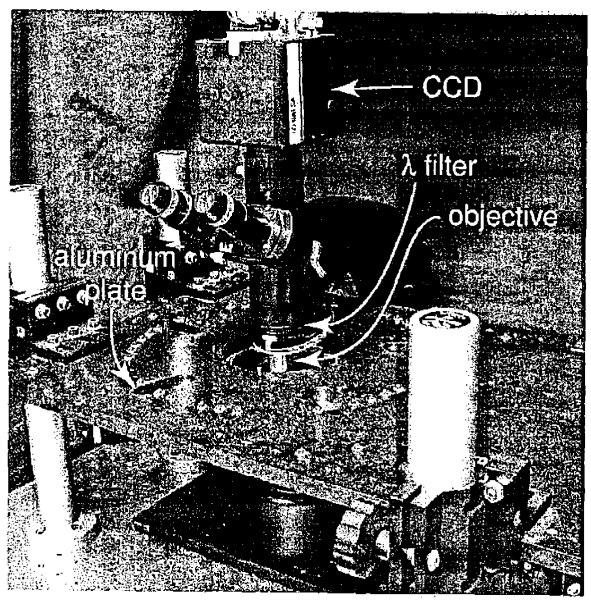

(b)

Figure 5-1: (a) Photograph of the imaging setup (left) and its schematic diagram (right). A more detailed view of the mirror assembly under the aluminum plate is shown in Figure 3-8. (b) View of the setup in (a) from a different angle.

5.2.2 Test target

To demonstrate the structured illumination approach, a random monolayer of 1 μm diameter fluorescent microspheres (model T-8880, Molecular Probes, Inc., Eugene, Oregon, 1.0 μm diameter, 30 nm standard deviation in diameter) was fabricated using a procedure described in Chapter 4. Figure 5-2 (a) shows an image of the target containing many microspheres illuminated by a fringe pattern. For the remainder of this chapter, we consider only the brightness of an unknown target contained in the dotted box in the image. A zoomed-in view of this sub-region is shown in Figure 5-2 (b). It is suspected that this region contains a cluster of several microspheres. However, individual microspheres in the cluster are not resolved. This is because of the limited resolution due to the NA of the microscope objective (0.2) and the finite pixel size (1 μm*)

Figure 5-2 (c) is an image of the same region as part (b), acquired using a 0.6 NA microscope objective.† A constellation of three microspheres is resolved in the image. Our goal here is to reconstruct an image of the target that resolves the individual microspheres, using a sequence of brightnesses of the target during a series of structured illuminations. Brightness of the target is measured here by summing the 16 pixel values within the dotted box in Figure 5-2 (b), but the same measurement could be done using a *single* light sensor. Therefore, the results shown in this chapter could be obtained using a single light sensor that is faster and more sensitive than a CCD, such as a PMT or APD, set up to count the photons fluoresced from the region of interest on the target.

5.2.3 Data acquisition

The target was illuminated by a sequence of light patterns. For each illumination pattern, an image of the target was acquired, with 40 msec exposure time. The sequence of illuminations was produced in the same way as described for the calibration

*This is the effective pixel size in the target space, calculated by dividing the actual pixel size (10 μm) by the magnification of the imaging system (10x).

†Zeiss Axioplan microscope with Koehler illumination was used here.

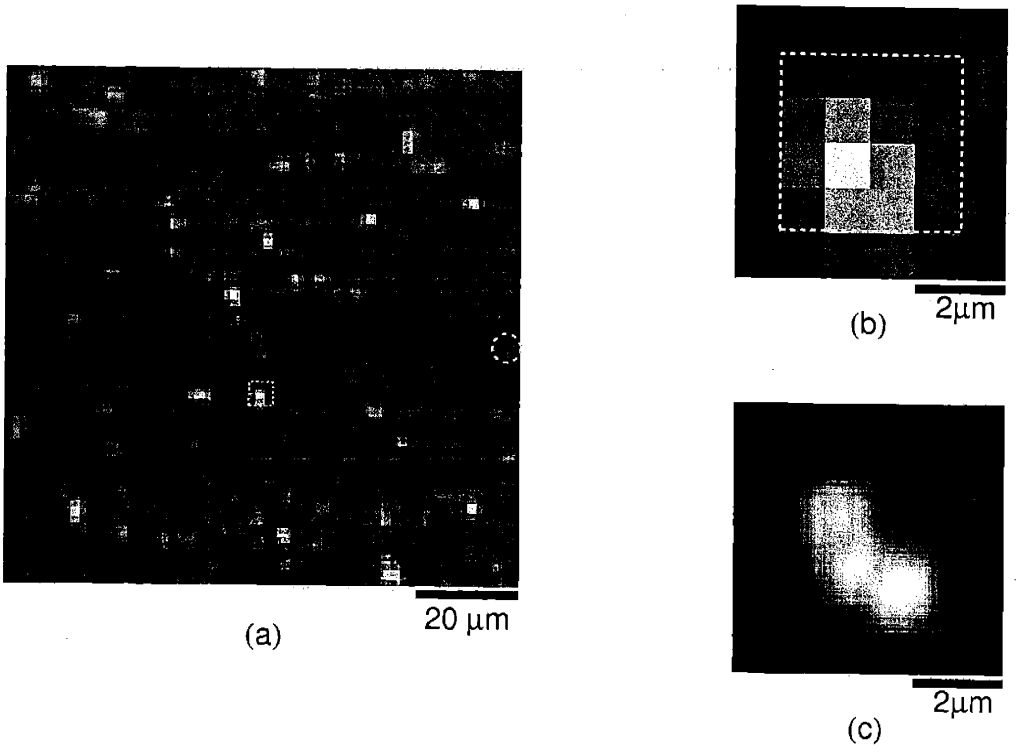

Figure 5-2: (a) A test target made of fluorescent microspheres with 1 μm diameter. The dotted box contains a target of interest. The dotted circle contains a single microsphere used in calibration. (b) A zoom-in view of the dotted box in (a). Brightness of the target is measured by summing the 16 pixel values within the dotted box. (c) An image of the unknown target in (b) acquired using 0.6 NA objective under uniform illumination. Three microspheres are resolved.

data acquisition. Each illumination pattern was a fringe pattern made by interfering a pair of beams. For each pair of beams (i and j), the electrical phase of the AOD drive for beam j (η_j defined in Figure 4-3) was changed from 0 to 2π at 16 equally spaced phases, while the electrical phase for beam i was fixed. This procedure was repeated for 82 different pairs of beams, producing a total of $16 \times 82 = 1312$ images.[‡]

Amplitudes, phases, and frequencies of fringes defined in Eq. (4.2) need to be known in post-processing the data to reconstruct an image of the target. In Chapter 4, it was shown that the sequence of brightnesses of a single microsphere is sufficient to calibrate the amplitudes and the phases of the fringe patterns used as the illumination. Also, data from multiple microspheres are required to calibrate the spatial

[‡]Total data acquisition time in this case is therefore 40 msec $\times$ 1312 = 53 sec.

frequencies contained in the sequence of illuminations. A calibration target containing multiple microspheres was fabricated separately for this purpose and the fringe frequency calibration data were acquired immediately before the acquisition of imaging data.[§] Then, a single microsphere in the region marked by a circle in Figure 5-2 (a) was used as the amplitude and phase calibration target. Thus, the amplitude and phase calibration data were acquired simultaneously with the imaging data.

5.3 Post-processing the data

5.3.1 Estimation of Fourier transform coefficients

The first step in post-processing of the data is to determine a set of Fourier transform coefficients of the target from a sequence of measured brightnesses. Figure 5-3 shows a sinusoidal change in the measured brightness of the target in Figure 5-2 (b) when the target was illuminated by a sequence of fringe patterns differing in phase (see Figure 4-3). For a pair of interfering beams (i and j), the electrical phase for beam j, η_j, was changed from 0 to 2π at 16 equally spaced phases with η_i fixed at 0. In the plot, circles are measured brightnesses and the curve is the least-square fit of the measurements to a raised cosine function. The three parameters (p_{ij}^0, p_{ij}^1, and χ_{ij}) of the best-fit sinusoidal function are also indicated in the plot.

As described in Chapter 4, the brightness data are the samples of the convolution of the target contrast pattern, represented by $g(\mathbf{r})$, and the fringe pattern, $f_{ij}(\mathbf{r})$. In Chapter 4, the measured brightnesses were used to estimate the Fourier transform coefficients of the fringe pattern with a known target, a single microsphere. Now, the Fourier transform coefficients of the target are estimated from the brightness data using a fringe that is known as a result of calibration. One can re-write Eq.s (4.10, 4.11, 4.12) while replacing the Fourier transform of the microsphere $\mathbf{S}(\mathbf{k})$ with the

[§]The fringe amplitude and phase can shift with tiny perturbations of the setup, e.g., temperature variations, drifts, but the spatial frequencies are more stable.

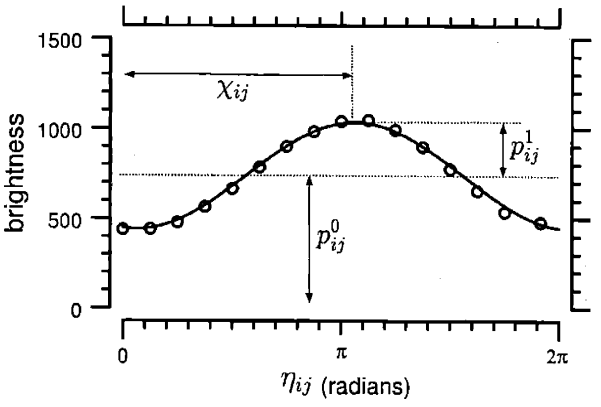

Figure 5-3: Brightness of the target vs. electrical phase difference between a pair of beams, η_{ij}. Circles are the measured brightnesses and the curve is the least square fit of the data points to a raised cosine function. The three parameters of the best-fit function are indicated.

Fourier transform of the unknown target $\mathbf{G}(\mathbf{k})$:

$$c^0_{ij} = \frac{p^0_{ij}}{|\mathbf{G}(0)|} \tag{5.1}$$

$$c^1_{ij} = \frac{p^1_{ij}}{|\mathbf{G}(\mathbf{k}_{ij})|} \tag{5.2}$$

$$\phi_{ij} = \chi_{ij} - \angle\mathbf{G}(\mathbf{k}_{ij}). \tag{5.3}$$

Now c^0_{ij}, c^1_{ij}, ϕ_{ij}, and $\mathbf{k}_{ij}$ are the *known* parameters of the fringe function $f_{ij}(\mathbf{r})$ defined in Eq. (4.2), and p^0_{ij}, p^1_{ij}, and χ_{ij} are obtained from the measured brightness values shown in Figure 5-3. Re-writing the above equations results in the following expressions for $\mathbf{G}(0)$ and $\mathbf{G}(\mathbf{k}_{ij})$, Fourier transform coefficients of $g(\mathbf{r})$ at DC and at $\mathbf{k}_{ij}$:

$$\mathbf{G}(0) = \frac{p^0_{ij}}{c^0_{ij}} \tag{5.4}$$

$$\mathbf{G}(\mathbf{k}_{ij}) = \frac{p^1_{ij}}{c^1_{ij}} e^{j(\chi_{ij}-\phi_{ij})}. \tag{5.5}$$

The phase of a fringe pattern is determined with respect to a reference point in space, which can be chosen arbitrarily. Suppose, in the example of Figure 5-2 (b),

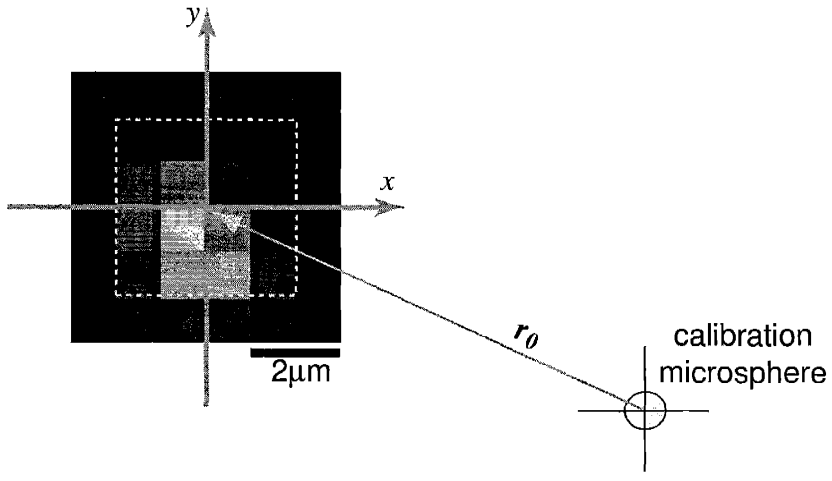

Figure 5-4: Extrapolation of the fringe phase. The phase is determined using the center of the reconstruction region as the reference point (the origin of the x-y coordinate). Phase of a fringe pattern estimated from the calibration microsphere shown in the figure is referenced to the center of the microsphere and needs to be extrapolated to the origin of the x-y coordinate. The vector $\mathbf{r}_0$ starts at the center of the microsphere and ends at the origin.

the center of the dotted rectangle is chosen as the reference point, which becomes the origin of the reconstruction coordinate (x-y coordinate shown in Figure 5-4). However, the phase of the fringe is estimated with respect to the center of the microsphere. The fringe phase with respect to the origin of the reconstruction coordinate, ϕ_{ij}, can be obtained from ϕ'_{ij}, the calibrated phase, in the following way:

$$\phi_{ij} = \phi'_{ij} + \mathbf{k}_{ij} \cdot \mathbf{r}_0 \tag{5.6}$$

where $\mathbf{k}_{ij}$ is the spatial frequency of the fringe pattern and $\mathbf{r}_0$ is a vector from the center of the microsphere to the origin of the reconstruction coordinate.

Fourier transform coefficients of the unknown target were estimated by the above method at spatial frequencies contained in the sequence of illuminations (Figure 4-14), which were produced by the interference of 62 different pairs of beams. The results are displayed in Figure 5-5.

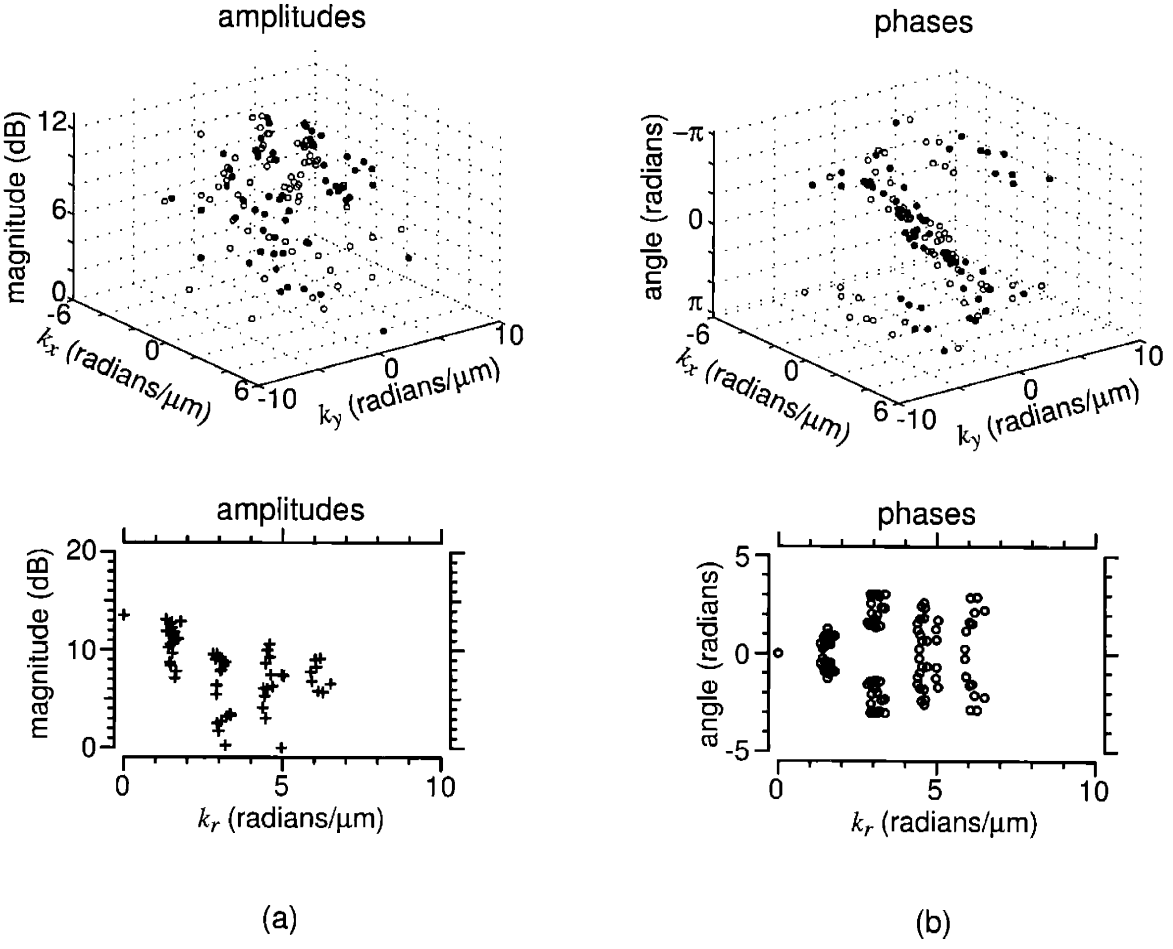

Figure 5-5: A total of 125 estimated Fourier transform coefficients of the unknown target in Figure 5-2 (b). (a) Fourier transform amplitudes. Filled data points and unfilled ones in the top plot are for conjugate spatial frequencies of each other. The plot at the bottom shows the same data as a function of the radial spatial frequencies ($k_r = \sqrt{k_x^2 + k_y^2}$). (b) Fourier transform phases. The transform coefficients in (a) and (b) were determined at spatial frequencies contained in the sequence of illuminations, shown in Figure 4-14.

5.3.2 Image reconstruction

The distribution of frequencies at which the target's Fourier transform is sampled in Fourier space is highly nonuniform (Figure 5-5 (c)); it is roughly a set of concentric circles. The Fourier space is densely populated along the angular directions but sparsely populated along the radial directions. This nonuniformity is a source of artifacts in an image reconstructed from the measured set of transform coefficients. A simple method, based on the Voronoi diagram, to address this non-uniform distri-

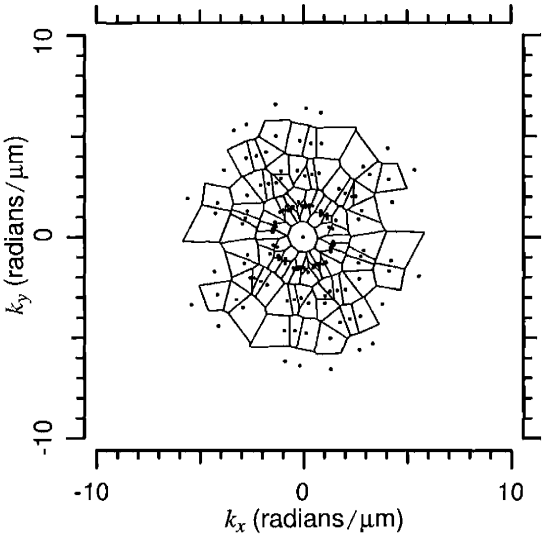

Figure 5-6: Voronoi diagram, a set of Voronoi polygons for the spatial frequencies shown in Figure 5-5 (c). The area of the Voronoi polygon for each frequency becomes a weighting factor for that frequency component when reconstructing an image of the target. Notice that Voronoi polygons for some frequencies in the outermost region cannot be defined. For these frequencies, the weighting factor w_{ij}'s were set to be the average area for all Voronoi polygons.

bution problem was described in Chapter 2. Voronoi polygons were calculated for the frequencies in Figure 5-5 (c) and the resulting Voronoi diagram is shown in Figure 5-6.

An image of the target $g(\mathbf{r})$ was then reconstructed using the following reconstruction formula (Eq. (2.13)):

$$s(\mathbf{r}) = w_0\mathbf{G}(0) + \sum_{all\ (i,j)} w_{ij}\mathbf{G}(\mathbf{k}_{ij})e^{j\mathbf{k}_{ij}\cdot\mathbf{r}} + \sum_{all\ (i,j)} w_{ij}\mathbf{G}^*(\mathbf{k}_{ij})e^{-j\mathbf{k}_{ij}\cdot\mathbf{r}} \qquad (5.7)$$

where w_0 and w_{ij} are the areas of the Voronoi polygons for DC and the spatial frequency $\mathbf{k}_{ij}$, and $\mathbf{G}(\mathbf{k}_{ij})$ and $\mathbf{G}^*(\mathbf{k}_{ij})$ are the Fourier transform coefficients estimated at $\mathbf{k}_{ij}$ and its complex conjugate.

A computer simulation shows the effectiveness of the Voronoi method in addressing the non-uniform sampling problem. A computer simulated image of a cluster of three 1 μm diameter microspheres in a 4 μm $\times$ 4 μm region was generated. A model of the microsphere's optical response shown in Eq. (4.13) was used. Positions of individual

microspheres were selected based on the high resolution image of the experimental target shown in Figure 5-2 (c), with a constraint that adjacent microspheres are touching each other.

A set of Fourier transform coefficients of the simulated target was calculated at the spatial frequencies shown in Figure 5-6. An image of the target was reconstructed from these coefficients using the reconstruction formula in Eq. (5.7). Figure 5-7 shows the results. In part (a), no weighting was introduced in the reconstruction formula, that is, the w's in Eq. (5.7) are all equal to one. The Voronoi polygon weighting scheme was used for part (b). Improved visual resolution of the image is a clear benefit of the Voronoi weighting method.

However, the image in part (b) shows increased background artifacts compared to part (a), suggesting a trade-off in the use of the Voronoi weighting reconstruction method. Sub-optimality is seen in the Voronoi diagram in Figure 5-6. Most of the Voronoi polygons are radially elongated, meaning that the sampled frequency within a Voronoi polygon represents frequencies that are far apart from each other.

5.4 Results

Comparing with the computer simulation

Figure 5-8 shows the counterpart images of the computer-simulated images in Figure 5-7, reconstructed from experimental data. As predicted by the computer simulation, the Voronoi weighting method shows a significant improvement in resolving individual microspheres. This is also shown in the intensity scans across a pair of microspheres at the bottom of the images (continuous lines). Again, the background artifact increased with the Voronoi weighting method, as predicted by the computer simulation. Notice the similarity of background artifacts to those appearing in the computer simulation (Figure 5-7 (b)).

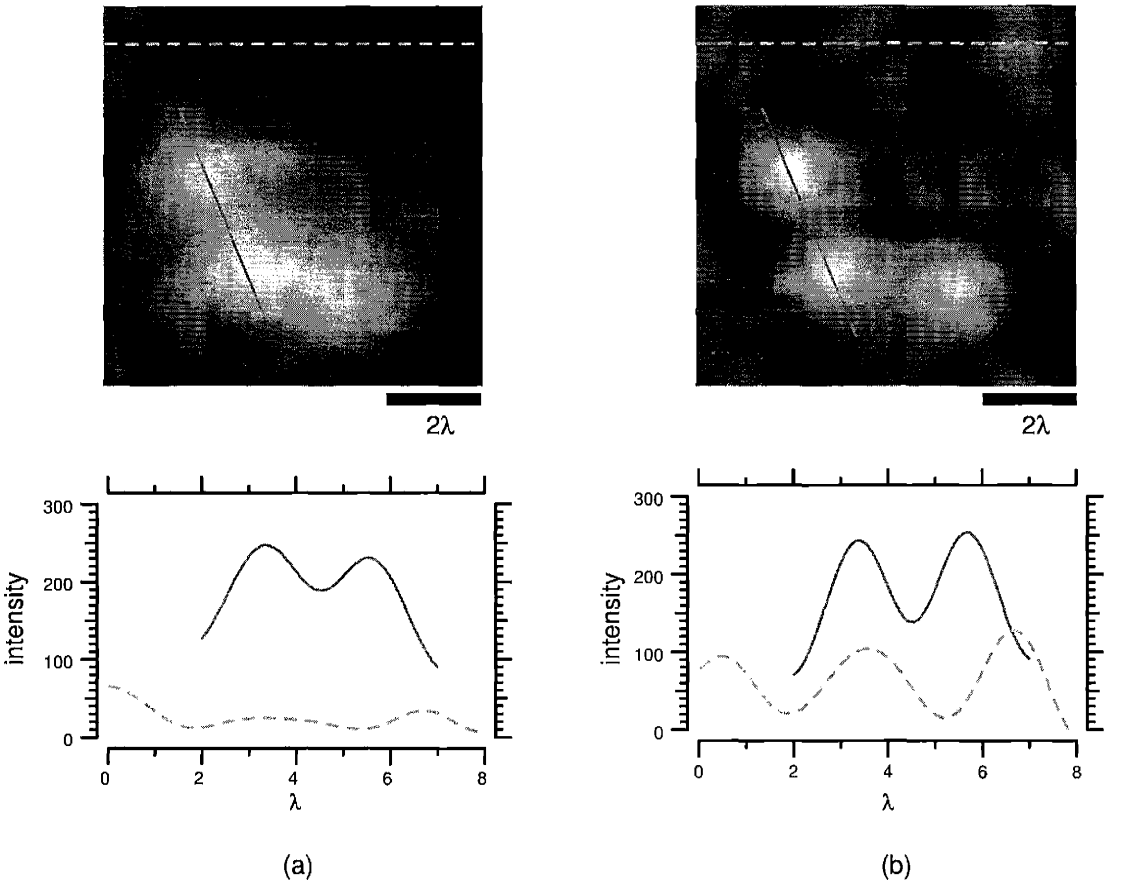

Figure 5-7: Computer simulated images of a cluster of three 1 μm diameter microspheres for the sequence of illuminations containing spatial frequencies shown in Figure 5-6. (a) Reconstruction without the Voronoi weighting of Fourier transform coefficients. (b) Reconstruction using Voronoi weighting method. The plots at the bottom of the images show intensities across the two adjacent microspheres (continuous lines) and in the background region (dotted lines). $\lambda = 488$ nm.

Comparing with the conventional microscopy

Figure 5-9 shows images of the same target acquired with three different imaging conditions. The image in panel A was acquired using conventional microscopy under uniform illumination with 0.2 NA objective.[¶] The image in panel B is the structured illumination image of Figure 5-8 (b). The same microscope objective was used in panel A and B.

The image in panel B demonstrates that a sequence of brightness measurements

[¶]Zeiss axioplan microscope with Koehler illumination was used.

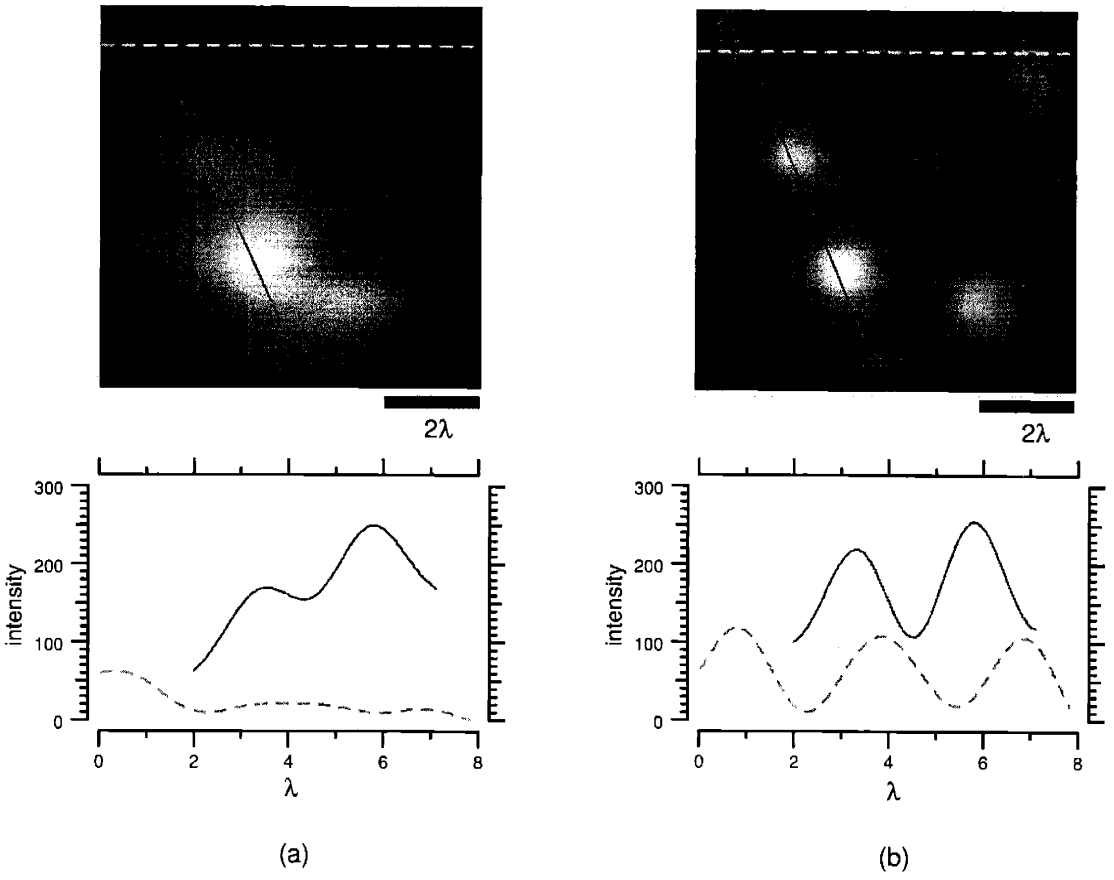

Figure 5-8: Images of the unknown target in Figure 5-2 (b) reconstructed using a sequence of brightnesses of the target. (a) Reconstruction without the Voronoi weighting of Fourier transform coefficients. (b) Reconstruction with the Voronoi weighting. $\lambda = 488$ nm. The plots at the bottom of the images show intensities along the lines indicated in the image.

without any mechanical scanning can produce an image of the target. Effectively, mechanical scanning is replaced by the phase modulation of beam pairs, which does not involve any mechanical motion. In this experiment, the speed of data acquisition was limited by the CCD. However, if a high speed light sensor such as a PMT or APD were used to record the brightness of the target, more than several orders of magnitude increase in imaging speed would be expected, compared with a mechanical scanning system using the same light sensor.

Comparing the two images in panel A and B also experimentally demonstrates an improvement in resolution using the structured illumination technique. A constellation of three microspheres is clearly resolved in panel B, but not in panel A, yet both

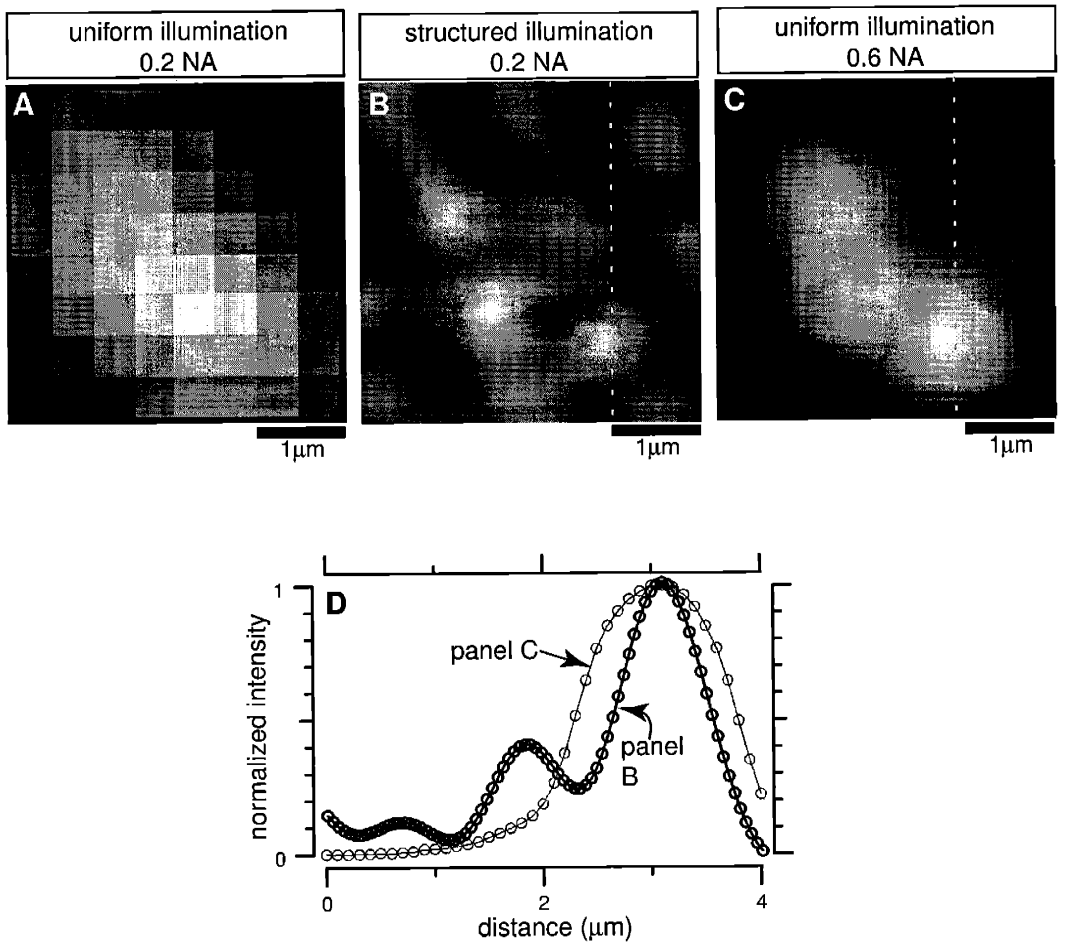

Figure 5-9: Image of the same target acquired using three different techniques. (a) Conventional microscopy under uniform illumination, using 0.2 NA objective. Individual microspheres are not resolved. (b) Structured illumination technique using the same objective. Individual microspheres are clearly resolved, demonstrating the resolution improvement using structured illumination technique. (c) The target was verified by imaging it with 0.6 NA objective, under uniform illumination. Notice that the image in part (b) is sharper than part (c), although the NA of the objective is three times lower. This is shown quantitatively in the intensity plot in part (d). The plot shows intensities along the dotted lines from the two images. In acquiring the images in part (a) and (c), the Zeiss axioplan microscope with Koehler illumination was used.

were acquired at the same working distance of the 0.2 NA objective.

The target was also imaged using an objective with 0.6 NA under uniform illumination. The resulting image is shown in panel C. The images in panels B and C resolve individual microspheres that are not resolved in panel A. However, an important point here is that the resolution of the image in panel C depends primarily on

the microscope objective's performance, which cannot be scaled to short wavelengths of light such as ultraviolet and x-ray. On the other hand, the resolution of the image in panel B depends on the structured illumination produced by an apparatus made of mirrors (reflective optical elements) only, with the exception of the AOD (a refractive element). Therefore, the imaging technique in panel B could be scaled to short wavelengths of light if the AOD were replaced by a reflective light modulator.[‖]

Notice that the image in panel B is sharper than the image in panel C, which is also shown quantitatively in the intensity plot in panel D. This can be predicted from the point spread function (PSF) analysis of the two imaging techniques. The PSF for an imaging system is the spatial mapping of intensity when the system images an infinitesimally small target, and is a measure of the resolution of the imaging system. The simulated PSF's of the imaging techniques of panels B and C are compared in Figure 5-10. Part (a) is the PSF of the structured illumination technique with spatial frequencies contained in the illumination shown in Figure 5-6. Part (b) is the PSF of a microscope objective with 0.6 NA for 560 nm light, the peak emission wavelength of the fluorescent dye coating the microspheres. Intensity scans through the centers of the two images are compared at the bottom of the images. The width of the PSF of the structured illumination technique is narrower than the uniform illumination method that uses an objective with three time higher NA.

Spatial extent of Fourier space sampling

In the structured illumination approach, a sequence of brightnesses of a target reported from a single light sensor encodes contrast information about the target sampled in Fourier space. This suggests that the spatial extent of the reconstructed image is not directly related to the area of the light sensor in the target space. In fact, in Chapter 2, it was shown that the spatial extent is defined by a window function, which is the convolution of the point spread function (PSF) of the objective and the

[‖]A reflective light modulation technique based on the principle of surface acoustic waves (Ippen, 1967; White and Voltmer, 1965) has been studied extensively, including a recent implementation in our group (Hong, 2001).

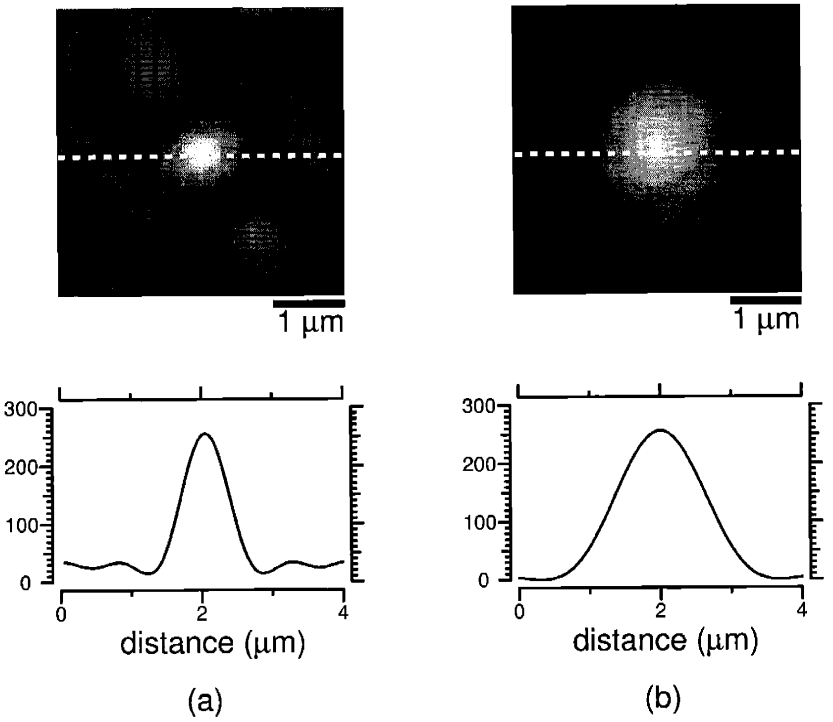

Figure 5-10: Computer-simulated point spread function (PSF) of the structured illumination technique using 0.2 NA objective (a) and uniform illumination imaging using a 0.6 NA objective (b). The PSF in (a) was calculated for the sequence of illuminations with spatial frequencies shown in Figure 5-6. The PSF in (b) was calculated using 560 nm as the wavelength of light. This is the peak emission wavelength of the fluorescent dye of the microsphere. At the bottom, intensities through the centers of the two images are plotted.

pixel response function.

Figure 5-11 experimentally demonstrates this. The image on the right side was reconstructed using data from a single pixel of the CCD and shows two microspheres in the field of view. The box on the left corresponds to the area of the pixel in the target space. The reconstructed image shows sub-pixel details of the target over an area larger than the area of the pixel.

The distance R shown in Figure 5-11 represents the field of view of the reconstructed image and is controlled by the NA of the objective and the size of the pixel. Therefore, what used to control the resolution in a conventional imaging system, now controls the field of view of a single light sensor based image. To obtain an image covering a larger region of the target, it becomes necessary to combine images from multiple light sensors. This is described in the next chapter.

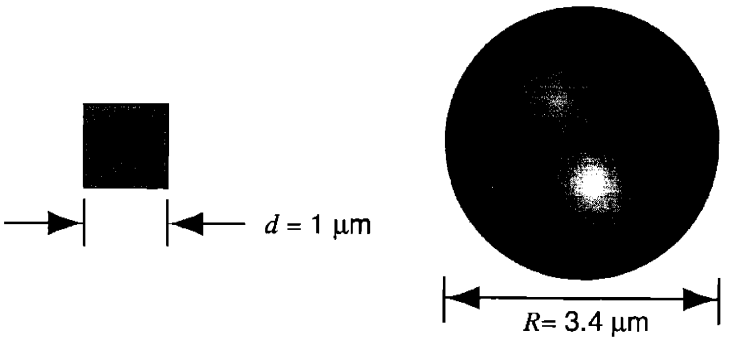

Figure 5-11: Right: An image of two microspheres reconstructed using data from a single pixel of the CCD. The box on the left side represents the area of the pixel in target space. Notice that the reconstructed image shows a region of the target larger than the area of the pixel. The field of view, represented by the distance R, is controlled by the NA (=0.2) of the objective and the size of the pixel.

Chapter 6

Multiple-Beam Interferometric Illumination as the Primary Source of Resolution

6.1 Introduction

The resolution of conventional optical microscopy is often defined in terms of the Rayleigh criterion (Goodman, 1996):

$$\delta = 0.61\frac{\lambda}{NA} \tag{6.1}$$

where λ is the wavelength of the light and NA is the numerical aperture (NA) of the objective. Two incoherent point sources are *barely resolved* by a diffraction limited system with a circular pupil when they are separated by the distance δ.

This means that, at a given wavelength of light, the resolution is primarily determined by the NA of the objective: the higher the NA, the higher the resolution. However, increasing the NA to achieve higher resolution means reducing the working distance (WD), depth of field (DOF), and field of view (FOV), as illustrated in Figure 1-1. This becomes an important trade-off in optical microscopy imaging.

Here, a fluorescence microscopy method is demonstrated in which the linking of

the resolution, WD, DOF, and FOV has been removed. Resolution can be increased without sacrificing the WD, DOF, or FOV. This is accomplished by illuminating the target with interference patterns formed by 31 coherent beams arranged in a cone with 78° half angle (*synthesized* NA = 0.98). In such a system, the NA of the cone of beams, not the NA of the objective, determines the resolution. This fact is experimentally demonstrated here by showing that a significant change in the NA of the objective causes only negligible change in the resolution, as long as the illumination is the same.

Since the resolution is determined by the illumination, a low NA objective can be used, which has longer WD, larger DOF, and larger FOV. Fluoresced light from the target was collected with a 0.1 NA objective for 930 different illumination patterns. Results were used to reconstruct an image with resolution comparable to that of a 0.98 NA objective. Compared to conventional microscopy with 0.98 NA objective, the system has more than an order of magnitude improvement in the WD, DOF, and FOV.

The fact that the multiple-beam interferometric illumination is the primary factor controlling the resolution opens up the possibility of scaling optical microscopy to shorter wavelengths such as ultraviolet light or even X-rays. At these wavelengths, most of the known lens materials become either completely opaque or completely transparent without any refraction, making it impossible to build a lens-based imaging system. On the other hand, a system that produces multiple-beam interferometric illumination can be made using only mirrors (reflective optical elements), which can handle the short wavelengths. The only refractive element in the current system is the acousto-optic deflector (AOD), which serves as the light modulator. Therefore, the imaging technique demonstrated here could be scaled to short wavelengths of light if the AOD were replaced by a reflective light modulator. In fact, a reflective light modulation technique based on the principle of surface acoustic waves (Ippen, 1967; White and Voltmer, 1965) has been studied extensively, including a recent implementation aimed at the interferometric illumination technique (Hong, 2001).

6.2 Effect of NA of the objective on resolution

To assess the effect of the NA of the objective on resolution, two data sets were acquired for the same target using two different NA of the objective. The first data set was acquired with a 0.2 NA objective using a sequence of 930 illumination patterns. The CCD exposure time for each image was 40 msec. The second data set was acquired with a 0.1 NA objective*, using the same sequence of illuminations. The CCD exposure time for each image was 600 msec.

The same data for each NA were processed in two different ways. In the first case, the 930 images were averaged to produce a single image, without utilizing knowledge of the illumination patterns. The averaged image is comparable to an image acquired with uniform illumination as in conventional microscopy, but has a significantly increased signal-to-noise ratio (SNR) compared to a single exposure image due to the averaging. Figure 6-1 (a) and (b) show images of the identical region of the target generated by averaging 930 images for the NA of 0.2 and 0.1, respectively. In these two images, individual microspheres in a cluster of microspheres are not resolved (for example, a cluster inside the box). Also, the decrease in NA caused significantly increased blurring of the image; the full-width-half-maximum (FWHM) of a single microsphere increased from 1.71 μm to 2.97 μm when the NA changed from 0.2 to 0.1 (Figure 6-1 (c)).

In the second case, an image of the target was reconstructed utilizing the knowledge of the illumination patterns, as described in the previous chapter. In this case, data from each pixel of the CCD were processed to reconstruct an image of the target with sub-pixel details and field of view larger than the area of the pixel. An example image reconstructed from a particular pixel is shown in Figure 5-11. Multiple images independently reconstructed from multiple pixels were then combined to produce an image with full field of view, using the stitching method described in Chapter 2 (Figure 2-6). Figure 6-2 shows the result using experimental data. The left side of

*The effective NA of the objective was reduced from 0.2 to 0.1 by constricting the diameter of the entrance pupil of the objective.

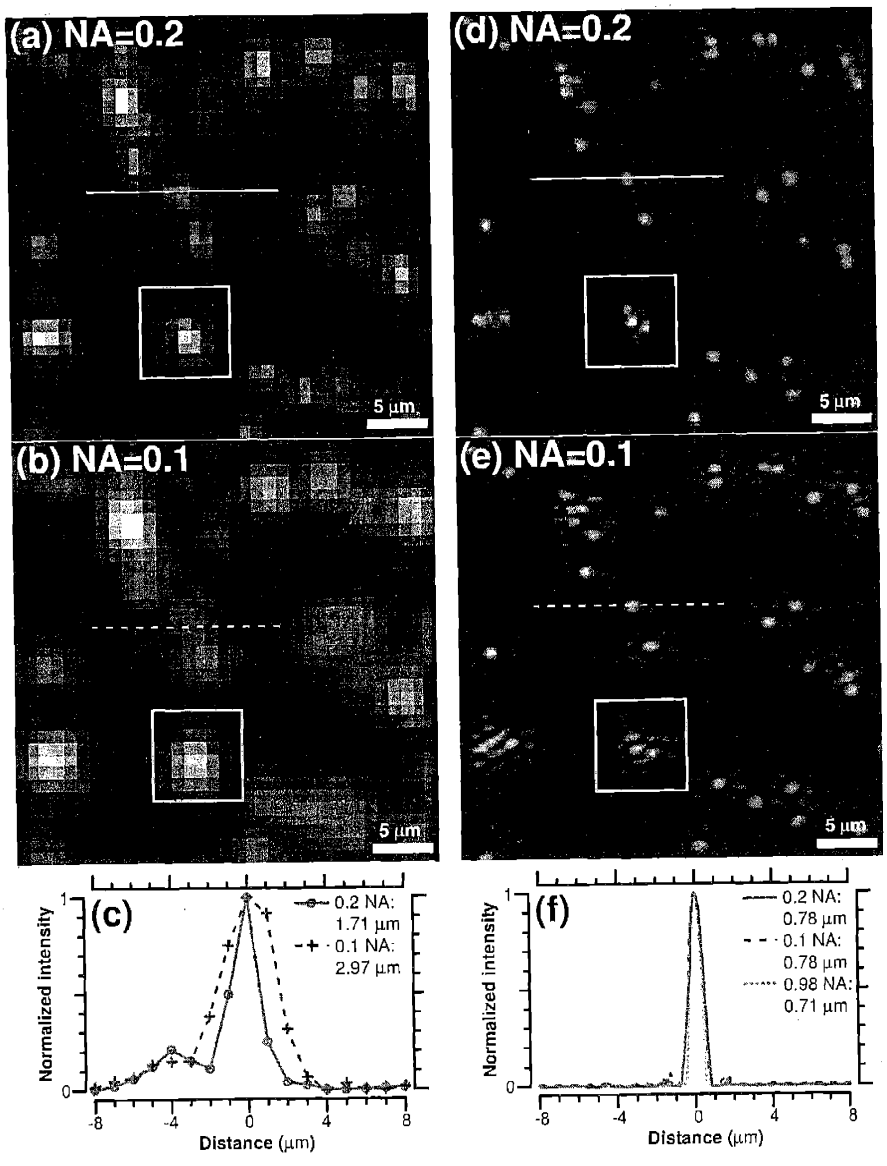

Figure 6-1: Effect of NA on resolution in conventional microscopy (left column) as compared to the structured illumination approach (right column). The figure shows images of the same region of a target made of 1 μm diameter fluorescent microspheres. The box in each image contains a cluster of three microspheres. (a) Averaged image, with NA of 0.2. (b) Averaged image, with NA of 0.1. (c) Intensities along the solid line in (a) (0.2 NA, uniform illumination) and the dashed line in (b) (0.1 NA, uniform illumination). FWHM's of the intensity scans are shown inside the plot. (d) Image reconstructed using the knowledge of illumination, with NA of 0.2. (e) The same as in (d) but with NA of 0.1. (f) Intensities along the solid line in (d) (0.2 NA, structured illumination) and the dashed line in (e) (0.1 NA, structured illumination). The dotted line is an intensity scan from a computer simulated image of a 1 μm diameter microsphere acquired with 0.98 NA objective.

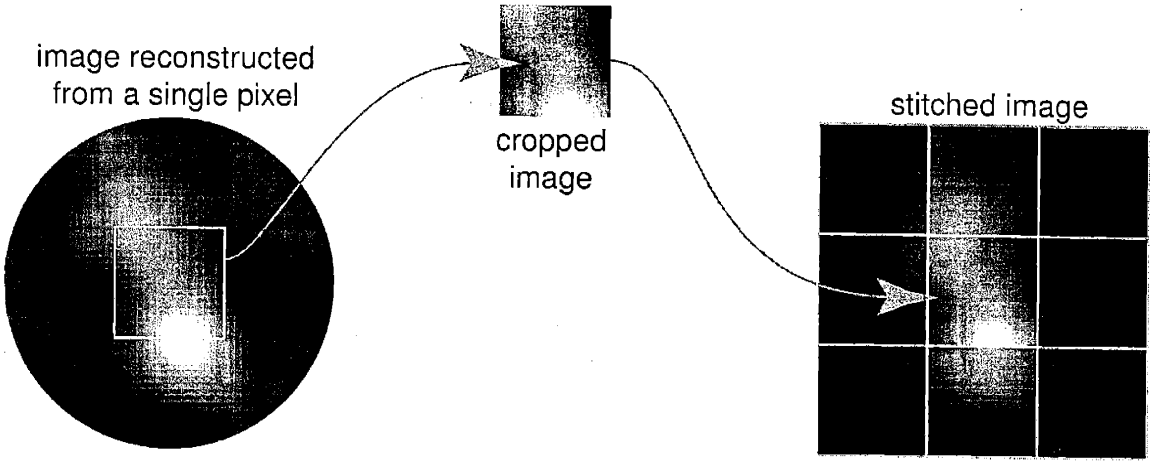

Figure 6-2: Stitching images reconstructed from an array of pixels. Left: an image reconstructed from a single pixel of the CCD. The size of the pixel in the target space is indicated by the rectangle inside the image. Notice that the image is larger than the pixel and shows sub-pixel details of the target. Center: An image generated by cropping the rectangular center portion of the image on the left side. Right: An image made by stitching nine cropped images reconstructed from nine pixels.

Figure 6-2 is the same image as Figure 5-11, reconstructed using data from a single pixel. The image in the middle was produced by cropping the image on the left for the area occupied by the pixel. Finally, the image on the right was generated by stitching 9 cropped images from 9 pixels. The images in Figure 6-1 (d) and (e) were made by stitching 1,225 cropped images reconstructed from 1,225 pixels.

When comparing Figure 6-1 (a) and (d) [or Figure 6-1 (b) and (e)], it should be emphasized that the excitation light energy, the objective, and the camera and its exposure time are the same. Individual microspheres in a cluster are readily resolved in both Figure 6-1 (d) and (e), in contrast to Figure 6-1 (a) and (b). Also, when the NA decreased from 0.2 to 0.1, the FWHM of the same microsphere showed a negligible change (from 0.76 μm to 0.76 μm, Figure 6-1 (f)) compared to the factor of 1.74 increase seen in Figure 6-1 (c). The plot in Figure 6-1 (f) also shows a simulation of the intensity scan that would be expected for an ideal 0.98 NA objective and uniform illumination. Note that this simulation matches almost perfectly the resolution achieved using structured illumination approach with a 0.98 NA synthetic aperture.

The results clearly show that the NA of the objective has a negligible effect on

the resolution of the structured illumination approach. Its resolution is determined primarily by the synthetic NA of the cone of illuminating beams. The resolution achieved is comparable to that expected from an objective with the same cone angle as the cone of beams (NA = 0.98). The NA of the objective lens can be chosen to permit substantial gains in WD, DOF, and FOV. With a 0.1 NA objective, these are increased by more than an order of magnitude relative to a 0.98 NA objective.

Chapter 7

Target Metrology

7.1 Introduction

Recently, there has been a lot of progress in fabricating structures at nanometer size scales. Within a few years, semiconductor processes are expected to produce devices with minimum features of 60 nm or less. There are increasing needs to develop tools to visualize and measure the fabricated structures, to control the quality of the fabrication process and to provide feedback to the design process. This step becomes especially important when a laboratory success is to be transferred to a manufacturing site for mass-production (Schattenburg and Smith, 2001).

In the semiconductor industry, the current standard for measuring the critical dimension (CD) of fabricated structures is Scanning Electron Microscopy (SEM). SEM provides sub-nanometer spatial resolution. However, it requires destructive chemical and mechanical pre-processing of the sample. Its speed is also a limitation in meeting the current industry target of 1 cm^2/sec. The technique is difficult to implement in an on-line arrangement for high throughput device evaluation.

An alternative CD metrology technique that is currently under development is the scatterometer (Raymond et al., 1997), which is an optical technique. Scatterometry is based on analysis of light diffraction from periodic structures. Compared to the SEM, the scatterometry is fast, convenient, and low-cost. Also, it is non-destructive and does not require any pre-processing of the sample. However, it applies only

to periodically structured targets. Post-processing of the measured data to obtain quantitative information is also computationally complex.

It would be desirable to combine the benefits of the above two techniques: the direct imaging capability of the SEM that makes it possible to obtain metrological information about an arbitrary target, with the speed and convenience of an optical method. The structured illumination approach presented in this thesis is a promising step toward this goal. Unlike scatterometry, where uniform illumination is used to probe a periodically structured target, the structured illumination can be used to probe non-periodic structures (such as single gates) in resist as well as post-etch materials. The known, controllable structures in the illumination are used as probes to obtain quantitative metrological information about the target.

This chapter describes preliminary results that obtain quantitative information from a fluorescent target using the structured illumination approach. Figure 7-1 (a) is an image of a 100 μm by 100 μm region of a target of 1 μm diameter fluorescent microspheres, obtained using conventional (uniform) illumination. Figure 7-1 (b) is a 4 μm by 4 μm sub-region of the image in (a). Figure 7-1 (c) shows an image of the same sub-region acquired using the same lens and camera, but with structured illumination. The two images in (b) and (c) illustrate the improvement in image resolution provided by the structured illumination approach. In this chapter, we focus on using this improved resolution to determine the position and diameter (D) of a microsphere, as illustrated in Figure 7-2.

7.2 Estimating position

A model-based approach was used to take advantage of the metrological information contained in the many pixels that represent a structure in the image. Each microsphere was modelled as a uniform volume source of light (Eq. (4.13) and Figure 4-5). In the absence of blur, brightness would be a hemispherical function of position, as shown in Figure 7-3 (a). The dashed line in the plot on the right side represents the brightness measured through the center of the microsphere. The parameters of the

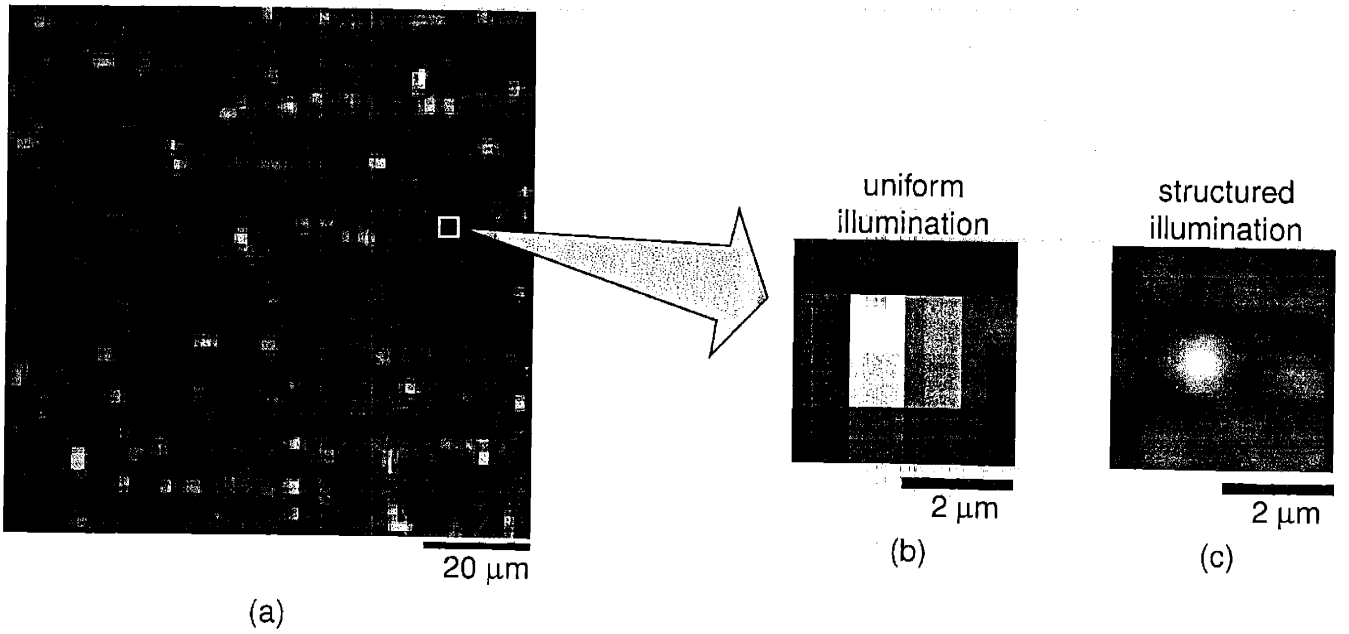

Figure 7-1: (a) A conventional optical microscopy (that is, using uniform illumination) image of a target made of a random monolayer of 1 μm diameter fluorescent microspheres. (b) A sub-region of image in (a) consisting of gray values from 16 pixels. The shape of the target within the region is not resolved. (c) Computationally reconstructed image of the same region in (b) using structured illumination approach. The same lens and camera as in (b) were used to acquire the data from which the image is reconstructed. Comparing the images in (b) and (c) demonstrates the improvement in resolution due to structured illumination method.

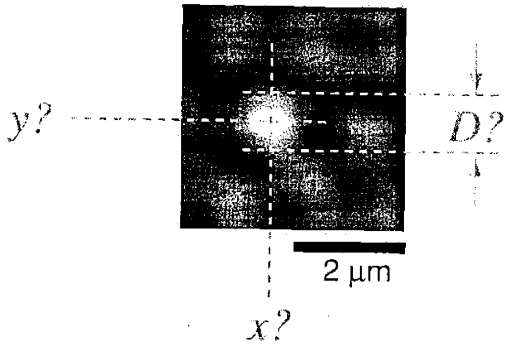

Figure 7-2: Improved resolution leads to more precise determination of target information, such as the position (x,y) and the diameter (D) of a microsphere.

model are the position of the center (x and y, only x is indicated in the plot), and the width D of the hemisphere.

The model shown in Figure 7-3 (a) was fit to a reconstructed image of the target, using a least squares approach. The image in Figure 7-3 (b) shows a representative

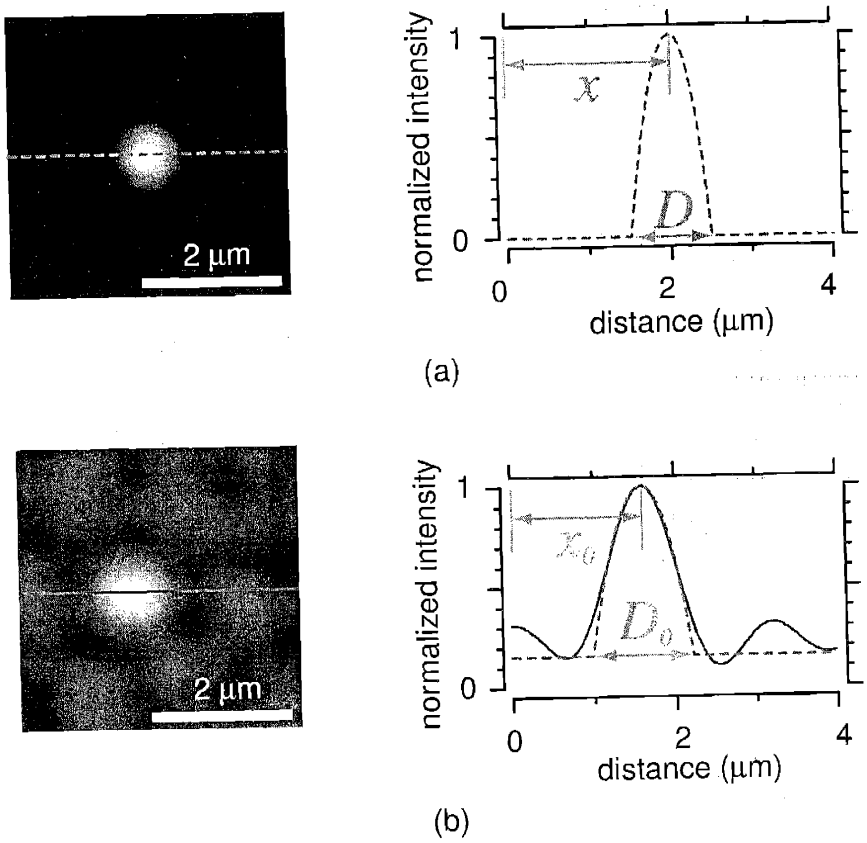

Figure 7-3: A model based approach to determine the position of a microsphere. (a) A computer simulated image (left) of a microsphere model (Eq. (4.13) and Figure 4-5) and the brightness measured through the center of the microsphere (right). The three parameters of the model are the position (x and y) and the diameter (D). (b) A reconstructed image of a microsphere using the structured illumination approach (left). The parameters of the model in (a) that best fit the image data in (b) were found by the least-square method. The continuous line is the brightness along the line in the image on the left side and the dashed line is the brightness of the best fit model at the same y position. The estimated x position, x_0, and the diameter, D_0 are indicated in the plot.

image of a microsphere. The parameters of the hemispherical function that best fits the image were found. The position of the peak brightness in the fitted function determines the position of the microsphere. The y-position of the center is indicated by the continuous line in the image. The plot shows the intensities along the continuous line in the image on the left side (continuous line in the plot) and the corresponding intensities of the best fit model (dashed line). The estimated x position of the microsphere is indicated as x_0 in the plot.

The positions of 20 microspheres were determined using 12 different calibration

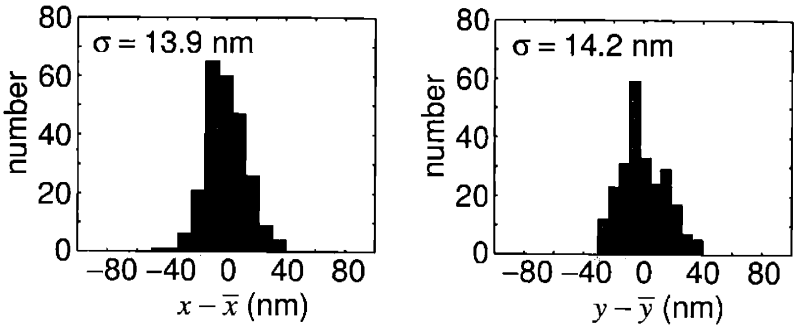

Figure 7-4: Histograms of the measured distances in x (left) and y (right) from their respective means. Data from 20 microspheres. For each microsphere, its position (x and y) was determined 12 times using 12 different calibration targets. The standard deviation represents the reproducibility of the position determination.

targets. This process resulted in 240 independent measurements of the centers (x and y) of the microspheres. For each target, the means and standard deviations of x and y were computed. The plots in Figure 7-4 show histograms of the measured distances in x and y from their respective means. The standard deviations of the data, that represents the reproducibility of the measurement technique, are 13.9 nm and 14.2 nm for x and y respectively.

7.3 Estimating diameter

The model fitting procedure described in the previous section also produced an estimate of the diameter of a microsphere (D_0 in Figure 7-3 (b)). However, unlike the position estimate, the diameter estimate is biased and systematically overestimates the actual diameter. It is necessary to determine the origin of this bias and to compensate for it.

The bias was modelled by computer simulation of the imaging process of the structured illumination method. The left side of Figure 7-5 (a) shows an image of the model of a microsphere with 1.000 μm diameter and the right side of the same figure shows a line plot of brightness along the center of the microsphere. The left side of Figure 7-5 (b) is a computer simulated image of the microsphere in Figure 7-5 (a). Notice the similarity between the simulated image and the experimentally

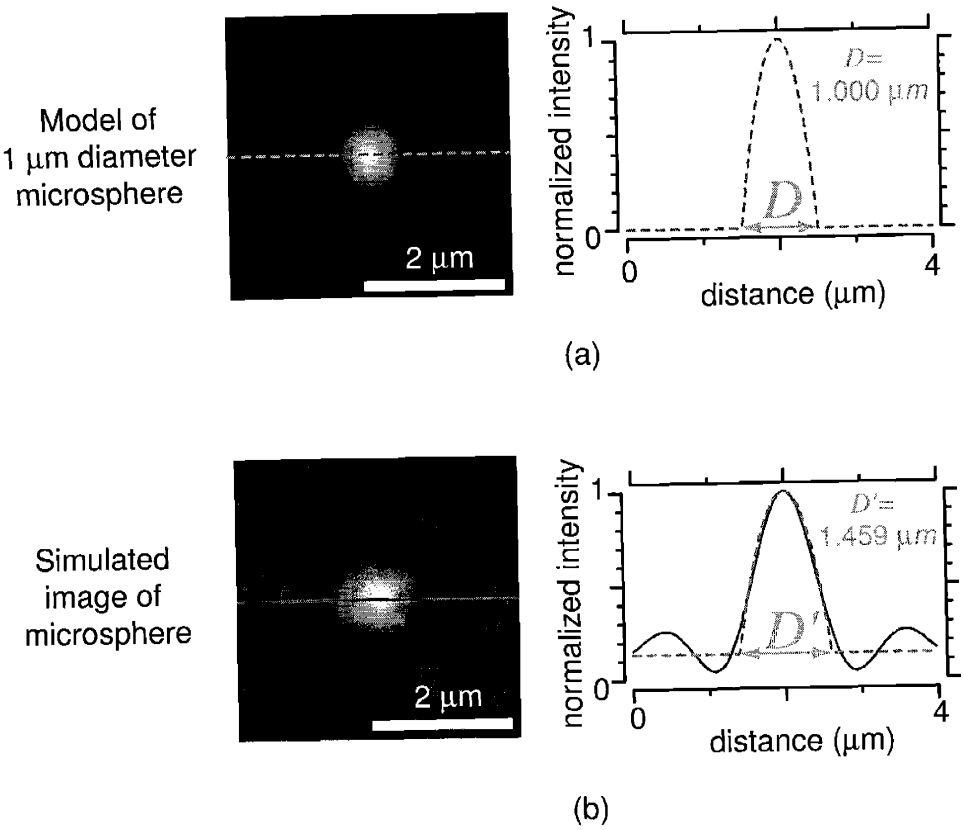

Figure 7-5: Determining the bias in diameter estimation. (a) An image of the model of a microsphere (left) and the brightness measured through the center of the microsphere (right). The diameter (D) of the model is indicated. (b) Computer-simulated image of the microsphere in (a) and the brightness measured through the center of the microsphere (straight line). Dashed line is the brightness scan of the best fit model of the image data. The diameter of the best-fit model, D', is indicated. The bias factor, s, is the ratio between the apparent diameter, D', and the true diameter, D.

reconstructed image in Figure 7-3 (b). The previously described hemisphere model was then fitted to the simulated image of a microsphere and the diameter of the best-fit model (D' in Figure 7-5 (b)) was found. Thus, the bias increases the apparent diameter by a factor of $s = D'/D = 1.459$.

The diameters of 20 microspheres were determined and corrected for bias. Figure 7-6 shows the resulting mean diameter and standard deviation and compares them with Transmission Electron Microscopy (TEM) data. The TEM data were provided by the manufacturer of the microspheres.

	TEM	SI
mean diameter	1.000 μm	1.029 μm
standard deviation	25 nm	26 nm

Figure 7-6: The mean diameter and the standard deviation of microspheres. TEM: Transmission Electron Microscopy data obtained from the manufacturer of the microsphere. SI: Diameters of 20 microspheres obtained using the structured illumination approach.

Chapter 8

Summary and Perspective

This thesis presents the first experimentally generated images based on the concept of the synthetic aperture optics. First, it was demonstrated that a sequence of brightnesses of a target, measured using a single photo-detector when the target was illuminated by a sequence of light patterns, can be processed to reconstruct an image of the target. The reconstructed image, which is larger than the size of the photo-detector, shows sub-pixel details of target's contrast pattern. This opens up a possibility to obtain meaningful images of a target using a high speed, high sensitivity photo-detector such as photo-multiplier tube (PMT) or avalanche photo-diode (APD), without any mechanical scanning involved.

Secondly, the results clearly demonstrate that, in the structured illumination approach, the resolution is primarily derived by the structured illumination, rather than the microscope objective as in the conventional system. This leads to breaking of the intrinsic coupling between resolution and other optical performances such as working distance, field of view, and depth of field. In the current system, high resolution is derived from the high numerical aperture illuminator, and long working distance, large field of view, and large depth of field are derived from the low numerical aperture objective on the imaging side. The combination of the system's optical performances clearly breaks the previous trends (Figure 8-1).

Finally, this work represents a meaningful first step towards scaling optical microscopy to UV and X-ray to improve its resolution. The cone of beams, which are

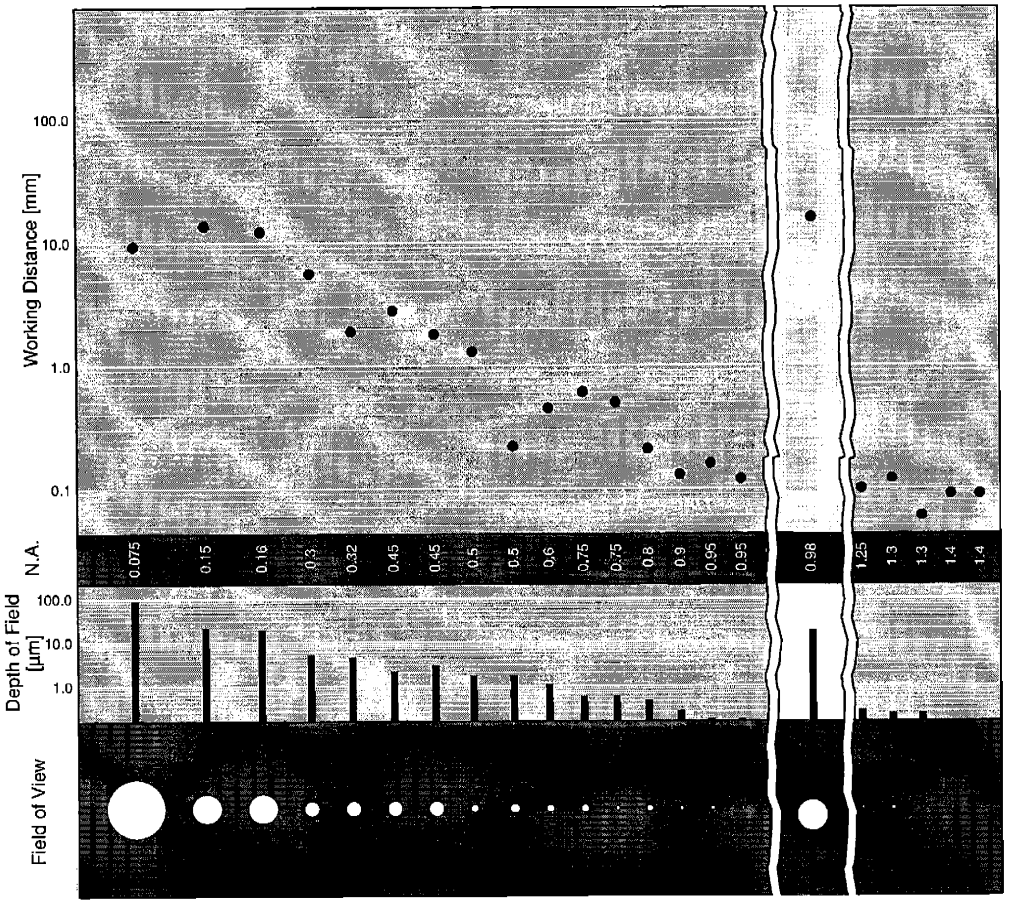

Figure 8-1: In the structured illumination approach, high resolution is derived from the high NA illuminator and long working distance, large field of view, and large depth of field are derived from the low NA objective. The chart overlays the optical performances of the current structured illumination system on top of the performances of 20 different microscope objectives shown in Figure 1-1. The combination of performances of the structured illumination system clearly breaks the previous trends.

the determinant of the system's resolution, is delivered by a system of flat mirrors, which are reflective optical elements. Unlike the lens which is a refractive element, mirrors can handle short wavelengths of light such as UV and X-ray.

The above outcomes are expected to open up possibilities of various biomedical investigations that were previously impossible or difficult to perform. Any high resolution fluorescence imaging task that requires long working distance, large field of view, and large depth of field will benefit from the current system. One such example

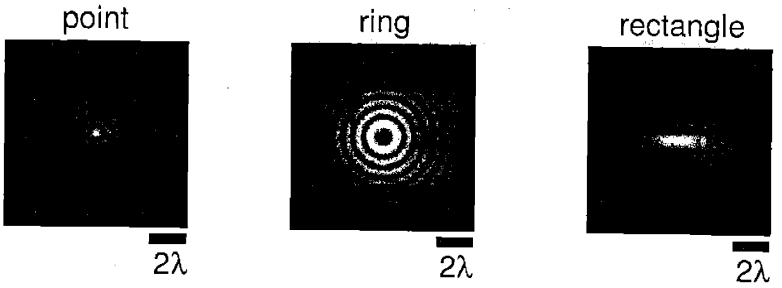

Figure 8-2: Computer simulated optical patterns (a point, a ring, and a rectangle, from left to right) formed by the interference of 41 coherent beams that converge in a cone with a NA of 0.98. Each optical pattern is produced by selecting the amplitudes and phases of the beams in an appropriate way. When the beams converge in a cone with the same angle relative to the horizontal plane, the same optical pattern is maintained along the axial direction due to the symmetry of the beams. Also, these optical patterns can be translated or rotated by electronically modulating the beam phases.

is an *in vitro* culture of cells on a glass or polymer substrate. Taking advantage of the system's improved working distance, without compromised resolution, cellular imaging could be performed simultaneously with non-optical probing or manipulation of the same cell, such as electrophysiological recording or mechanical stimulation.

The technique is based on projection of known optical patterns formed by the interference of multiple laser beams. This capability can be further developed for non-imaging applications. Algorithms can be developed to determine the amplitudes and phases of the beams that generate a desired interference pattern. Figure 8-2 shows several examples of such optical patterns, generated by computer simulation of 41 beam system with 0.98 NA. These optical patterns could potentially be used to produce high spatial and temporal resolution control of chemical or biological reactions, or, depending on the light energy, can even be used to manipulate microscopic objects as in the well-known light tweezer applications (Ashkin et al., 1986; Garces-Chavez et al., 2002).

	μ_R	σ_R (% of μ_R)	λ_A/λ_E (nm)
NS 1	250 nm	10 nm (4.0 %)	505/515
NS 2	105 nm	10 nm (9.5 %)	505/515
NS 3	50 nm	3 nm (6.0 %)	488/560

Figure A-2: Properties of the three types of nanosphere samples (NS1, NS2, and NS3) used to make the self-assembled monolayers, provided by the manufacturer. μ_R: mean radius, σ_R: standard deviation, λ_A: peak absorption wavelength, λ_E: peak emission wavelength.

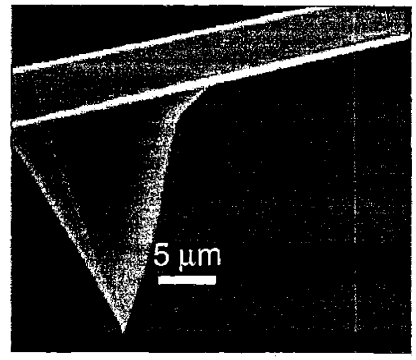

Figure A-3: An electron microscopy image of the AFM tip used to acquire images of the self-assembled monolayers of microspheres.

quencies ranging from 200 kHz to 400 kHz and were conical in shape with the cone angle of 35 degrees and the effective radius of curvature at the tip of 10 nm.

A.0.3 Results

AFM images of self-assembled monolayers of three different types of nanospheres listed in Figure A-2 are shown in Figure A-4. The top left corresponds to the AFM image of 250 nm radius nanospheres. The periodic, hexagonal assembly of nanospheres is clearly shown in the image. Notice the existence of several defects in the imaged region. These defects are caused by non-uniformity in the size of the nanospheres: the defects in sub-region A and B are caused by a relatively large and small nanosphere, respectively. The number of defects could be reduced by using nanospheres with more

precisely controlled sizes.

The middle part of the top panel shows the Fourier transform magnitude of the image to its left in gray scale. The hexagonal periodicity of the arrangement of nanospheres gives rise to 6 distinct peaks in the Fourier domain. The plot to the right shows the normalized Fourier transform magnitude along the dotted straight line in the middle part. These peaks fall on a circle centered at DC (shown as the dotted circle in the middle part). The radius of this circle is the frequency domain representation of the distance between adjacent spheres. The angular orientation of the peaks along the circle represents the directional characteristics of the crystalline structure of nanospheres. Therefore, the Fourier domain analysis is a convenient way to obtain averaged metrological information about the target.

The middle and the bottom panels in Figure A-4 show the corresponding images and plots for radii of 105 nm and 50 nm, respectively. The AFM images clearly demonstrate the validity of the fabrication technique scaled to different size nanospheres. Fourier transform magnitude for each case shows 6 peaks similar to the top panel, again located on a circle whose radius is inversely proportional to the radius of the nanospheres used.

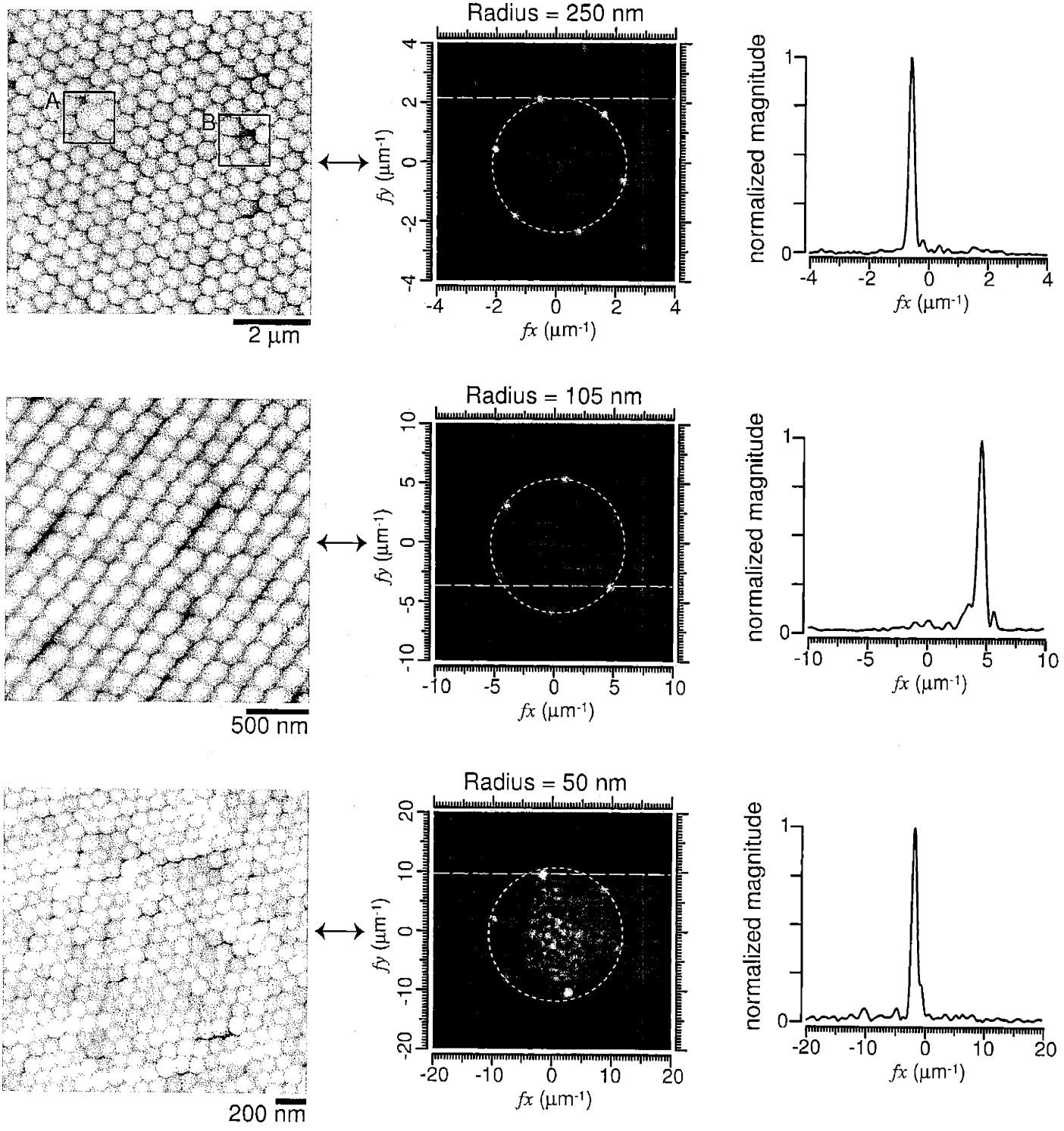

Figure A-4: AFM images of self-assembled monolayers of three different types of microspheres and their Fourier transform. See text for details.

Bibliography

Abbe, E. (1873). Beiträge zur theorie des mikroskops und der mikroskop ischen wahrnehmung, *Arch. Mikrosk. Anat.* **9**: 413–468.

Adler, R. (1967). Interaction between light and sound, *IEEE Spectrum* pp. 42–54.

Ashkin, A., Dziedzic, J. M., Bjorkholm, J. E. and Chu, S. (1986). Observation of a single-beam gradient force optical trap for dielectric particles, *Optics Letters* **11**: 288.

Aurenhammer, F. (1991). Voronoi diagrams: A survey of a fundamental geometric data structure, *ACM Computing Surveys* **23**: 345–405.

Bailey, B., Farkas, D. L., Taylor, D. L. and Lanni, F. (1993). Enhancement of axial resolution in fluorescence microscopy by standing-wave excitation, *Nature* **366**: 44.

Born, M. and Wolf, E. (1999). *Principles of Optics*, Cambridge University Press, New York.

Brow, W. N. (1975). *Methods in Computational Physics*, B. Alder, S. Fernbach, and M. Rotenberg, Eds. New York: Academic, pp. 131–175.

Cragg, G. E. and So, P. T. C. (2000). Lateral resolution enhancement with standing evanescent waves, *Optics Letters* **25**(1): 46.

Deckman, H. W. and Dunsmuir, J. H. (1982). Natural lithography, *Applied Physics Letter* **41**(4): 377–379.

Deckman, H. W. and Dunsmuir, J. H. (1983). Application of surface textures produced with natural lithography, *J. Vac. Sci. and Technol. B.* **1**(4): 1108–1112.

Elston, G. (1985). Intermodulation products in acousto-optic signal processing systems, *1985 IEEE Ultrasonics Symposium* pp. 391–397.

Frohn, J. T., Knapp, H. F. and Stemmer, A. (2000). True optical resolution beyond the rayleigh limit achieved by standing wave illumination, *Proc. Natl. Acad. Sci. USA* **97**: 7232–7236.

Frohn, J. T., Knapp, H. F. and Stemmer, A. (2001). Three-dimensional resolution enhancement in fluorescence microscopy by harmonic excitation, *Optics Letters* **26**(11): 828.

Garces-Chavez, V., McGloin, D., Melville, H., Sibbett, W. and Dholakia, K. (2002). Simultaneous micromanipulation in multiple planes using a self-reconstructing light beam, *Nature* **419**: 145.

Goodman, J. W. (1996). *Introduction to Fourier Optics*, McGraw-Hill, Boston.

Gustafsson, M. G. L. (2000). Surpassing the lateral resolution limit by a factor of two using structured illumination microscopy, *J. Microsc.* **198**: 82–87.

Gustafsson, M. G. L., Agard, D. A. and Sedat, J. W. (1999). 3D widefield light microscopy with better than 100 nm axial resolution, *J. Microsc.* **195**: 10.

Hecht, D. L. (1977). Multifrequency acousto-optic diffraction, *IEEE Transactions on Sonics and Ultrasonics* pp. 7- 18.

Heintzmann, R. and Cremer, C. (1998). Laterally modulated excitation microscopy: improvement of resolution by using a diffraction grating, *Proc. SPIE* **3568**: 185.

Herman, G. T. (1979). *Image Reconstruction from Projection: Implementation and Applications*, Springer-Verlag, Berlin.

Hong, S. S. (2001). *Surface acoustic wave optical modulation*, Master's thesis, Massachusetts Institute of Technology, Cambridge, MA.

Hooke, R. (1961). *Micrographia*, Facsimile edition, Dover, New York.

Hulteen, J. C. and Duyne, R. P. V. (1995). Nanosphere lithography: A materials general fabrication process for periodic particle array surfaces, *J. Vac. Sci. and Technol. A.* **13**(3): 1553–1558.

Ippen, E. P. (1967). Diffraction of light by surface acoustic waves, *Proceedings of the IEEE* **55**: 248.

J. B. Pawley, E. (1995). *Handbook of Biological Confocal Microscopy*, Plenum Press, New York.

Keto, E. (1997). The shapes of cross-correlation interferometers, *The Astrophysical Journal* **475**: 843–852.

King, K. F. and Moran, P. R. (1984). A unified description of nmr imaging, data collection strategies and reconstruction, *Magn. Reson. Med.* **11**: 1–14.

Korpel, A. (1981). Acousto-optics: a review of fundamentals, *Proceedings of the IEEE* **69**: 48–53.

Korpel, A. (1997). *Acousto-optics*, Marcel Dekker, New York.

Krishnamurthi, V., Bailey, B. and Lanny, F. (1996). Image processing in 3d standing-wave fluorescence microscopy, *Proc. SPIE* **2655**: 18.

Mermelstein, M. S. (2000a). Multiple beam pair optical imaging, U.S. Patent No. 6,016,196.

Mermelstein, M. S. (2000b). Optical synthetic aperture array, U.S. Patent No. 6,140,660.

Mermelstein, M. S. (2000c). *Synthetic aperture microscopy*, PhD thesis, Massachusetts Institute of Technology, Cambridge, MA.

Mueller, R. K., Kaveh, M. and Wade, G. (1979). Reconstructive tomography and applications to ultrasonics, *Proc. IEEE* **67**: 567–587.

Neil, M. A. A., Juškitis, R. and Wilson, T. (1997). Method of obtaining optical sectioning by using structured light in a conventional microscope, *Opt. Lett.* **22**: 1905.

Nelder, J. A. and Mead, R. (1965). A simplex method for function minimization, *Computer Journal* **7**: 308–313.

Press, W. H., Flannery, B. P., Teukolsky, S. A. and Vettering, W. T. (1988). *Numerical recipies in C*, Cambridge University Press, Cambridge, UK.

Raymond, C. J., Murnane, M. R., Prins, S. L., Sohail, S., Naqvi, H. and McNeil, J. R. (1997). Multiparameter grating metrology using optical scatterometry, *J. Vac. Sci. Technol. B* **15**(2): 361–368.

Schattenburg, M. L. and Smith, H. I. (2001). The critical role of metrology in nanotechnology, *Proceedings of the SPIE Workshop on Nanostructure Science, Metrology and Technology* **4608**.

So, P. T. C., Kwon, H. and Dong, C. Y. (2001). Resolution enhancement in standing-wave total internal reflection microscopy: a point-spread-function engineering approach, *J. Opt. Soc. Am. A* **18**: 2833.

Wang, B. (2003). Linear birefringence measurement at 157 nm, *Review of Scientific Instruments* **74**(3): 1386–1389.

Wang, B., Ward, M., Rockwell, R. and List, J. (2002). Measuring birefringence in calcium fluoride at 157 nm, *Photonics-Spectra* **36**(11): 62-69.

White, R. M. and Voltmer, F. W. (1965). Direct piezoelectric coupling to surface elastic waves, *Applied Physics Letters* **7**: 314–316.